

PROCESSING AND CHARACTERIZATION OF COPPER INDIUM SELLINIDE
FOR PHOTOVOLTAIC APPLICATIONS

By

CHEN-RENG CHANG

A DISSERTATION PRESENTED TO THE GRADUATE SCHOOL
OF THE UNIVERSITY OF FLORIDA IN PARTIAL FULFILLMENT
OF THE REQUIREMENTS FOR THE DEGREE OF
DOCTOR OF PHILOSOPHY

UNIVERSITY OF FLORIDA

1995

To my parents, A-C Chang, and C-K Tsai

♫

My wife, Hui-Chen, and our three kids

ACKNOWLEDGMENTS

I have benefited from many people during my graduate career. I would like to thank Dr. Tim Anderson, chair of my supervisory committee, for his guidance and support for my research. I am indebted to Dr. Sheng Lu for teaching me device physics and for giving me much more advice. Dr. Hefeng Wang taught me about vacuum evaporation and allowed previous visits to his lab. I am also grateful to Dr. Chuanli for many useful discussions during our biweekly group meeting, and to Dr. Guang for serving as my co-mentor and providing helpful suggestions.

My colleagues in this project have helped and taught me very much. Billy Standley taught me about being a dedicated scientist by setting an example. Dr. Albert Dwyer received my greatest appreciation for patiently tutoring me about phase diagrams and solid state chemistry. I am indebted to Dr. Wentong Zhang and Dr. Jiaquan Xiao for sharing their expertise in density-functional modeling and phase diagram calculations. I would like to thank Dr. Augusto Morozzi, Eric Pedroni, Jeremy Thompson, Qing Zhu for TDD analysis and sample preparations. I am also grateful to Chao-hua Huang, Lei Li, Loren Park, Mahan Mitei, Saba Kati, and Serkan Kozal for being such good team partners in this project. Thanks to Eric Lindberg and Wayne Ageron in IMAC for their help in AFS and WDS analysis, respectively.

I am fortunately to have had the opportunity to collaborate with many scientists from other departments and laboratories. I am grateful to Nadia Lajmoussi in Advanced

Photon Source, Argonne National Laboratory and to Dr. Randy Glaser in the Chemistry Department for making the XAFS experiments possible. I am indebted to Dr. Grant Barker at the Illinois Institute of Technology for sharing his knowledge of XAFS data analysis. I would like to thank Dr. Phil Albrecht at NREL for teaching me HETED at SLAC, Dr. Se-Hyun Woo at NREL for the collaboration of first principle calculations. Many thanks to Dr. Raghu Srinivasan and Dr. Ramesh Ramamoorti, both at NREL, for help in ECP measurements and crystal fabrication and characterization. I am indebted to Dr. Andrew Payson at HTMIL, ORNL, for powder XRD measurements and for teaching me how to use OLDS for Rietveld refinement.

TABLE OF CONTENTS

page

ACKNOWLEDGEMENTS	iii
ABSTRACT	viii
CHAPTERS	
1 INTRODUCTION	1
1.1 Photocatalytic Devices	2
1.2 Catalyst-based Photocatalysts	3
1.3 Current Understanding and Future R&D Challenges	6
1.4 Statement of Thesis Work	11
2 THEORY AND PROCEDURES FOR ASSESSING THERMOCHEMICAL AND PHASE DIAGRAM DATA	12
2.1 Introduction	12
2.2 Principle of Phase Diagram Calculation	14
2.3 CALPHAD Methodology	15
3 THERMODYNAMIC ASSESSMENT OF THE SILICON-BINARY SYSTEM	19
3.1 Introduction	19
3.2 Literature Review	19
3.3 Assessments	22
3.4 Vapor Pressure and Composition at Equilibrium with Condensed Phases	41
3.5 Flux Calculations for a Fluidy Evaporating Source	44
3.6 Conclusions	44
4 A CRITICAL ASSESSMENT OF THERMODYNAMIC AND PHASE DIAGRAM DATA FOR THE Cu-Ge SYSTEM	55
4.1 Introduction	55

4.2 Phase Diagram Data	35
4.3 Enthalpy, Entropy and Heat Capacity Data	36
4.4 Gibbs Energy Data	41
4.5 Thermodynamic Models	42
4.6 Optimization Procedure	47
4.7 Results and Discussion	49
4.8 Conclusions	71
5 A CRITICAL ASSESSMENT OF THERMODYNAMIC AND PHASE DIAGRAM DATA FOR THE In-Sn SYSTEM	83
5.1 Introduction	86
5.2 Phase Diagram Data	89
5.3 Enthalpy, Entropy and Heat Capacity Data	92
5.4 Gibbs Energy Data	103
5.5 Thermodynamic Models	106
5.6 Optimization Procedure	107
5.7 Results and Discussion	109
5.8 Conclusions	111
6 Cu₆₀Sn, THEN FILM FORMATION BY RAPID-THERMAL PROCESSING	121
6.1 Introduction	123
6.2 Previous Studies on RSP Cu ₆₀	124
6.3 Reaction Firing Engineering	127
6.4 Process Details	136
6.5 Rapid Thermal Processing	139
6.6 Characterization	140
6.7 Results and Discussion (Process Version-1)	141
6.8 Results and Discussion (Process Version-II)	160
6.9 Conclusions	170
7 X-RAY ABSORPTION FINE STRUCTURE(XAFS) INVESTIGATIONS OF COPPER-INDIUM SOLID-STATE NANOCONDUCTION ALLOYS	171
7.1 Introduction	173
7.2 Theory of Extended X-ray Absorption Fine Structure(EXAFS)	175
7.3 Experimental system for XAFS	179
7.4 Compositional effects on the local structure of Cu ₆₀ Sn	184
7.5 Local structure of Cu ₆₀ Sn	195
7.6 Discussion	213
7.6 Conclusions	224

8. CONCLUSIONS AND FUTURE WORK	226
8.1. Conclusion	226
8.2. Future Work	231
REFERENCES	235
GEOGRAPHICAL SKETCH	248

Abstract of Dissertation Presented to the Graduate School
of the University of Florida in Partial Fulfillment of the
Requirements for the Degree of Doctor of Philosophy

**PROCESSING AND CHARACTERIZATION OF COPPER INDIUM TELLURIDE
FOR PHOTOVOLTAIC APPLICATIONS**

By

Chih-hung Chang

December 1995

Chairman: Timothy J. Anderson
Major Department: Chemical Engineering

Polycrystalline CadCdTe and related materials, are promising candidates of low-cost high efficiency solar cells. This thesis describes the applications of phase diagrams to suggest alternative absorber precursor structures, explores the use of Rapid Thermal Processing (RTP), and characterizes the structure of CadCdTe and related materials.

A critical assessment of the thermochanical and phase diagrams data for the Cu-In-CdTe₂ and In-In-CdTe₂ binary systems was performed. The information was used to give an evaluated Cu₂In₂Te₄ pseudobinary phase diagram and suggest liquidus lines in the Cu-In-CdTe₂ system. The resulting information was used to propose a novel In-doped precursor structure consisting of a co-deposited In₂Se₃ (50 to 55 Se, wt %) top layer and a CdTe₂ (30 to 35 Se, wt %) bottom layer. This precursor structure was designed to form CdTe by reacting a liquid CdSe with a solid InSe phase in the process temperature window.

1070°C to 1170°C. Two different precursor structures were elaborated and tested. The first one consists of the three layers $\text{In}_2\text{Se}_3/\text{CuInSe}_2/\text{CuSe}$, and the second one was a simple two-layer structure InSe/CuSe . After RTP the first precursor structure underwent a liquid-solid reaction and formed large grained CuInSe_2 . Here it is believed the mixing of say InSe layer occurs through a miscible reaction. The second precursor structure also lead to the formation of large grained $\text{CuIn}_2\text{-Squid}$ films, as suggested in the reaction pathway analysis.

X-ray Absorption Fine Structure (XAFS) measurements were performed on crystals of CuInSe_2 with different compositions close to the 1:1:2 stoichiometry and CuIn_2Se_4 . It was found that the Cu-Se bond length is independent of the Cu occupancy number in the composition range within a length of 0.11 Å. Least-square fitting of the Se-K edge EXAFS spectra indicated CuInSe_2 consists of Se-centered tetrahedron with an average of 2 Cu and 2 In nearest neighbors. On the other hand, CuIn_2Se_4 consists of Se-centered tetrahedron with an average of 3.3 Cu and 3.4 In nearest neighbors. The Cu-Se and In-Se bond lengths were determined to be 2.418 and 2.498 Å, respectively. This result already proves that CuIn_2Se_4 is indeed a defect tetrahedral structure and suggests a mixture of three types of local tetrahedral cationic clusters around each Se: 10% $\square\text{-Cu}_2\text{In}_2$ (I-II), and 40% $\square\text{-Cu+In}$ (I+II) and 50% $\square\text{-In+In}$ (II-III), where \square denotes vacancy and k denotes the sum of the cation valence electrons.

CHAPTER I INTRODUCTION

The search for a cheap, clean and renewable energy source has been a fundamental issue for mankind. The major energy source today is that generated by burning fossil fuels. These valuable resources of the earth are limited and will be depleted in the relatively near future. In addition to their limited supply, fossil fuels produce contamination gases that trap heat and are the largest contributors to the global warming effect. Various renewable energy sources do exist today, including photovoltaic solar cells, bio-fuels, hydroelectric power, and wind power. The conversion of sunlight directly into electricity using the photovoltaic properties of suitable materials is the most elegant energy conversion process.

The photovoltaic effect was discovered by Becquerel in 1839. The first practical photovoltaic device was the silicon solar cell developed at Bell Laboratories in 1954 for space applications. The energy crisis in the early 1970s raised the serious consideration for photovoltaic solar cells as an alternative energy source for terrestrial applications. Increased research efforts resulted in further improvements and the development of new photovoltaic materials and devices. These research efforts focused on improving performance, lowering cost, and increasing reliability. The last five decades of research and development have brought photovoltaic technology to a high level of performance. These efforts have been reflected in a steady growth of 15 to 20% per annum for more than a decade to reach \$1 billion sales in 1996. The industry expanded worldwide by a

10% growth to 100% despite fast expanding terrestrial market and the progress in cell technology, various challenges remain. For photovoltaics to be widely used the cost must be competitive with conventional energy sources, where the key issue is development of low-cost manufacturing processes.

The low energy density of the incoming sunlight requires large areas of semiconductors for the production of considerable amounts of electricity. This has photovoltaics were developed as a means of substantially reducing the cost of photovoltaic systems due to their reduced material costs, energy costs, handling costs, and capital costs. Many compound semiconductor materials have been examined for application in thin polycrystalline film solar cells. These materials include Cu_2S , CuInSe_2 and related alloys, CdTe , WSe_2 , Fe_2P_2 and TeInSe . Among these materials CuInSe_2 and CdTe and related alloys have made significant technical progress. Thin film CuInSe_2 and CdTe based solar cells have reported efficiencies of over 12% and 18.8%, respectively for small area laboratory devices, and over 12% for prototype modules. Many companies worldwide are now pursuing commercialization efforts based on these two technologies.

1.1 Photovoltaic Devices

In a photovoltaic device, electron-hole (e-h) pairs are generated by absorption of photons. The e-h pairs are then separated by the electric field present in the cell. The electric field can be produced by using a p-n junction, Schottky barrier, MIS (metal-insulator-semiconductor) structure, or semiconductor-electrolyte junction. Most of the photovoltaic devices are p-n junction solar cells, including CuInSe_2 -based photovoltaic devices.

The device I - V characteristics can be described by the Poisson and carrier continuity equations

$$\nabla \cdot \mathbf{E} = -q(p - n + N_D^+ + N_A^-) \quad (1.1)$$

$$\nabla \cdot \mathbf{J}_n = q(R - G) \quad (1.2)$$

$$\nabla \cdot \mathbf{J}_p = q(G - R) \quad (1.3)$$

where \mathbf{E} is the displacement vector, n and p are the free electron and hole densities, N_D^+ and N_A^- denote the acceptor density and donor densities, \mathbf{J}_n and \mathbf{J}_p are electron and hole current densities, G is the free carrier generation rate, and R_n and R_p are the hole and electron recombination rates. Given appropriate boundary conditions, these equations can be solved numerically [Oro 96] or analytically [Pim 88] for small device structures.

The fundamental material parameters associated with these carrier transport equations and that the device performance includes the band gap, electron affinity, optical absorption and reflection coefficients, refractive index, dielectric constant, carrier mobility, carrier lifetimes, and doping density (intrinsic and extrinsic). An understanding of the correlation between the structural, electrical, and optical properties in the semiconductor materials and the processing characteristics is essential in reproducibly manufacturing high-efficiency and low cost photovoltaic modules.

1.2 A Review of CdTe/CdS-based Photovoltaic Technologies

The first CdTe/CdS based photovoltaic device was reported by Roy, Wagner and Kaiser [Roy 75] in 1975. It was made by evaporating CdS on the (112) plane of a single crystal of p-CdTe. Subsequently thin film polycrystalline devices have been developed and the first efficient thin film CdS/CdTe solar cell was fabricated by Macklem and Chen [Mac 80]. Remarkable progress has been made in the

past few years by incorporating Cu into the absorber for optimized absorption of sunlight. The current state-of-the-art device was fabricated on FGLL with a total area efficiency of 11.9% [Kuo '05]. Figure 1.1 shows a cross section of a common thin CdTe/CdS-based photovoltaic device structure. The low cost soda lime glass serves as a substrate. A polycrystalline back contact, usually around 1 μm thick, is deposited by sputtering or a-beam evaporation. The CdTe/CdS absorber layer is normally grown by co-evaporation of the constituent elements. Following the absorber layer, a thin buffer layer (CdS or other Cd-free alternative) is prepared by chemical bath deposition. The n-type window layer normally consists of a thin layer of constant ZnO followed by a thinner and conductive layer of ZnO and doped with an Anti-Reflection Coating (ARC) (e.g. MgF_2). For small cells, a metal grid is formed on top of the ARC. In a typical grid, a thin Ni layer is first evaporated to form an Ohmic contact, followed by a thick Al layer to form the major body of the contact.



Figure 1.1: Schematic of a typical cross-section CdTe/CdS-based thin film photovoltaic device.

For large area devices (modules), the individual cells are series-connected by nonohmic interdigitated rather than use of metallic top-contact grids. The series interconnection between adjacent cells relies on the front contact TCO and the back contact Mo layers. Figure 1.2 displays a schematic cross-section of a typical module structure with the equivalent circuit. A review of module design analysis is given in Stachurski et al. [16]. The focus of this thesis is on the CIS absorber layer.



Figure 1.2 Schematic cross-section of the module structure with the equivalent circuit

1.3 Current Understanding and Future R&D Challenges

1.3.1 Substrate and underlayers

Several materials have been tested to use as a substrate for CIGS-based photovoltaic devices, including glass, silicon, selected polymers, and monolayer steel. The high-efficiency cells have been fabricated using low cost soda-lime glass (SLG), probably a result of the positive impact of its non-diffusion and its influence on grain growth during formation of the absorber. Experiments [18–21] have shown the CIGS-based PV performance strongly depends on the properties of the life contact. The Mo back contact is normally fabricated by dc magnetron sputtering. Adhesion and reactivity are the two properties affecting the life contact quality [See 15]. Another important role of the life layer is the interface between the Mo and underlying soda-lime glass substrate. The microstructure of the Mo film controls the extent of Mo diffusion into the absorber layer. Current research topics in this area include obtaining a better understanding of the relation between the microstructure of Mo film and Mo ion-diffusion from SLG substrate, sputtering the Mo deposition process to make a desirable microstructure [See 15] and the search for a good Mo diffusion-barrier [See 16].

1.3.2 Absorber

A wide variety of techniques have been used to fabricate CdTe/CdS-based thin films. There are two main types of deposition processes: co-evaporation and sequential

1.3.3 Co-evaporation Process

Co-evaporation is the most successful technique to fabricate high efficient CdTe/CdS-based solar cells since the demonstration of an 17% efficiency cell by the

deposited slowly [Min 92]. The lower co-evaporation process is a single layer process. This layer is deposited by first heating the elemental sources and the substrate to the desired temperature, then opening the shutter to initiate the deposition. A high substrate temperature (~500°C) is required to form device quality films. This process produces a homogeneous but small grained polycrystalline film across the substrate. The co-evaporation technique allows for changing the stoichiometric elemental flux ratio during the deposition. The in-layer process, first developed by Selenkiewicz and Chen [Min 93], utilizes this feature to produce CDS films with large grains. Deposition of CDS begins with a slight copper excess ratio to form a Cu₂S₂ and Cu₂Se mixed-phase film at low temperature, and followed by an indium excess flux to further re-crystallize the film layer at a higher temperature. The success of this recipe is attributed to a liquid assisted re-growth process, which is a result of the wetting of Cu₂S₂ in the presence of excess selenium. A further development lead to a three stage process [Chen 94]. This process begins with the formation of an In₂S₃ layer. This In₂S₃ layer is then subjected to a Cu and In flux to form Cu₂In₂S₄(s) and Cu₂Se(l) mixture in the second stage of this process. Finally In and Se fluxes are used to anneal the mixture Cu₂Se phase to form a large grain size device quality film. A similar process was also developed for CDS thin film formation.

1.3.2.3 Sequential Process

The characteristic of the sequential process can be described as low temperature precursor film deposition followed by high temperature annealing. There are many kinds of sequential processes. Selenkiewicz and Shaded Elemental Layer (SEL) processes are the two most studied. Selenkiewicz is a two stage process. First, sequential layers of

copper and silver are deposited on a molypdenum coated substrate. The metal precursor is then exposed to either H₂ or Sn₂ gas at high temperatures to form Cu₂Se₃ films. The EBL process differs from the solvothermal one by incorporating a *in situ* layer into the precursor structure [Dun 89]. CIS-based PV devices with efficiencies ~ 10% had been achieved by many groups using these two processes. The metal precursor layers for these two processes can be deposited at high rate by a variety of deposition techniques, such as sputtering, evaporation, electro-deposition, s-beam evaporation. This is an advantage for large-scale production; however, these processes are difficult to control. The search for a better precursor structure is an active research area [Chi 97].

1.1.3 The Role of Cu₂Se₃

CIS-based solar cells have been thought to be p-n structures (p-CIS, n-CIS). However, such a model does not predict the failure of high-Cu content devices. A novel model has been proposed by Schmidt *et al.* [Sch 91] that the growth kinetics of PVD-grown Cu₂Se₃ results in the in situ formation of a surface layer of Cu₂Se₃, and that this Cu₂Se₃/Cu₂Se₃ heterojunction is the true heterojunction partner to CIS device. This surface material is reported to show composition near Cu₂Se₃ and has been referred to as an "Ordered Vacancy Compound" (OVC). This significant finding resembles rather observation of a *in situ* junction observed by electron-beam induced current (EBIC) [Phi 86] measurements. However, the crystal structure of Cu₂Se₃ and its phase relation with Cu₂Se₃ is still not clear at this point.

1.3.4 Junction Formation

Junction formation is a critical step in fabricating a good photovoltaic device. The best results today for CIS-based PV have incorporated deposition of a thin CIS layer (~500 Å) by chemical bath deposition (CBD) [Kas 98]. Considerable effort has been directed towards understanding the mechanism responsible for this dramatic improvement of cell performance. Elucidation of the role of CBD CIS will lead to better device engineering and suggesting alternative processes. Several explanations have been proposed to account for the improved photovoltaic performance over other processes:

1. A polycrystalline nanofloral layer of suspended CIS requires thicker films to completely cover the rough CIS-absorber surface.
2. The liquid electrolyte chemical modifies the absorber surface:
 - Cd diffuses into CIS lattice forming $\text{Cd}_{1-x}\text{Cd}_{2x}\text{Se}_{1-x}\text{Se}_{2x}$ (or Cd on Cu sites) donor and induces a type conversion (p to n) [Kas 98]
 - Cd reacts with CIS surface forming CdSe , or CdS , CdS_2 , which produced a graded interface structure [Kas92]

The first effect has been commonly accepted as interfacial impurity. The chemical modification explanation appears to play a very crucial role in addition to the first three mechanisms. Intensive studies have been carried out in this area. Several proposed explanations based on the interfacial reactions between the CIS surface and the chemical bath. For example, it is suggested that exchange reactions at the rear-surface region between the CIS and the Cd or S ions in the chemical bath. Another proposed mechanism is washing or etching effect that removes soluble components (e.g., cadmium complex, a significant waste). The waste removal parallels upon dipping in the chemical bath has

been carefully studied [Kao 92]. In a more recent set of studies on the impact of the buffer layer process, the beneficial effects of a Cd postal electrolytic treatment on the CDS films. There were two interactions suggested for the Cd postal electrolytic treatment. One model [Kao 92] suggested that Cd ions react with the CDS surface and form a CdS_x or CdS_xSe_y compound, thus reducing the density of interface defects. The other suggested interaction is that Cd ions diffuse into the CdSeS_x buffer and form CdS_x droplets, thus reducing a type II structure [Kao 93]. The Cd doping model had been proposed by [Mac 91] for an evaporated-CdS/hexyle crystal CdSeS_x device. The true mechanism for the observed type conversion was not clearly resolved due to the complexity of the defect chemistry. Furthermore, the etching of the buffer compounds (eg. CdSeS_x) with the chemical bath could also be a significant factor for the reported high efficiency cell with the buried junction between CdSeS_x and CdSeS_x .

Impurities (e.g. O, N) in CDS CDS films have been reported [Kyl 91]. Several compounds such as, CuOHCl , CuCl , CuSCN , CuSO_4 , CuCO_3 , Cl⁻ and H_2S have been suggested. The disagreement for the impurity compounds depend on the region used for the bath and the difficulty in interpretation of the analysis results. The effects of impurities on the cell performance, however, are not clear as far.

1.1.3. Etching of Buffer Layers

Considerable effort has been devoted to find a replacement for the CDS CDS process in CIGS-based solar cells. This search has been directed towards developing a Cd-free process for environmental reasons, and a dry deposition process to make it more compatible with the remaining of manufacturing process. A variety of buffer layer materials have been tested as replacements for CDS, including ZnO , ZnS , Fe_2O_3 & GaN .

ZnO , In_2O_3 , O_2 , In_2O_3 , $\text{In}_2\text{O}_3/\text{O}_2$, $\text{In}_2\text{O}_3/\text{H}_2\text{S}$, ZnO , and ZnO all deposited by CVD. Other approaches include ZnO by vacuum layer spurt and ZnO by MOCVD. CVD solar cells with continuously evaporated Cd-free buffer layers In_2O_3 , Ga_2O_3 , and $\text{ZnO}_{x/2}\text{Ga}_{x/2}$ have also been demonstrated. Although, significant progress has been achieved in this area, these alternative buffer layer materials and processes still produce inferior CIGS-based PV cells, and some suffer from stability problems (e.g., $\text{In}_2\text{O}_3/\text{H}_2\text{O}$, $\text{ZnO}_{x/2}\text{Ga}_{x/2}$). The search for a better alternative buffer-layer process is still needed.

1.3.6 TCO layer

The role of the TCO layer is to effectively transport photo carriers generated by the absorber layer to the external circuit without the sacrifice of incident sunlight. ZnO is the common choice for the top contact. Criteria for the optimization of the ZnO film are low sheet resistance and high optical transmission. The figure of merit can be defined as the ratio of the electrical conductivity to the optical absorption coefficient of the film. RF sputtering or MOCVD are the two widely used deposition processes. The ongoing research for an improved TCO layer includes elucidation of the relation between microstructure (point and planar defects) and processing parameters used TCO materials and processes, and a thinner TCO layer.

1.4 Statement of Thesis Work

The objectives of this thesis are

1. Develop a limited thermodynamic description of the Cu-In-In system for better understand the processing chemistry of Cu-In-In absorber layer formation.

2. Apply the student knowledge of thermochemistry and phase diagrams to design novel processes suitable for synthesis of Cu₂S, discover ways to equal thermal process
3. Investigate the local structure of important copper sulfide minerals (intercalation alloys [Cu₂S], Cu₂S, Cu₂S) by EXAFS

CHAPTER 1 THEORY AND PROCEDURE FOR ADDRESSING THERMOCHEMISTRY AND PHASE DIAGRAM DATA

1.1 Introduction

Van Laar [Van 04] established the basis of calculating phase diagrams in 1901 by using a solution model to describe the Gibbs energy of solution phases and reciprocal 1 then ran the calculation with the introduction of large scale computational capabilities. This approach can now be applied to large scale systems. The CALPHAD method is characterized by the combination of Computer Calculations of Phase Diagram with experimental thermochanical and phase diagram data. The main output of this procedure is to generate useful phase equilibria and thermochanical information to solve problems in materials processing. In 1973 a group (CALPHAD) was organized to share experiences and further develop this approach [Lau 73]. Initially, systematic trial and error methodologies were used to adjust model parameters. As the computational power increased, it became possible to treat large data sets using formal parameter minimization algorithms. The first of these was created by Dr. H.L. Lukas [PROMIS and PROMET] and applicable to binary systems [Luk 75]. These programs allowed simultaneous adjustment of the model parameters to all types of measured data such as phase diagrams and thermochanical data, and to account for errors of measurement. Several sophisticated programs have been developed since then, including LUKAS [Luk 92], Thermo-Calc [Jan 90], MTDATA [Glas 90] and FACT [Pel 90].

3.1 Principle of Phase Diagram Calculation

Most computer-based calculations of phase diagrams are based on the principle of Gibbs' energy minimization and Maxwell's construction. On constant (isobar) construction, The Maxwell construction is a geometric interpretation of the solution for equilibrium conditions. Which are,

$$T_\alpha = T_\beta \quad (3.1)$$

$$P_\alpha = P_\beta \quad (3.2)$$

$$\mu_1^\alpha = \mu_1^\beta \quad (3.3)$$

$$\mu_2^\alpha = \mu_2^\beta \quad (3.4)$$

For a binary (components A and B) two-phase (phases α and β) system. An illustration of the construction is given in Figure 3.1

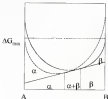


Figure 3.1 An illustration of Maxwell's construction

3.3 CALPHAD Approaches

The CALPHAD approach is based on three elements: data, models and software, as shown in Figure 3.2



Figure 3.2 Elements and functions of the Calphad approach

3.3.1 Data sets

The experimental data can be categorized as three standard types

- 1 Phase diagram data (e.g. liquidus, solvus)
- 2 Enthalpy data (e.g. ΔH_f , ΔH_{mix} , ΔH_{form} , C_p)
- 3 Gibbs energy data (e.g. activity, vapor pressure)

2.1.2 The models

A thermodynamic description of a system requires the assignment of thermodynamic functions for each phase. The CALPHAD method employs various models to describe the Gibbs energy as a function of temperature, pressure and composition.

2.1.2.1 Reference state

Energy quantities (e.g., enthalpy, Gibbs energy) can not be defined absolutely. Only their differences have a physical meaning. By convention, the enthalpy for an element in its stable state at 298.15 K and 1 bar (H_{298}) is assigned the value zero. The use of this reference for data is called *Sub's Element Reference* and denoted SER, and the enthalpy is sometimes denoted H_{298} .

2.1.2.2 Models for phases with fixed composition

A pure element and a low compound cannot vary in composition and thus its Gibbs energy is as a function of temperature and pressure only. For such phases the Gibbs energy is expressed as

$$G-H_{298} = a + bT + cT \ln T + dT^2 + eT^3 + fT^4 \quad (2.5)$$

2.1.2.3 Models for solution phases

The Gibbs energy for a solution phase can be divided into three contributions as the following equation

$$G = G^S + G^M + G^E \quad (2.6)$$

Where G^S corresponds to the Gibbs energy of a mechanical mixture of the constituents of the phase, G^M is the entropy of mixing for an ideal solution, and the term a and G^E is the excess Gibbs energy which accounts for the departure from ideal mixture behavior.

Many models have been developed to describe the miscibility including the regular solution model, associated model, lone model, group-theoretical model, incremental model and valence models.

One commonly used model is the Redlich-Kister formalism. The Gibbs energy G for a binary solution is expressed as

$$G = RT \{ x_1 \ln x_1 + x_2 \ln x_2 + x_1 x_2 \sum_{j=0}^n \frac{L_j}{T^j} (x_2 - x_1)^j \} \quad (2.7)$$

where x_1 and x_2 are mole fractions of elements A and B and L_j is a function of temperature, according to

$$L_j = a_j + b_j T + c_j T \ln T \quad (2.8)$$

Detailed discussions of these various models can be found in [Bun 90]. Recently efforts have been directed to introduce ab-initio calculations of phase diagrams into the CALPHAD community [Aul 90], like the Cluster Variation Method (CVM) or Monte Carlo (MC) calculations [Fon 90]. These methods are based on knowledge of the system configuration and accompanying electronic structure calculations, previous to being more simple into appropriate solution models for systems that are difficult to probe experimentally.

2.3.3 Software

Two major algorithms are involved in the calculations: one is the optimiser based on the Gaussian least squares method and the other is Newton-Raphson method. The software calculates the phase diagrams as well as thermodynamic functions by using the

optimized Gibbs energy function data the optimizer. The input to the assessment is thermodynamic and phase equilibrium data; the output is optimized expressions for the Gibbs energy of each phase. The calculation flowchart is given in Figure 2.3.

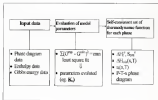


Figure 2.3 Calphad thermodynamic assessment flowchart

CHAPTER 1 THERMODYNAMIC ASSESSMENT OF TELLURIUM UNARY SYSTEM

1.1 Introduction

For the thermodynamic assessment of phase diagrams, the phase stability of the pure components are required. Furthermore knowledge of the vapor phase composition is important in process planning. Therefore reliable G-Helmholtz expressions for the condensed and gaseous tellurium species are necessary. Critically assessed G-Helmholtz expressions for the tellurium species however are lacking in the literature. For this reason, the thermodynamic properties of Te (α -hexagonal), Te (β) and Te_2 (g) [ref.1-4], including $\Delta H^\circ_{f,298.15}$, $S^\circ_{298.15}$, and $C_p(T)$ were assessed. Using these properties the G-Helmholtz expressions for each phase of tellurium were produced. The temperature dependence of vapor pressure and composition for $\text{Te}_2(g)$ in equilibrium with condensed tellurium were also calculated from equilibrium constants for $\text{Te}_2(g)$ and compared with experimental data.

1.2 Literature Review

1.2.1 Solid state

Three modifications of solid tellurium have been reported: hexagonal, monoclinic and amorphous tellurium. Hexagonal tellurium is taken as the stable standard state. The heat capacity of hexagonal tellurium had been reported by many authors, which were

reported by Claus *et al.* [Cla 84]. The earlier assessments by Holgren [Hol 71], Mills [Mil 76] and KYTE [Kye 84] did not include the heat capacity data from [Cla 73] and [Cla 74]. No experimental data are available for the solid selenium experienced above its melting point, therefore only an assessment can be made for the superheated heat capacity.

The value of W_{ex} was evaluated by both [Cla 84] and [Kye 84], with the value by Claus *et al.* [Cla 84] lower. This discrepancy was produced by the fact that the heat capacity data measured by Chang and Bental [Cha 74] in the range of 4 to 70 K was used by Greenwell *et al.* [Gra 84] but not by Claus *et al.* [Claus 84], who used Brannon and Lippman's [Bry 73] data instead. The nearest value by Greenwell *et al.* [Gra 84] is adopted in this work.

3.2.2 Liquid state

Several investigators have measured the heat capacity of liquid selenium. The data from Mandan-Mandari [Man 56], Jorgens [Jor 67], and Goffow and Hensch [Gof 74] are in poor agreement. The later measurements by [Gra 75], [Cha 74], [Mil 76], and [Kye 80] are in better agreement. They investigated the heat capacity from the superheated region (400 to 444 K) to 1000 K. The assessed liquid selenium heat capacity, $C_p(T)$, along with the experimental data are shown in Figure 3.2. The heat capacity decreases in the temperature range 400 to 750 K, with a subsequent increase to 1000 K. This complex behavior is due to vibrational energy contributions, first volume effects and later of structure from the change to ring-chain equilibria and depolymerization equilibria, which have been studied by Sha *et al.* [Sha 80]. No experimental data were available for the temperature above 1000 K. Constant heat capacity

values were used above the temperature in both NIST [Dec 71] and NISTAI [Dec 76] databases.

7.2.1 Gaseous Phase

Similar to sulphur, selenium exhibits a complex composition in the vapor phase. The mass spectrometric measurements have shown the presence of all the molecules from monomer to S_8 species, the more abundant ones being S_2 through S_6 . Studies of the complex structure of selenium vapor have been performed by a variety of methods. These include vapor density [Hil 27], and [Ros 74], torsion or Raman effluent measurements [Yam 37], [Ros 42], [Kil 71], optical absorption [Ros 45], and mass spectrometry [Dec 44], [Ros 46], [Yam 27], [Ros 70], [Haj 66], [Ros 61], [Ros 66], [Kil 71], [Ste 72], [Ros 44], [Dec 44], [Ros 45], [Ros 71], and [Gra 74]. Mills [M2 74] reviewed the data available before 1974. Then Grossel et al. [Dec 84] assessed the $\Delta H_{f,298}$, molecular constants and thermodynamic functions for selenium monomers and dimers. Koschel [Kos 84] calculated the thermodynamic functions for S_n molecules from spectroscopic and structural data. The entropy and heat capacity data for cyclic S_n ($n=3,4,7$) molecules were obtained from linear relationships between \log rate α , entropy, and heat capacity values of S_2 and S_6 . Ros [Ros 81] calculated the thermodynamic functions for S_n ($n=3$ to 7) from molecular constants derived from the data of S_2 , S_4 and S_6 ($n=2$ to 8).

3.1 Assessment

3.1.1 Solid state

The $C_p(T)$ expression for solid hexagonal selenium was modeled as $C_p = a + bT + cT^2$ and the parameters were estimated using the experimental data of [Geo 73] and [Chi 74]. The coefficients are given in Table 3.10. For the supercooled solid selenium the heat capacity was simply extrapolated to a constant value based on the polynomial expression at 298 K where the $C_p(T)$ curve reaches its maximum value of 28.55 J/K.mol. The coefficients for G-Helm derived from $C_p(T)$ expressions using the entropy value $S^\circ_{298.15} = 41.27$ J/K.mol by Giauque *et al.* [Geo 34] are given in Table 3.11. The plot of C_p vs. T along with experimental data is shown in Figure 3.1. The reported values for the heat of fusion are widely divergent [old 74]. The experimental value $\Delta H_{fus} = 41.58$ kJ/mol reported by Giauque [Geo 34] was used here.

3.1.2 Liquid state

the liquid state heat capacity $C_p(T)$, was expressed as one equation ($C_p = a + bT + cT^2$) using the experimental data measured by [Geo 71], [Chi 74], and [Sta 80] from the supercooled state 298 to 404 K to 1400 K. No experimental data are available for temperatures higher than 1400 K. The extrapolation was carried out by assuming the $C_p(T)$ based the polynomial expression curve to a constant value 36 J/K.mol at 1700 K. The fitted heat capacity expression is shown in Table 3.12. C_p and G-Helm vs. T plots with experimental data and NIST (JANAF) database are given in Figure 3.2 and 3.3 respectively.

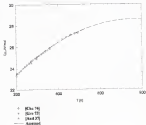


Figure 3 | Fitted bond capacity data for horizontal release along with experimental data

3.3.3-Data sources

Grossel *et al.* [Gro 84] have critically assessed the standard enthalpy of formation and thermodynamic functions for the monomer and dimer. Their data are adopted here. For Se_n ($n=2$ to 8), Grossel and Szwarc [Gro 84] and Keller [Kel 70] calculated the value of S°_{298} . The molecular constants calculated by Keller [Kel 70] are based on rough approximations. No information was given in [Gro 84] concerning the molecular structure and vibrational frequencies used in their calculations. The heat capacity data listed in Mills [Mil 74] and also [Bar 74] are based on the data in [Gro 84] and [Kel 70] respectively. Barin [Bar 71] estimated the vibrational frequencies, product of wavenumbers of the Se_n molecules ($n=2$ to 7) from the molecular constants of Se_2 and Se_3 , Se_4 [Gro 84] [Gro 84], and [Ste 41] based on the Molecular-Orbital or a Linear Combination of Atomic Orbitals (MO-LCAO) method. Nagata *et al.* [Nag 61] assigned the complete vibrational spectra for Se_2 , from Raman and IR measurements. The estimated frequencies by Barin [Bar 71] and the experimental values determined by Nagata *et al.* [Nag 61] for Se_2 are in good agreement. The molecular constants listed by Barin [Bar 71] together with the data by Nagata *et al.* [Nag 61] are adopted to calculate the thermodynamic functions for Se_n ($n=2$ to 8), assuming harmonic oscillator-rigid rotator and ideal gas behavior.

The values of standard enthalpy of formation for Se_n ($n=2$ to 8) were interpreted by several authors employing various techniques. The partial pressures resulting from the electrochemical Knudsen cell by Keller *et al.* [Kel 71] are more accurate than those from conventional mass-spectrometric investigations, especially for small molecules (Se_2 , Se_3 and Se_4) which can be formed by fragmentation of large molecules even at the lowest

energy. The electrochemical Koutecky-Levich slope present can be better distinguished. When the logarithm of the ion intensity in the mass-spectrometry is plotted against the potential, the different species should have different slopes. Only they which are in agreement with the theoretical value, are then thought to be the parent ion intensity. The vapor density measurements by [28-32] only included the even numbered species in the vapor than the others are disregarded. Rao [Rao 74] measured the vapor density and total vapor pressure over liquid selenium and optimized the thermodynamic properties the enthalpies and entropies of Se_n , for 2 to 4, by fitting the vapor pressure and density data. Therefore the set of thermodynamic properties for Se_n , listed by [Rao 74] do not lead to independent values.

To evaluate the standard enthalpies of formation for Se_n , for 2 to 4, the calculated thermodynamic functions are used to perform statistical low and third law analysis of the experimental data. The average total pressure by Newman and Luthinberg [New 34] and Wenz and Sheline [Wen 42] over solid selenium is used to calculate the partial pressure in third law analysis. The measurements for each species is listed below.

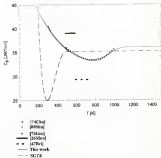


Figure 3.3: Molar heat capacity for liquid indole along with experimental data

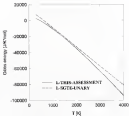


Figure 3.3 Assessed G-Fluxes for Secondary system as comparison with the RTDE database.

3.3.3.3a

The evaluated values of standard enthalpy of formation for $\text{Se}_2(\text{g})$ from [Sta 34], [Mol 34], and [Gre 34] are listed in Table 3.1. Greenhalgh *et al.* [Gre 34] had actually evaluated the standard enthalpy of formation and dissociation energy data of $\text{Se}_2(\text{g})$ gas. They had used these data to calculate the standard enthalpy of formation for $\text{Se}_2(\text{l})$ gas. Their assessed value, $\Delta H_{\text{f,298}}^\circ = 271.41 \text{ kJ mol}^{-1}$, is adopted.

Table 3.1: Standard enthalpy of formation data for Se_2 .

Authors	$\Delta H_{\text{f,298}}^\circ$ (kJ/mol)
[Sta 34] and [Mol 34] ([Sta 34])	269.4 ^{±5}
[Mol 34] ([Mol 34])	273.12
Greenhalgh <i>et al.</i> [Gre 34]	271.41 ^{±0.47}

The entropy data listed in [Sta 34], [Mol 34], [Mol 34], and [Gre 34] are consistent. The value $S_{\text{f,298}}^\circ = 176 \text{ J K}^{-1} \text{ mol}^{-1}$ was adopted in this work. The heat capacity data from different authors are shown in Figure 3.5. The heat capacity data from [Gre 34] have been fitted with $C_p(T)$ expressions with one break point according to the shape of the $C_p(T)$ curves. Results of $C_p(T)$ and $G-H_{\text{f,298}}(T)$ are presented in Tables 3.10, 3.11 and Figure 3.6 respectively.

3.3.3.3b

The value of the heat of formation of $\text{Se}_2(\text{g})$ has been assessed by many authors [Sta 34], [Mol 34], [Mol 34], [Gre 34], [Van 37]. The critical assessed value, $\Delta H_{\text{f,298}}^\circ = 164.14 \text{ kJ mol}^{-1}$, by Greenhalgh *et al.* [Gre 34] is adopted here. The entropy and heat capacity data calculated from the molecular constants were published by [Sta 34], [Mol 34], [Mol 34], [Gre 34], [Rau 74], and [Van 37]. The reported heat capacity data are

shown in Figure 3.5. The least-squared data from [Oro 94] are adopted here. Two equations are used to fit the complex shape of the heat capacity curve. The equations and plots of $C_p(T)$ and $C_p/\text{Rgas}(T)$ are given in Table 3.16, 3.17 and Figure 3.6.

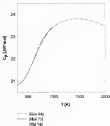


Figure 3.4 reported heat capacity for Se(g) in the range $T=774$ to 2000 K

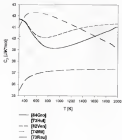


Figure 3.1 Heat capacity for $\text{Si}_3(\text{g})$ at the range $T=400$ to 2000 K.

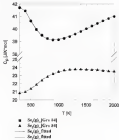


Figure 3-6: Fitted heat capacity for $\text{Se}_2(\text{g})$ and $\text{Se}(\text{g})$ in the range 500–2000 K.

1.3.3.5a) Se_2

The values of the standard enthalpy of formation obtained from various investigations for Se_2 are listed in Table 3.2. The data are calculated from assessed thermodynamic functions by second and third law methods.

Table 3.2 Standard enthalpy of formation data for $\text{Se}_{0.5g}$

Authors	Method	$\Delta H^\circ_{\text{form}}$ (kJ/mol)
Endrey and Chapka [End 46]	Mass spectrometry	137.83 \pm (1)
Keller et al. [Kel 71]	Mass spectrometry and Electrochemical Knudsen cell	145.59 \pm (1) 151.44 \pm (18)
Ross [Ros 74]	Vapour density measurements	140.74
Huang et al. [Hua 84]	Mass spectrometry	138.66 \pm (1) 144.16 \pm (18)

II: Second Law Value, III: Third Law Value

The values derived from conventional mass-spectrometric studies [End 46] [Hua 84] are lower than those by Keller et al. [Kel 71]. The reason for such discrepancy can be ascribed to fragmentation of larger molecules. The electrochemical Knudsen cell used by Keller et al. [Kel 71] is more reliable for the study of smaller Se gas molecules than conventional mass spectrometer. The third law values by [Kel 71] are self-consistent with a standard deviation of 0.26 kJ/mol and also agree with the second law value. Thus the third law value $\Delta H^\circ_{\text{form}} = 151.44 \pm 0.26$ kJ/mol, by [Kel 71] was selected. The entropy value, $S^\circ_{\text{form}} = 213.80$ JK/mol, calculated by [Ros 74] is adopted in this work. Figure 3.7 shows the assessed $C_p(T)$ along with data from other authors. The results of assessed $C_p(T)$ and $\Delta H^\circ_{\text{form}}(T)$ are given in Tables 3.10 and 3.11, respectively.

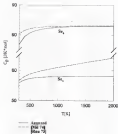


Figure 3.7 Assumed heat capacity for $\text{Sn}_4(\text{g})$ and $\text{Sn}_2(\text{g})$ in the range $T=298$ to 2000 K.

3.3.3.4 Δ_{vap}

The values of the standard enthalpy of formation obtained from various investigations are listed in Table 3-3. The entropy value, $S^\circ_{298} = 143.10 \text{ J/K mol}$, reported by [Rus 71] is used in this work.

Table 3-3 Standard enthalpy of formation data for Ba_2 (g)

Authors	Method	$\Delta H^\circ_{\text{f,298}}$ (kJ/mol)
Keller et al. [Kel 71]	Mass spectrometry and Electrochemical & sodium cell	119.88 (13) 167.27 (18)
Δ_{Ba} [Rus 71]	Vapor density measurements	158 (4)
Greenley et al. [Gre 62]	Angular distribution mass spectrometry	119.68 (48) 149.45 (10)
Shaw et al. [Shw 64]	Mass spectrometry	114 (8) (B) 145.38 (11)

B: Second law value, 18: Third law value

As with Ba , the standard enthalpy of formation values reported by [Gre 62] and [Shw 64] are lower than the values of Keller et al. [Kel 71] due to the fragmentation of larger molecules. Although the experimental methods used by [Kel 71] are more reliable in general, the third law analysis shows a standard deviation 3.58 kJ/mol. And the second law value seems to be too large. The standard enthalpy of formation value for Ba_2 needs further refinement. Ba_2 , however, is not a major component in the vapor phase in equilibrium with condensed selenium. It is not essential to select the total vapor pressure or density. An approximation through total vapor pressure is clearly that it is not reliable. Thus, standard law value: $\Delta H^\circ_{\text{f,298}} = 167.27 \pm 5.77 \text{ kJ/mol}$, reported by [Kel 71] is selected.

here. Figure 3-7 shows the assessed $C_p(T)$ along with data from other authors. The results of the assessed $C_p(T)$ and $G_{\text{fuss}}(T)$ are given in Tables 3-10 and 3-13, respectively.

3.3.3 S_{fuss}

The values of the standard entropy of formation obtained from various investigations are listed in Table 3-4. The entropy value, $S_{\text{fuss}}^{\circ} = 415.56 \text{ J/K mol}$, reported by [Kus 94] is adopted in this work.

The third law values derived from [Bar 60], [Pig 60], [Kus 92], [Pus 94], [Kus 94] are in good agreement. The third law value derived from [Kil 73] with a standard deviation of 2.71 kJ/mol seems to be too high. From the mass-spectrometric studies it is known that Se_2 is a major species in equilibrium with liquid selenium in the temperature range 500–1000 K. The standard enthalpy of formation value for Se_2 can be assessed by the total vapor pressure data in equilibrium with liquid selenium in the temperature range 500 to 1000 K. The vapor pressure data by [H 57], [Kus 94], and [Kil 67] are in good agreement within this temperature range. These data are used to perform the optimization. The calculation is performed by using the assessed G_{fuss} equations for liquid selenium and gaseous Se_2 (see 3-8 except 3) to calculate the partial pressures for each species. And the partial pressure for Se_2 is obtained by subtracting the partial pressures of Se_4 (see 3-8 except 3) from the total vapor pressure. Since the enthalpy of formation value for Se_2 is uncertain, the value was changed from 140 to 170 kJ/mol in calculating the partial pressure for Se_2 . The Peng-Robinson equation-of-state is used for real gas corrections and the ideal mixture behavior is assumed. The calculated results show the ΔH_{fuss} for Se_2 equal 153.45 to 153.79 kJ/mol when ΔH_{fuss} for Se_4 changes from 133 to 140 kJ/mol. The mean value of $\Delta H_{\text{fuss}} = 153.62 \pm 0.17 \text{ kJ/mol}$ is selected.

Table 3.4: Standard enthalpy of formation data for $\text{Sn}(\text{gl})$

Authors	Method	$\Delta H_{\text{f,298.15}}^{\circ}$ (kJ/mol)
Barin et al. [Bar 68]	Mass spectrometry	150.30 (1)
		152.87 (38)
Poppe et al. [Pop 68]	Mass spectrometry	154.50 (1)
		152.99 (38)
Yamaguchi and Porter [Yam 77]	Mass spectrometry	145.34 (1)
Keller et al. [Kel 79]	Mass spectrometry and Electrochemical freezing cell	144.96 (1)
		150.24 (38)
Lee [Lee 74]	Single crystal calorimetry	148.90
Moore et al. [Mo 75]	Mass spectrometry	151.21 (1)
Ginsley et al. [Gin 76]	Appar. distribution mass spectrometry	148.88 (1)
		151.24 (38)
Chung et al. [Ch 74]	Mass spectrometry	151.89 (1)
		151.24 (38)
Grewat et al. [Grew 74]	Mass spectrometry	147.75 (1)
		152.40 (38)

1) Second law value, 2) Third law value

Figure 3.1 showed the estimated $C_p(T)$ along with data from other authors. The results of estimated $C_p(T)$ and $G-\text{Hess}(T)$ are given in Tables 3.5 and 3.6, respectively.

3.3.3.4 ΔG_0

The values of the standard enthalpy of formation obtained from various investigations are listed in Table 3.5. The entropy value, $S_{\text{298}}^{\circ} = 118.73$ J/(mol.K), was calculated from the molecular constants listed by [Bar 74] and [Pop 71].

The third law values of $\Delta H_{\text{f,298}}^{\circ}$ derived from the data of [Bar 68], [Pop 68], [Bar 67], [Yam 77], [Mo 75], and [Gin 76] are in relatively good agreement. The third law and second values by [Kel 71] are well-consistent with a standard deviation value of 0.23 kJ/mol, however smaller than values are ΔG_0 [2] or the most prominent species in

equilibrium with solid selenium. It was found the calculated $\ln a_2(g)$ vapor pressure from the value by [Ref. 70] is higher than the total pressure in equilibrium with solid selenium as measured by [Yam. 77], [Niu. 30], [Niu. 40] and [Choi. 35] using a torsion-effusion measurement. On the other hand the $\ln a_2(g)$ vapor pressure calculated from the mass ΔH_{298} value from [Bar. 46], [Bar. 75], [Fuj. 44], [Ots. 82], [Niu. 44] and [Ito. 84] is consistent with these experimental measurements. Thus, the mean value $\Delta H_{298} = 143.38 \pm 3.47$ kJ/mol, is selected here. Figure 3.4 showed the calculated $C_p(T)$ along with data from other authors. The results of $C_p(T)$ and $G-H_{298}(T)$ are given in Tables 3.10 and 3.11, respectively.

Table 3.5 Standard-enthalpy of formation data for $\ln_2(g)$

Authors	Method	$\Delta H_{298}^{0, ex}$ (kJ/mol)
Barinowicz and Chapka [Ref. 44]	Mass spectrometry	145.95 (II)
Fujimaki et al. [Fuj. 44]	Mass spectrometry	143.47 (III) 148.70 (III')
Yamashita and Porter [Yam. 77]	Mass spectrometry	145.47 (II)
Barinowicz and Radzisz [Ref. 52]	Mass spectrometry and electrochemical Krypton-cell	137.92 (II)
Keller et al. [Ref. 70]	Mass spectrometry and electrochemical Krypton-cell	137.60 (II) 138.60 (III)
Ito [Ref. 84]	vapor density measurements	144.27
Herman et al. [Ref. 77]	Mass spectrometry	143.47 (III)
Granby et al. [Ref. 82]	Regular-distribution mass spectrometry	143.40 (II) 144.76 (III)
Huang et al. [Ref. 49]	Mass spectrometry	143.13 (II) 144.20 (III)
Ortiz-Martí et al. [Ort. 84]	Mass spectrometry	137.18 (II) 140.74 (III)

II: Second low-value III: Third low-value

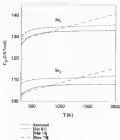


Figure 3-8 Heat Capacity of $Se_2(g)$ and $Se_3(g)$ in the range $T=0$ to 2000 K.

3.3.3 T, Se_2

The values of the standard enthalpy of formation obtained from various investigations are listed in Table 3-6. The average value, $H^\circ_{298} = 491.16 \text{ kJ/mole}$ from [Run 7]) is entered here. The third law values derived from [Ref. 11] are insufficient

with a standard deviation value 0.38 kJ/mol and agree well with the second law value. The value $\Delta H_{\text{Lam}}^{\circ} = 949.48 \pm 0.40$ kJ/mol is selected. Figure 3-5 shows the evaluated $C_p(T)$ data along with data from other authors. The results of $C_p(T)$ and $G_{\text{Hess}}(T)$ are given in Tables 3-10 and 3-11, respectively.

Table 3-4 The standard enthalpy of formation data for $\text{Se}_{1/2\text{Lam}}$

Authors	Method	$\Delta H_{\text{Lam}}^{\circ}$ (kJ/mol)
Bartolomé and Chapuis [Bar 90]	Mass spectrometry	118.48 (11)
		152.48 (18)
Pignault <i>et al.</i> [Pig 66]	Mass spectrometry	164.33 (11)
		152.11 (17)
Yonakagui and Fourni [Yon 77]	Mass spectrometry	155.25 (11)
Keller <i>et al.</i> [Kel 71]	Mass spectrometry and Electrochemical bromine cell	146.45 (11)
		145.14 (10)
Rau [Rau 79]	Vapor density measurement	172.72
Hopwood <i>et al.</i> [Hop 75]	Mass spectrometry	152.48 (11)
Grandy <i>et al.</i> [Gra 72]	Argon-helium/argon mass spectrometry	149.29 (11)
		152.18 (10)
Huang <i>et al.</i> [Hua 84]	Mass spectrometry	159.48 (11)
		152.19 (10)
Drowart <i>et al.</i> [Dro 58]	Mass spectrometry	150.45 (10)
		152.57 (11)

(1) Second law value. (2) Third law value.

3.1.3.3 ΔG_p

The values of the standard enthalpy of formation obtained from various investigations are listed in Table 3-7. The entropy value $S_{\text{Lam}}^{\circ} = 532.29$ J/mol.K from [Rau 79] is used here.

The third law values derived from [Kel 70] are self-consistent, with a standard deviation of 0.28 kJ/mol, and agree well with the second law value. Thus, the value $\Delta H_{\text{Lam}}^{\circ} = 150.02 \pm 0.11$ kJ/mol, is selected in this work. Figure 3-7 shows the evaluated

$C_p(T)$ data along with data from other authors. The results of $C_p(T)$ and $\Delta H_{\text{fusion}}(T)$ are given in Tables 3.10 and 3.11, respectively.

Table 3.7 The standard enthalpy of formation data for $\text{Sn}_2(\text{g})$

Authors	Method	$\Delta H^\circ_{\text{f,Sn}_2(\text{g})}$ (kJ/mol)
Endrey and Chapka [Ref. 64]	Mass spectrometry	170–194 (II) 179(2) (III)
Papadimitriou [Ref. 65]	Mass spectrometry	170–187 (II) 171(60) (III)
Yamashita and Foster [Ref. 67]	Mass spectrometry	171–201 (II)
Keller et al. [Ref. 71]	Mass spectrometry and electrochemical ionization cell	158–74 (II) 158(50) (III)
Bain [Ref. 74]	Vapor density measurements	169–20
Hosoya et al. [Ref. 74]	Mass spectrometry	174–15 (II)
Courtney et al. [Ref. 87]	Angular distribution mass spectrometry	150–80 (II) 161(44) (III)
Huang et al. [Ref. 84]	Mass spectrometry	161–26 (II) 161(4) (III)

II: Second-law value; III: Third-law value

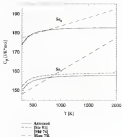


Figure 5.1 Heat capacity of $\text{Se}(\text{g})$ and $\text{Se}(\text{l})$ in the temperature range 298–to 2000 K

5.4 Vapor Pressure and Components in Equilibrium with the Confined Phase

Several authors have investigated the vapor pressure in equilibrium with confined solvent using a variety of techniques. Garswold *et al.* [20a, 24] has reviewed the data published through 1984. The equilibrium partial pressures in equilibrium with

the condensed phase are calculated using the standard G-Hugg equations for the condensed and gaseous state listed in Tables 3.11 and 3.13, respectively. The Peng-Robinson equation of state, which is commonly used for organic gases, is included to calculate the density coefficient and compressibility for real gas mixtures. The generalized form of the Peng-Robinson equation of state is

$$P = \frac{RT}{V-b} - \frac{a(T)}{V(V+b)} + \frac{a(T)b}{V^2(V+b)^2} \quad (3.1)$$

With

$$a(T) = a_c [1 + (1 - \sqrt{T_r})^2] \quad (3.2)$$

$$T_c = 377.32 \text{ K} \quad (3.3)$$

$$b_c = 0.07781 \text{ L mol}^{-1} \quad (3.4)$$

$$a(T) = 0.42724 \frac{R^2 T_c^2}{P_c} \alpha(T) \quad (3.5)$$

$$b = 0.07780 \frac{R T_c}{P_c} \quad (3.6)$$

$$\sqrt{\alpha} = 1 + \omega(1 - \sqrt{\frac{T_r}{T_c}}) \quad (3.7)$$

$$\omega = 0.37464 + 1.54226\omega_1 - 0.26992\omega_1^2 \quad (3.8)$$

$$\omega = -0.8 - \log_{10} [P_r^{\text{sat}} (T_r = 0.7) / P_c] \quad (3.9)$$

Here $P_r^{\text{sat}} (T_r = 0.7)$ is the equilibrium vapor pressure of the fluid at reduced temperature $T_r = T/T_c = 0.7$. The critical properties of selenium were determined by Hultine et al. [Hult 74]. The ideal mixture behavior is assumed. Hence the density coefficient, $\phi_i (p) = \phi_i$, and compressibility, $Z_i (p) = Z_i$, are equal for all different species and depend on only the total pressure and temperature. The results for compressibility and density coefficient at different temperature are listed in Table 3.6.

Table 3.3 Compressibility and fugacity coefficient for selenium vapor in the temperature range -100 to 1500 K.

Temperature K	Compressibility Z	Fugacity coefficient ϕ
500	1.000000	1.000000
600	0.999993	0.999999
700	0.999987	0.999999
800	0.999982	0.999999
900	0.999976	0.999999
1000	0.999971	0.999999
1100	0.999967	0.999999
1200	0.999963	0.999999
1300	0.999960	0.999999
1400	0.999957	0.999999
1500	0.999955	0.999999

The calculated partial pressures over solid and liquid selenium are given in Figures 3.10 and 3.11, respectively. The calculated total pressure in equilibrium with solid and liquid selenium with experimental data is shown in Figures 3.12 and 3.13. The calculated vapor compositions show that Se_2 is the major species in equilibrium with solid selenium, and Se_2 , Se_3 , along with Se_4 are the major species over liquid selenium up to 100 K. At higher temperatures Se_2 is the dominant species. This work is consistent with the experimental reports by [Bro 44], [Bro 46], [Bro 70], [Tay 66], [Ott 61], [Pau 64], [Bro 44], [Kot 51], [Bro 70], [Bro 74], and [Pau 52]. The calculated equilibrium vapor compositions over solid and liquid selenium are given in Figures 3.14 and 3.15, respectively.

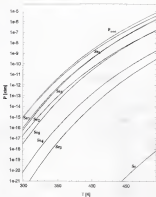


Figure 3.18 Equilibrium vapor pressure over solid nitrous tetroxide in the temperature range 310–410 K.

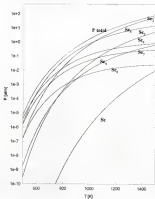


Figure 3.11: Equilibrium vapor pressure over liquid silicates in the temperature range $T=400$ to 1500 K.

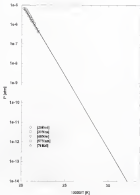


Figure 3.12: Experimental and estimated total vapor pressure over benzene solid phase (benzene) at $T=280$ to 320 K.

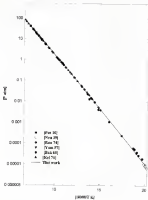


Figure 3.13 Experimental and assessed total vapor pressure over liquid cadmium in the temperature range 10% to 1 000 K.

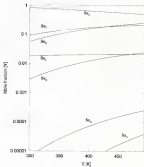


Figure 3-14 Equilibrium solute vapor composition over binary solid solution in the temperature range 380 to 460 K.

from [3] 1991

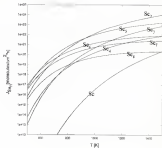


Figure 3. (a) Calculated flux versus temperature, (b) flux from input relative abundances.

3.3 Eyring Calculations for a Truly Expositive Source

The thermodynamic functions presented in this chapter were used to estimate the Langmuir exponents for these calculations as well as characterizing the performance of an expositive source. The Hertz-Langmuir equation

$$J_{\text{ex}} = \alpha R_s P_{\text{ex}} / \sqrt{2\pi M_{\text{ex}} RT} \quad (3.7)$$

was used where

- α = evaporation coefficient
- R_s = Langmuir's number
- P_{ex} = partial pressure of $\text{In}_n(\text{g})$
- M_{ex} = molecular weight of $\text{In}_n(\text{g})$

The evaporation coefficient for $\text{In}_n(\text{g})$ were related by Huang *et al.* (Hua-84) for molten indium at 500 K. They reported the evaporation coefficients of about 0.1 for all species $\text{In}_n(\text{g})$ for $n = 1$ to 5. Their data were re-evaluated by Brown *et al.* (Bro-84) who decreased the α -value for each of the $\text{In}_n(\text{g})$ species. Their result was adopted in this calculation. The temperature dependence of α is neglected in this calculation since no data are available for other temperatures. The calculation results are given in Figure 3.16.

3.4 Conclusions

In the present work, the thermodynamic properties for condensed and gaseous indium have been critically evaluated. Entropy and heat capacity data for gaseous phase species $\text{In}_n(\text{g})$ were calculated from molecular constants. The obtained Gibbs energy functions were used to perform the *ab initio* calculations for the enthalpy of formation values of each $\text{In}_n(\text{g})$ ($n = 1$ to 5). The enthalpy of formation value of In_1 is critical assessed using the selected equilibrium vapor pressure in equilibrium with liquid indium due to the disagreement between the literature data. The new set of Gibbs energy functions show

analytical accuracy is needed and third law evaluations for standard enthalpies of formation for $\text{Ba}_2\text{Cl}_2(g)$ ($x=0$). This was a problem in previous evaluation as discussed by Barakat *et al.* [2004]. The vapor pressures obtained from equilibrium calculations are well within the experimental results.

Table 3.9 Assessed heat capacity for condensed solutions

Phase	Temperature Range (K)	Coefficients in $C_p(T)$ expression $C_p = a + bT + cT^2 + dT^3$
Solid	298.15 – 494.5	$a = 19.140$ $b = 1.408 \times 10^{-3}$ $c = -1.406 \times 10^{-7}$
„	494.5 – 760	$a = 19.140$ $b = 1.408 \times 10^{-3}$ $c = -1.406 \times 10^{-7}$
„	760 – 1200	$a = 23.10$
Liquid	298.15 – 494.5	$a = 32.460$ $b = 4.581 \times 10^{-3}$ $c = 1.225 \times 10^{-7}$
„	494.5 – 1000	$a = 32.460$ $b = 4.581 \times 10^{-3}$ $c = 1.225 \times 10^{-7}$
„	1000–1150	$a = -5.240$ $b = 7.055 \times 10^{-3}$ $c = 3.121 \times 10^{-7}$
„	1150–1900	$a = 30.00$

Table 3.10 Assessed heat capacity for gaseous solutions

Species	Temperature Range (K)	Coefficients in $C_p(T)$ expression $C_p = a + bT + cT^2 + dT^3$
Ar	298.15 – 1000	$a = 19.560$ $b = 1.322 \times 10^{-3}$ $c = -3.071 \times 10^{-8}$ $d = 4.526 \times 10^{-12}$
„	1000 – 2000	$a = 23.236$ $b = 1.400 \times 10^{-3}$ $c = -1.918 \times 10^{-7}$ $d = -1.560 \times 10^{-11}$
Ba ₂	298.15 – 1000	$a = 17.800$ $b = 4.363 \times 10^{-3}$ $c = 1.476 \times 10^{-7}$ $d = -8.294 \times 10^{-12}$
„	1000 – 2000	$a = 24.046$ $b = 8.275 \times 10^{-3}$ $c = 4.647 \times 10^{-7}$ $d = -1.214 \times 10^{-11}$
Ca ₂	298.15 – 2000	$a = 29.593$ $b = 2.373 \times 10^{-3}$ $c = -8.880 \times 10^{-8}$ $d = -1.560 \times 10^{-11}$
Ca ₂ „	298.15 – 2000	$a = 32.576$ $b = 8.497 \times 10^{-3}$ $c = -1.430 \times 10^{-7}$ $d = -5.213 \times 10^{-11}$
Ca ₂ „	298.15 – 2000	$a = 32.750$ $b = 1.659 \times 10^{-3}$ $c = -1.758 \times 10^{-7}$ $d = -4.871 \times 10^{-11}$
Ca ₂ „	298.15 – 2000	$a = 32.728$ $b = 3.423 \times 10^{-3}$ $c = -4.413 \times 10^{-7}$ $d = 5.783 \times 10^{-11}$
Ca ₂ „	298.15 – 2000	$a = 37.581$ $b = 8.376 \times 10^{-3}$ $c = -1.334 \times 10^{-7}$ $d = -2.882 \times 10^{-11}$
Ca ₂ „	298.15 – 2000	$a = 40.446$ $b = 4.336 \times 10^{-3}$ $c = 1.439 \times 10^{-7}$ $d = -7.843 \times 10^{-12}$

Table 3.11 Gibbs energy relative to H_2O of condensed substances

Phase	Temperature Range (K)	Coefficients in $G(\text{J mol}^{-1})$ expression $G(\text{J mol}^{-1}) = A + BT + CT \ln T + DT^2 + ET^3 + FT^4$ (calculated)
Solid	258.15 – 494.3	$A = -1607$ $B = 92.12589$ $C = -18.34$ $D = -0.001194$ $E = 0.2671 \times 10^{-5}$ $F = 0$
"	494.3 – 750.4	$A = -1607$ $B = 92.12589$ $C = -18.34$ $D = -0.001194$ $E = 0.2671 \times 10^{-5}$ $F = 0$
"	750.4 – 1200.0	$A = -1055$ $B = 139.33422$ $C = -29.182$ $D = 0$ $E = 0$ $F = 0$
Liquid	258.15 – 494.3 **	$A = -1609.20$ $B = 148.81342$ $C = -32.4$ $D = 0.004923$ $E = -0.0491 \times 10^{-5}$ $F = 0$
"	494.3 – 1000	$A = -1608.30$ $B = 151.81342$ $C = -32.4$ $D = 0.004923$ $E = -0.0491 \times 10^{-5}$ $F = 0$
"	1000 – 1500	$A = -843.14$ $B = -75.42691$ $C = 8.160$ $D = -0.005942$ $E = 8.332 \times 10^{-5}$ $F = 0$
"	1150 – 1500	$A = -746.0$ $B = -102.54623$ $C = -36$ $D = 0$ $E = 0$ $F = 0$

Note: B = superheated solid, ** = superheated liquid

Table 3.12 Assumed residual enthalpy of formation and entropy for gaseous species H_2 , ($n=1-5$) at 298 K

Species	$\Delta_f H_{298.15}^\circ$ (kJ mol $^{-1}$)	$S_{298.15}^\circ$ (J K $^{-1}$ mol $^{-1}$)
H_2	207.01 ± 0.12	174.63
H_2	144.14 ± 0.60	242.27
H_2	187.44 ± 0.16	313.80
H_2	147.27 ± 3.77	340.32
H_2	143.60 ± 0.76	415.58
H_2	141.26 ± 0.47	434.74
H_2	140.84 ± 0.40	464.39
H_2	138.62 ± 0.21	512.24

Table 3.13: Gibbs energy relative to $\text{H}_{2\text{O}}$ of gaseous selenium at standard vapor pressure, 10^3 J mol^{-1} .

Species	Temperature Range (K)	Coefficients in $G(\text{H}_{2\text{O}})$ -equation $G(\text{H}_{2\text{O}}) = A + BT + CT^2 + DT^3 + ET^4 + FT \ln T$
Se	298.15 - 600	$A = 210840.14$ $B = -47.5879$ $C = +1.9734$ $D = -0.0000405$ $E = -8.4493 \times 10^{-6}$ $F = -293.36$
Se	600 - 3000	$A = 128461.52$ $B = -17.5403$ $C = +12.23$ $D = -0.0000414$ $E = -0.0236 \times 10^{-6}$ $F = 3993.80$
Se ₂	298.15 - 600	$A = 127002.41$ $B = 120.66426$ $C = -37.06$ $D = -0.02164$ $E = -8.4997 \times 10^{-6}$ $F = 244700$
Se ₂	600 - 3000	$A = 117043.23$ $B = -23.50413$ $C = -34.14$ $D = -0.0021815$ $E = -0.0002 \times 10^{-6}$ $F = -0.021508$
Se ₃	298.15 - 3000	$A_0 = 563479.23$ $B = 75.76236$ $C = -68.008$ $D = -0.00007365$ $E = -0.1104 \times 10^{-6}$ $F = 69360$
Se ₃	298.15 - 3000	$A_1 = 140826.90$ $B = 112.65629$ $C = -42.378$ $D = -0.00002393$ $E = -0.0258 \times 10^{-6}$ $F = 263630$
Se ₄	298.15 - 3000	$A = 110878.75$ $B = 308.1143$ $C = -107.565$ $D = -0.0000818$ $E = -0.0043 \times 10^{-6}$ $F = 264830$
Se ₄	298.15 - 8000	$A_0 = 95712.54$ $B = 453.60804$ $C = -112.716$ $D = -0.0007122$ $E = -8.1732 \times 10^{-6}$ $F = 280910$
Se ₆	298.15 - 3000	$A = 188442.32$ $B = 568.17960$ $C = -157.345$ $D = -0.00000036$ $E = -0.2313 \times 10^{-6}$ $F = 254930$
Se ₆	298.15 - 3000	$A_1 = 108559.14$ $B = 404.35476$ $C = -102.480$ $D = -0.00000036$ $E = -0.2432 \times 10^{-6}$ $F = 592360$

CHAPTER 4 A CRITICAL ASSESSMENT OF THERMODYNAMIC AND PHASE DIAGRAM DATA FOR THE Cu-Fe BINARY SYSTEM

4.1 Introduction

Cu-Fe system is a member of the I-VI group containing compounds with wide variety of properties. Cu_3Fe is a mixed conductor which exhibits both ionic and electronic conduction. It is often present in Cu-Fe-based solder alloys as undesirable secondary phase. In contrast, the CuFeSi phase is a low temperature superconductor. Knowledge of the thermodynamics and phase diagram of the Cu-Fe system is essential for understanding the full Cu-Fe-Fe system and its subsequent use in developing new process. A critical assessment of the Cu-Fe system, however, was lacking in the literature. In this chapter, a critical assessment of the literature phase diagram and thermodynamic data for the Cu-Fe system was performed. The association model was used to model the liquid phase, and a three-sublattice compound energy formalism was used for the Cu_3Fe phase. The remaining six metastable solid phases (Cu_2Fe , CuFe , CuFeSi) were modeled as line compounds. A self-consistent set of phase diagram and thermodynamic data was derived through this assessment.

4.2 Phase Diagram Data

The Cu-Fe liquid phase exhibits two miscibility gaps, one for Cu-rich composition and the other for Fe-rich composition. Four intermediate phases were reported in the literature including Cu_3Fe (Cu₃Fe), Cu_2Fe , CuFe and CuFeSi . The Cu_3Fe (Cu₃Fe) phase is the most stable phase in this system with a broad homogeneity

range extending towards the Sn side to form a defect compound. Ca_{1-x}Sn has two polytypes: $\alpha\text{-Ca}_{1-x}\text{Sn}$ and $\beta\text{-Ca}_{1-x}\text{Sn}$. CaSn has three polytypes: $\alpha\text{-CaSn}$, $\beta\text{-CaSn}$ and $\gamma\text{-CaSn}$. Extensive studies have been carried out for the CaSn phase diagram using DTA (Differential Thermal Analysis), XRD (X-Ray Diffraction), microscopy, and microchemical techniques. Earlier work covered the copper-rich side at high temperatures as reported by [Hsu 34]. Later [Chi 83] critically reviewed the phase diagram and thermodynamic data for the system, but did not perform an optimized assessment subsequent to this review. [Ros 84] and [Abe 84] further studied the Ca_{1-x}Sn phase using DTA and DSC (Differential Scanning Calorimetry) carried out more studies for the Ca_{1-x}Sn phase. [Chi 85] studied the miscibility gap in the Cu-rich side by the acoustic method. All the phase diagram data are shown in Figures 4.2 a and b. The assessed equilibria are listed in Table 4.11.

4.1 Entropy, Enthalpy and Heat Capacity Data

4.1.1 $\alpha\text{-Ca}_{1-x}\text{Sn}$

The standard enthalpy of formation, $\Delta H^\circ_{f,298.15\text{K}}$ value for $\alpha\text{-CaSn}$ was measured by several authors using a variety of techniques as summarized in Table 4.1. Grosse and Schmalzer [Chi 56] reported a value of $\Delta H^\circ_{f,298.15\text{K}} = -19.7$ (kJ/mol), by direct synthesis calorimeter. Several investigators have used solid state galvanic cells to measure the Gibbs energy of formation of CaSn phase at various temperatures. Valverde [Val 68] reported $\Delta G^\circ_{f,1000\text{K}} = -45.8$ (kJ/mol) using the following cell,



The standard enthalpy of formation, $\Delta H_{f,298.15}^{\circ} = -61.9$ (kJ/mol), was evaluated by Mills [Mil 74] from the available literature data using the third law method. Rao and Subramo [Rao 70] measured the equilibrium liquid vapor pressure in the Car-Coulter two-phase dataset and estimated the enthalpy and entropy values using the heat capacity data reported in Kalschauer's book [Kal 70]. Mills re-evaluated the data using a third law analysis, $\Delta H_{f,298.15}^{\circ} = -65.3$ (kJ/mol), and the more accurate heat capacity and phase transition data reported by Kalschauer and Nistang [Kal 70]. Astumian et al [Ast 76] reported a value, $\Delta H_{f,298.15}^{\circ} = -61.5$ (kJ/mol) and $\Delta G_{f,298.15}^{\circ} = 28.5$ (kJ/mol), from their EMF measurements. The value derived from March and Hayling's liquid isothermal calorimetric measurements is substantially lower than other reported values. Part of this discrepancy is likely related to the assumption that the dissolved liquid mixture is an ideal solution. The entropy values, $S_{f,298.15}^{\circ}$, were reported by Rao and Subramo [Rao 70] from vapor pressure measurements and Astumian et al [Ast 76] from EMF measurements. Their data together with the third law re-evaluation by Mills [Mil 74] are listed in Table 4.7. The heat capacity measured by Kalschauer and Nistang [Kal 70] is listed in Table 4.8.

Table 4.7 Standard heat of formation of n-*C*-decane at 298.15 K.

Author	Method	$-\Delta H_{f,298.15}^{\circ}$ (kJ/mol)
Takami and Katoishi [Tak 70] ^a	Reaction calorimetry $\text{C}_{10}\text{H}_{22}(\text{g}) + 15\text{O}_2(\text{g}) \rightarrow$ $10\text{CO}_2(\text{g}) + 11\text{H}_2\text{O}(\text{g})$	69.2
Gunter and Subramo [Gun 70]	Calorimetry	55.1
Yokozaki [Yok 66] ^a	EMF	64.9
Rao [Rao 70] ^a	Vapor pressure	63.3
Astumian [Ast 76]	EMF	61.5
March and Hayling [Mar 77] ^{a,b}	Liquid isothermal calorimetry	22.3
Mills [Mil 74]	Evaluation	65.3

^a Calculated in [Mil 74]. ^b introduced in this work.

4.1.2 β - $\text{C}_{10}\text{H}_{16}\text{Se}$

The values of the standard enthalpy of formation for β - $\text{C}_{10}\text{H}_{16}\text{Se}$ as determined by different authors are listed in Table 4.1. Gerson and Schneider [Ref. 50] reported a value, $\Delta H^\circ_{\text{f,org}} = -55.4$ (kJ/mol), by direct systematic calorimetry. Again the values derived from Simack and Heyding's liquid bomb calorimetric measurements are too low. A value of the standard entropy of β - $\text{C}_{10}\text{H}_{16}\text{Se}$ value, S°_{org} , was calculated by [Ref. 70] from vapor pressure measurements. Their data together with [Ref. 70]'s evaluation value are listed in Table 4.2. The heat capacity measured by Kabanetschvili and Hiding [Ref. 71] is listed in Table 4.3, while the values of $\Delta H^\circ_{\text{f,org}}$ (α - β) from various authors are listed in Table 4.4.

Table 4.2. Standard enthalpy of formation of β - $\text{C}_{10}\text{H}_{16}\text{Se}$ (s) at 298.15 K.

Compound	Reference	Method	$\Delta H^\circ_{\text{f,org}}$ (kJ/mol)
$\text{C}_{10}\text{H}_{16}$	[Ref. 49]	Calorimetry	54.4
$\text{C}_{10}\text{H}_{16}\text{Se}$	[Ref. 50]	Calorimetry	55.4
$\text{C}_{10}\text{H}_{16}\text{Se}$	[Ref. 70]	Extrapolation	47.3
$\text{C}_{10}\text{H}_{16}\text{Se}$	[Ref. 70]**	Liquid bomb calorimetry	34.9
$\text{C}_{10}\text{H}_{16}\text{Se}$	[Ref. 70]**		34.7
$\text{C}_{10}\text{H}_{16}\text{Se}$	[Ref. 70]**		35.2
$\text{C}_{10}\text{H}_{16}\text{Se}$	[Ref. 70]**		33.6
$\text{C}_{10}\text{H}_{16}\text{Se}$	[Ref. 74]	Extrapolation	38.4
$\text{C}_{10}\text{H}_{16}\text{Se}$	[Ref. 75]	Extrapolation	34.9

** Calculated in this work.

Table 4.3. Enthalpy of transition for α - $\text{C}_{10}\text{H}_{16}\text{Se}$ to β - $\text{C}_{10}\text{H}_{16}\text{Se}$.

Author	Method	Transition Temperature	$\Delta H^\circ_{\text{f,org}}$ α - β (kJ/mol)
[Ref. 49]	DTA	464 K	26.3
[Ref. 54]	DTA	423 K	7.05
[Ref. 71]	Adiabatic calorimetry	507 K	1.83
[Ref. 71]	DTA	486 K	1.46
[Ref. 69]	DTA	473 K	4.83
[Ref. 14]	DTA	473 K	7.05

4.3.3 Co_2Si

Reported values of the standard enthalpy of formation, $\Delta H_{\text{f,298.15}}^\circ$, of Co_2Si are listed in Table 4-4. Guttent and Schmalzer [Ref 74] reported the value, $\Delta H_{\text{f,298.15}}^\circ \sim 10.5$ (kJ/mol), by direct synthesis calorimetry. Anderson et al. [Ref 75] reported the value, $\Delta H_{\text{f,298.15}}^\circ \sim 14.6$ (kJ/mol), from their EMF measurements. The enthalpy change of the protected reaction: $0.5\text{TiCo}_2\text{Re}_2(\text{s}) \rightarrow \text{Co}_2\text{SiRe}_2(\text{s}) + 0.5\text{CoRe}_2(\text{s})$, was reported by several authors [Ref 76, Ref 77, Ref 78] and the values are listed in Table 4-5. The absolute entropy value, $S_{\text{298.15}}^\circ$, was reported by [Ref 79] from EMF measurements. Their data together with [Ref 74]'s evaluation value are listed in Table 4-7.

Table 4-4. Standard heat of formation of Co_2Si (J at 298.15 K).

Author	Method	$\Delta H_{\text{f,298.15}}^\circ$ (kJ/mol)
[Ref 74]	Isolation calorimetry	10.5
[Ref 75]	Vapor pressure	14.6
[Ref 76] ^a	from reaction: $0.5\text{TiCo}_2\text{Re}_2(\text{s}) \rightarrow$ $\text{Co}_2\text{SiRe}_2(\text{s}) + 0.5\text{CoRe}_2(\text{s})$	124.3
[Ref 77] ^a	from reaction: $0.5\text{TiCo}_2\text{Re}_2(\text{s}) \rightarrow$ $\text{Co}_2\text{SiRe}_2(\text{s}) + 0.5\text{CoRe}_2(\text{s})$	112.1
[Ref 78] ^a	from reaction: $0.5\text{TiCo}_2\text{Re}_2(\text{s}) \rightarrow$ $\text{Co}_2\text{SiRe}_2(\text{s}) + 0.5\text{CoRe}_2(\text{s})$	119.6
[Ref 79]	Evaluation	124.8

^a Calculated by [Ref 74]^a calculated in this work.

4.3.4 CoSi

Reported values of the standard enthalpy of formation, $\Delta H_{\text{f,298.15}}^\circ$, for CoSi are listed in Table 4-5. Value of the absolute entropy, $S_{\text{298.15}}^\circ$, was reported by [Ref 79] from their vapor pressure measurements and by [Ref 76] from their EMF measurements. Their data together with [Ref 74]'s evaluated value are listed in Table 4-7.

Table 4.3 Standard heat of formation of Cu₂S (s) at 298.15 K

Author	Method	$-\Delta H^\circ_{\text{form}}$ (kJ/mol)
[Cox 56]	Solution calorimetry	79.3
[Yeo 68] ^a	EMF	86.9
[Bass 70] ^a	Vapor pressure	82.0
[Ahl 74]	EMF	75.8
[Hoy 84] ^a	From reaction: $1/2\text{Cu}_2\text{S}(s) + \text{Cu}_2\text{O}(s) \rightarrow 2\text{Cu}(s)$	84.8
[Bar 72] ^{a,b}	From reaction: $1/2\text{Cu}_2\text{S}(s) + \text{Cu}_2\text{O}(s) \rightarrow 2\text{Cu}(s)$	82.5
[Mull 74]	Extrapolation	71.8

^aCalculated in [Mull 74] ^bcalculated in this work4.1.3 Cu₂S

Reported values of the $\Delta H^\circ_{\text{form}}$ from various investigators are listed in Table

4-4, while the reported values of $\Delta G^\circ_{\text{form}}$ are listed in Table 4-7

Table 4.4 Standard heat of formation of Cu₂S (s) at 298.15 K.

Author	Method	$-\Delta H^\circ_{\text{form}}$ (kJ/mol)
[Cox 56]	Calorimetry	82.1
[Bass 70] ^a	Vapor pressure	82.1
[Ahl 74]	EMF	75.7
[Hoy 84] ^a	From reaction: $\text{Cu}_2\text{S}(s) + \text{Cu}_2\text{O}(s) \rightarrow 2\text{Cu}(s)$	80.9
[Bar 72] ^{a,b}	From reaction: $\text{Cu}_2\text{S}(s) + \text{Cu}_2\text{O}(s) \rightarrow 2\text{Cu}(s)$	80.1
[Mull 74]	Extrapolation	69.1

^aCalculated in [Mull 74] ^bcalculated in this work

Table 4.3 Standard enthalpy of solid Cu₂-Se compounds at 298.15 K

Compound	Author	Method	$\Delta_f H^\circ$ in kJ (kJ ^o mol ⁻¹)
α -Cu ₂ Se	[Kaw 79]	Vapor pressure	(11.3)
	[Ade 76]	EMF	86.2
	[Mik 82]	Evolution	(21.7)
β -Cu ₂ Se	[Kaw 79]	Vapor pressure	(62.5)
	[Ade 76]	EMF	(64.5)
	[Mik 82]	Evolution	(27.1)
CuSe	[Kaw 79]	Vapor pressure	(13.6)
	[Ade 76]	EMF	(14.1)
	[Mik 82]	Evolution	(79.2)
Cu ₂ Se ₃	[Kaw 79]	Vapor pressure	(136.3)
	[Ade 76]	EMF	(64.6)
	[Mik 82]	Evolution	(107.5)

Table 4.4 Heat capacity data of Cu₂Se

Compound	C_p (J K ⁻¹ mol ⁻¹)	Temperature Range
Cu ₂ Se	$68.0472 + 79.0781 \times 10^{-5} T$	261-351 K
	$39.7130 + 2.0790 \times 10^{-3} T$	125-1050 K

4.4 Gibbs Energy Data

4.4.1 EMF measurements

[Mik 80] investigated the Cu₂-Se phase, using the solid state galvanic cell Pt|Cu₂Se|Cu₂-Se/graphite, in the temperature range 350°C to 450°C. The electromotive force was measured as function of the stoichiometry of the solid-state compound and the temperature. The composition of the solid solution (Cu₂-Se) was varied by covalent substitution. The chemical potential of copper, μ_{Cu} , in Cu₂-Se is given by

$$\mu_{Cu}^{(1)} = \mu_{Cu}^\circ + RT$$

where F is the Faraday constant, E is the open-circuit potential, and μ_{Cu}^0 is the standard potential of pure Cu. The measured values are plotted in Figure 4.4.

4.4.3 Vapor Pressure Measurement

The following gas species were reported to exist in the Cu-Be system, Se_2 , ($\mu=1$), H_2 , Cu , Cu_2 , CuBe_2 , and CuBe , with Se_2 the most prominent one. Rao and Raghavan [Rao 10] studied the Se_2 equilibrium pressures for Cu-Be system at shown in Figure 4.5. The partial pressure data have been converted into partial Gibbs energy data and used in the assessment. Marbute and Jells [Jells 91] determined the solubility of selenium in molten mixtures of copper and selenium by a modified drop-point method at 1370 K. Asakawa and Tazawa [Asa 16] measured the selenium activities in copper-selenium melt at 1200°C by the transpiration method.

4.5 Thermodynamic Models

4.5.1 Pure Elements and Stoichiometric Compound Phases

The Gibbs energy of Cu is from [Jou 16] and that of Be is from [Chi 96]. The three-term equation given below is used to represent the temperature dependence of the Gibbs energies of stoichiometric compound phases,

$$^0G = a + bT + cT \ln T \quad (4.1)$$

Where 0G is the standard Gibbs energy, T is the absolute temperature, and a , b and c are constants whose values need to be determined from experimental data.

4.5.2 Ternary Solid Solutions

A limited solubility of Be in Cu was measured by [Jou 16, Tay 91], while negligible solubility of Cu in Be was proposed by [Chi 81]. In this work, the solubility of Cu in Be

was also considered negligible, whereas the solubility of Be in Cu is modeled. The Gibbs energy (G^{ss}) of the ternary solid solution based on face-centered cubic (fcc) Cu is expressed as

$$G^{\text{ss}} = x_{\text{Cu}}^{\text{ss}} G_{\text{Cu}}^{\text{ss}} + x_{\text{Zn}}^{\text{ss}} G_{\text{Zn}}^{\text{ss}} + x_{\text{Be}}^{\text{ss}} G_{\text{Be}}^{\text{ss}} \quad (4.3)$$

with

$$x_{\text{Cu}}^{\text{ss}} G_{\text{Cu}}^{\text{ss}} = x_{\text{Cu}} G_{\text{Cu}}^{\text{L}} + x_{\text{Zn}} G_{\text{CuZn}}^{\text{L}} \quad (4.4)$$

$$x_{\text{Zn}}^{\text{ss}} G_{\text{Zn}}^{\text{ss}} = RT(x_{\text{Cu}} \ln x_{\text{Cu}} + x_{\text{Zn}} \ln x_{\text{Zn}}) \quad (4.5)$$

G_{Cu}^{L} is the mean Gibbs energy, and expressed by the Redlich-Kister polynomial [Red, 68]

$$G_{\text{Cu}}^{\text{L}} = x_{\text{Cu}} x_{\text{Zn}} \sum_{j=0}^3 L_j^{\text{Cu}} x_{\text{Cu}}^j x_{\text{Zn}}^{3-j} + x_{\text{Be}}^2 \quad (4.6)$$

where L_j is the binary interaction parameter to be optimized in the present work. The temperature dependence of L_j may be expressed as

$$L_{j,\text{Cu}}^{\text{Cu}} = a_j + b_j T \quad (4.7)$$

4.5.3 Liquid Phase

The subregular model developed by [Hou, 82] was used to describe the Gibbs energy of the liquid phase. Cu₃Zn is the most stable compound in this system, which is stable to 1463 K, and congruently melts at that temperature, while the other compounds peritectically decompose below 695 K. It is thus reasonable to select Cu₃Zn as an associate species for the modeling of the liquid phase

$$(\text{Cu}-\text{Cu}_3\text{Zn})_{\text{liq}} \quad (4.8)$$

The Gibbs energy of the phase (per mole of atoms) can also be expressed by equation (8.2) where the should be replaced by $\{i\}$ (equally). The term ${}^{\circ}G_i^s$ is equal to

$${}^{\circ}G_i^s = y_{\text{Fe}} G_{\text{Fe}}^s + y_{\text{Co}} G_{\text{Co}}^s + y_{\text{Ni}} G_{\text{Ni}}^s \quad (8.8)$$

where y_i refers to the site fractions of the species i : $y_{\text{Fe}} + y_{\text{Co}} + y_{\text{Ni}} = 1$. The terms G_i^s represent the Gibbs energies of the pure liquid phase of species i .

The ideal mixing Gibbs energy ${}^{\circ}G_i^{\text{mix}}$ is equal to

$${}^{\circ}G_i^{\text{mix}} = RT(y_{\text{Fe}} \ln y_{\text{Fe}} + y_{\text{Co}} \ln y_{\text{Co}} + y_{\text{Ni}} \ln y_{\text{Ni}}) \quad (8.9)$$

and the excess Gibbs energy ${}^{\circ}G_i^{\text{ex}}$ is, by Redlich-Kister

$${}^{\circ}G_i^{\text{ex}} = y_{\text{Fe}} y_{\text{Co}} y_{\text{Ni}}^2 \{G_{\text{FeCoNi}}^{\text{ex}} + y_{\text{Fe}} y_{\text{Co}} \{G_{\text{FeCo}}^{\text{ex}} + y_{\text{Fe}} y_{\text{Co}} G_{\text{Fe}}^{\text{ex}}\} \\ + y_{\text{Fe}} y_{\text{Ni}} \{G_{\text{FeNi}}^{\text{ex}} + y_{\text{Fe}} G_{\text{Fe}}^{\text{ex}}\} + y_{\text{Co}} y_{\text{Ni}} \{G_{\text{CoNi}}^{\text{ex}} + y_{\text{Co}} G_{\text{Co}}^{\text{ex}}\}\} \quad (8.10)$$

where the four L terms represent the interactions between the ordered species. They can be expressed as the function of temperature

8.1.4 Order of Interdiffusion Coefficient Phases

The high temperature modification of Co_2Fe ($\beta\text{-Co}_2\text{Fe}$) is related to the Fe (FeNi) or $\text{Fe}(\text{CoFe})$ structure [Pol 84, Bar 41, See 71] suggested that $\beta\text{-Co}_2\text{Fe}$ is the FeNi -type structure with the space group $F\bar{4}3m$. In this structure, four Fe atoms occupy the $4(b)$ sites, four Co atoms occupy the $4(c)$ sites, and the other Co atoms are statistically distributed in the interstitial sites (four interstitial (a), four octahedral (b), and sixteen trigonal (c) positions) [Hey 76] and the later investigations [Tou 81, Ch 83, Sak 83, Yau 71] suggested another structure model based on the space group $Fm\bar{3}m$. Each of these investigations agreed that the Fe atoms occupy the $4(b)$ sites and form a fcc sublattice. While [Ch 84] proposed that all Co atoms occupy the trigonal $12(c)$ sites, and

investigations [Tan 41, Sak 48, Yam 53] proposed that Cu atoms lie on two different sites. Based on the structural data the ordered monochromes β -Cu₂Se phase was divided into three sublattices: one is occupied by Se atoms, and the other two occupied by Cu atoms. The structural data suggested the monochromism is due to the formation of vacancies on the Cu sublattice. The occupation of the two Cu-sublattices are different. The Cu atoms can lie more easily on one sublattice with lower energy than the other one. Therefore, vacancies form more easily on the sublattice with higher energy, and thus ensure one of the two Cu sublattices is always fully occupied by Cu atoms. As a result, the β -Cu₂Se phase was described using the sublattice model developed by [Mol 70, Sak 71] with three sublattices after the formula

$$(\text{Cu}_x\text{V}_{1-x})_2(\text{Se}_y\text{V}_{1-y})_2(\text{Cu})_2 \quad (4.11)$$

where V_h represents vacancy. Including the possibility of vacancies on Se sublattice introduces flexibility in the modeling of the Gibbs energy, but does not imply that the Se sublattice contains a high concentration of vacancies. From the assessment results given later, it is found that the vacancy concentration in the Se sublattice is very small, which is in good agreement with the structural observations.

The low-temperature modification of Cu₂Se, α -Cu₂Se, exhibits a complex reflection process and makes it difficult to identify. The structure of α -Cu₂Se has been described as cubic [Nat 36, Sak 74, Yam 53], pseudo-cubic [Mol 67], tetragonal [Sak 43, Sak 72], orthorhombic [Sak 67, Sak 48, Sak 71], monoclinic [Tan 41, Mol 67, Tan 50] and pseudotetragonal [Kao 33]. Each investigator, however, agrees that the Se atoms form a Se sublattice and the Cu atoms distribute over two or more random sites (e.g., interstitial, octahedral and tetrahedral sites). For modeling the homogeneity range, the

ordered intercalationary α -Cu₂Sb phase was also described with three sublattices after formula (4.7). The Gibbs energy of such a phase i (α -Cu₂Sb or β -Cu₂Sb) can also be expressed by equations (4.2) (where \bar{G}_i is replaced by G_i) with

$$\begin{aligned} {}^0G^i = & x_{\text{Cu}}x_{\text{Sb}} {}^0G_{\text{CuSb}}^i + x_{\text{Cu}}x_{\text{S}} {}^0G_{\text{CuS}}^i \\ & + x_{\text{Cu}}x_{\text{Fe}} {}^0G_{\text{CuFe}}^i + x_{\text{Sb}}x_{\text{S}} {}^0G_{\text{SbS}}^i \end{aligned} \quad (4.12)$$

$$\begin{aligned} {}^0G^i = & \text{aB} [y_1 \ln y_1 + y_2 \ln y_2 + y_3 \ln y_3 + \\ & + (y_4 \ln y_4 + y_5 \ln y_5)] \end{aligned} \quad (4.13)$$

$$\begin{aligned} {}^0G^i = & x_{\text{Cu}}x_{\text{Sb}} \left[\frac{1}{2} \left({}^0G_{\text{CuSb}}^i + {}^0G_{\text{CuSb}}^i (y_{\text{Cu}} - y_{\text{Sb}}) \right) + \frac{1}{2} \left({}^0G_{\text{CuS}}^i + {}^0G_{\text{CuS}}^i (y_{\text{Cu}} - y_{\text{S}}) \right) \right] \\ & + x_{\text{Cu}}x_{\text{S}} \left[\frac{1}{2} \left({}^0G_{\text{CuS}}^i + {}^0G_{\text{CuS}}^i (y_{\text{Cu}} - y_{\text{S}}) \right) + \frac{1}{2} \left({}^0G_{\text{CuFe}}^i + {}^0G_{\text{CuFe}}^i (y_{\text{Cu}} - y_{\text{Fe}}) \right) \right] \end{aligned} \quad (4.14)$$

where y_1 and y_2 refer to the two fractions of the component i in the first and second sublattices, respectively. ${}^0G_{\text{CuSb}}^i$ is the standard Gibbs energy of intercalationary α -Cu₂Sb or β -Cu₂Sb, which will be discussed in this work. ${}^0G_{\text{CuS}}^i$ and ${}^0G_{\text{CuFe}}^i$ can be expressed as

$${}^0G_{\text{CuS}}^i = {}^0G_{\text{Cu}}^{\text{ref}} + a_1 + b_1T \quad (4.15)$$

$${}^0G_{\text{CuFe}}^i = {}^0G_{\text{Cu}}^{\text{ref}} + a_2 + b_2T \quad (4.16)$$

where, ${}^0G_{\text{Cu}}^{\text{ref}}$ is the standard Gibbs energy of pure copper in the first phase, and a_1 and b_1 are the optimized parameters. The value of ${}^0G_{\text{CuSb}}^i$ can be expressed by the following relation [Ann 83, Zhu 99]

$${}^0G_{\text{CuSb}}^i = {}^0G_{\text{Cu}}^{\text{ref}} - {}^0G_{\text{Sb}}^{\text{ref}} + {}^0G_{\text{Sb}}^{\text{ref}} - {}^0G_{\text{Sb}}^{\text{ref}} \quad (4.17)$$

To reduce the number of parameters, the following relations are used in the optimization [Ann 83, Zhu 99]

$$\begin{aligned} & {}^1\bar{G}_{\text{Cu}_2\text{Sn}} - {}^1\bar{G}_{\text{Cu}_2\text{Sn}} - {}^1\bar{G}_{\text{Cu}_2\text{Sn}} \\ & {}^1\bar{G}_{\text{Cu}_2\text{Sn}} - {}^1\bar{G}_{\text{Cu}_2\text{Sn}} - {}^1\bar{G}_{\text{Cu}_2\text{Sn}} \end{aligned} \quad (118)$$

$$\begin{aligned} & {}^1\bar{G}_{\text{Cu}_2\text{Sn}} - {}^1\bar{G}_{\text{Cu}_2\text{Sn}} - {}^1\bar{G}_{\text{Cu}_2\text{Sn}} \\ & {}^1\bar{G}_{\text{Cu}_2\text{Sn}} - {}^1\bar{G}_{\text{Cu}_2\text{Sn}} - {}^1\bar{G}_{\text{Cu}_2\text{Sn}} \end{aligned}$$

4.4 Optimization Procedure

A selected set of thermodynamic and phase diagram data (listed in Table 4.1) were used for the optimization of thermodynamic model parameters of all phases in this system. The critical review of [Cha 11] was used as a guide for selecting the experimental phase diagram data. New experimental phase diagram data [Abt 04, Bor 04, Glin 11, Pan 09] were also used in the optimization. The optimization was performed by using the PANDIT module of the Thermo-Calc program package [Jou 02] and split in six steps.

First, the Gibbs energy coefficients of the stoichiometric compounds $\alpha\text{-Cu}_2\text{Sn}$ and $\beta\text{-Cu}_2\text{Sn}$ and the stoichiometric liquid Cu_2Sn were estimated from enthalpy of formation, standard entropy, heat capacity, transition enthalpy, transition temperature, and melting enthalpy and temperature. Then, assuming that $\beta\text{-Cu}_2\text{Sn}$ is a stoichiometric phase and there is no interaction between the pure elements in the liquid phase, a preliminary optimization of the liquid coefficients was performed based on the selection of relevant miscibility gap and two-phase equilibria. Then, fixing the coefficients of the liquid phase, the coefficients of the ordered intermetallic $\beta\text{-Cu}_2\text{Sn}$ phase were roughly optimized based on the measurements of the activities of copper [Mor 99], two-phase equilibria between liquid and $\beta\text{-Cu}_2\text{Sn}$, and the miscibility and solubility equilibria data. Fourth, fixing the coefficients of the liquid and $\beta\text{-Cu}_2\text{Sn}$ phases, the coefficients of the

monoclinic Cu_2Se , $\alpha\text{-Cu}_2\text{Se}$, $\beta\text{-Cu}_2\text{Se}$ ($\gamma\text{-Cu}_2\text{Se}$), and CuSe phases were optimized based on their enthalpies of formation, enthalpies of transition, standard entropies, and equilibrium data that indicated these phases. As no discontinuous change in entropy was detected in the $\beta\text{-Cu}_2\text{Se}$ - $\gamma\text{-Cu}_2\text{Se}$ transformation by DTA method [Mir 73] the transformation may be considered to be continuous i.e., higher order [Chs 83]. In this work, the $\beta\text{-Cu}_2\text{Se}$ and $\gamma\text{-Cu}_2\text{Se}$ phases are assumed and modeled as one phase. Table 4.6 lists the coefficients of solid phases. The coefficients of the $\alpha\text{-Cu}_{1-x}\text{Se}$ and intermetal solid solution $\text{Se}(\text{Cu})$ phases were optimized based on available experimental data. Finally, all parameters of the phases were optimized to fit the experimental data listed in Table 4.7.

4.1 Results and Discussion

The optimized parameters of the stable phases in the Cu-Se system were listed in Table 4.10. The parameters taken from [Des 90] and [Chs 79] were not reproduced in Table 4.10 to conserve space. The phase diagram and thermodynamic properties of the system have been calculated by using the optimized parameters, which were performed with the Poly-3 module of the Thermo-Calc program package.

The calculated phase diagram is shown in Figure 4.1. The dash line, which denotes the $\beta\text{-Cu}_2\text{Se}$ - $\gamma\text{-Cu}_2\text{Se}$ transformation, is not the calculated result. It is based on the XRD measurement of [Mir 73]. Figure 4.1a-c compared the calculated phase diagram and the measured data. The calculated phase diagram agrees well with the data used in the optimization. It does not agree with some of the data which was not used in the optimization, including the Curie-magnetism gap data measured by [Des 74] (Figure

4.7a) and the α -Cu₄₀Sn₆₀-Cu₄₀Sn₆₀ solvus line and related eutectic measured by [Ogo 09, Ogo 12] (Figure 4.1b). These data are consistent with the ones measured recently. Specifically, the Cu-rich miscibility gap data measured by [Zhu 76] are disagreed with those measured by [Aue 76, Cha 91], while the α -Cu₄₀Sn₆₀-Cu₄₀Sn₆₀ equilibrium and related eutectic measured by [Ogo 09, Ogo 12] are consistent with those measured by [Kie 64].

Table 4.11 presents the experimental and calculated temperatures and compositions of the invariant reactions in this system. The calculated values agree well with the data summarized by [Cha, 90]. The calculated critical temperature of the Cu-rich liquid miscibility gap agrees well with the experimental data of [Cha 91], whereas the calculated critical composition has lower Sn concentration than the experimental one [Cha 91]. However, the calculated compositions of the whole Cu-rich miscibility gap agree well with the experimental data of [Cha 91] as shown in Figure 4.2a. In the calculated phase diagram, the temperatures and compositions of the Sn-rich liquid miscibility gap have been predicted, which need to be verified by future experiments.

Figure 4.3 shows the comparison between the calculated and measured chemical potential of selenium in liquid phase. The calculated values agree with the measured ones [Cha 76] when the mole fraction of selenium is larger than 0.500. When the mole fraction of selenium is less than 0.500, the calculated values lie between the measured results of [Aue 76] and [Cha 71]. The calculated and measured chemical potential of copper in the β -Cu₄₀Sn₆₀ phase is shown in Figure 4.4. The calculated curves essentially agree with the experimental data. The calculated curves, however, are not so accurate as the measured ones. Figure 4.5 shows the comparison between the calculated and measured Sn₂ partial

pressure along the liquid and in equilibrium with the compounds in this system. To calculate the Sn partial pressure, an ideal gas-phase containing 17 species is added to the optimized coefficient set. The parameters of the gas species Sn , Sn_2 , Sn_3 , Sn_4 , Sn_5 , Sn_6 , Sn_7 , and Sn_8 are given in chapter 3, whereas the parameters of the gas species Cu , Cu_2 , Cu_3 , Cu_4 , and Cu_6 are taken from [Bau 94]. The calculated Sn partial pressure values agree well with the measured data of [Kau 90] except those in the low pressure $\text{Sn}(\text{Cu})/\text{Cu}_2/\text{Sn}$ region. Attempts to fit will not allow other experimental data to be fitted, including the experimental Sn_2 partial pressures measured by the same authors in [Kau 90].

The calculated vacancy site fractions in the $\beta\text{-Cu}_2\text{Sn}$ phase are shown in Figure 4.6 and 4.7. In the $\beta\text{-Cu}_2\text{Sn}$ single-phase region, the Cu vacancy concentration as the first sublattice, x_{Cu}^{I} , increases with the increase of selenium concentration, whereas the Sn vacancy concentration, x_{Sn}^{I} , decreases with the increase of selenium concentration. The horizontal lines from the axis fraction of selenium at 0.118 to 0.149 at 380 K in Figures 4.6 and 4.7 correspond to the $\alpha\text{-Cu}_2\text{Sn}/\beta\text{-Cu}_2\text{Sn}$ two-phase region. The calculated Cu vacancy site fraction as the first sublattice is between 0.268 to 0.278 in Figure 4.6, whereas the Sn vacancy site fraction is between 2.87×10^{-17} to 2.22×10^{-9} in Figure 4.7. No experimental data are available for comparison to these calculation results. However, the very limited Sn-vacancy and a large Cu-vacancy concentration set as reasonable agreed to the structural research results [Ste 11, Hay 76, Yau 91].

The experimental and calculated standard enthalpies of formation of the intermediate compounds at 298.15 K in the Cu-Sn system are presented in Table 4.12. The corresponding standard entropies are presented in Table 4.13. The reference state for

these properties is the enthalpy of the pure stable element at 298.15 K. The calculated enthalpies of formation in the present work lie between the data measured by [Jin 36] and those evaluated by [Mol 34]. The calculated standard entropies agree well with those evaluated by [Mol 34], except that of Cu_2O , which lies between the value of [Rau 32] and that evaluated by [Mol 34]. Figure 4.3 shows the calculated heat capacity for Cu_2O along with the experimental result [Koh 73]. The calculated values agree well with the measured ones. The calculated enthalpy of formation of the $\alpha\text{-Cu}_2\text{O}$ - $\beta\text{-Cu}_2\text{O}$ transition at 398 K is 4.45 kJ/mole, which is in good agreement with that measured by [Koh 73]. The calculated enthalpy of the $\alpha\text{-Cu}_2\text{O}$ - $\beta\text{-Cu}_2\text{O}$ transition at 238 K is 1.18 kJ/mole, which is in good agreement with that measured by [Hag 64]. As no experimental heat capacity data for CuO are available, these data are optimized from the phase diagram data after assuming no difference between the heat capacities of $\alpha\text{-CuO}$ and $\beta\text{-CuO}$.

4.4 Conclusions

A thermodynamic description of the Cu-O binary system was obtained by optimization of the available phase equilibrium and thermodynamic data. The Redlich-Kister polynomial, association solution model, and substitution model were used to represent the Gibbs energy of the Cu_2O liquid, and both Cu_2O phases, respectively. Other intermediate phases are modeled as line compounds. The phase diagram and thermodynamic properties of the system have been calculated by using the optimized model parameters. There is reasonable agreement between the model-calculated values and selected phase equilibrium and thermodynamic data available in the literature for all

phases. Further experimental work is suggested for determining the shape and critical point of the Bi-rich liquid miscibility gap.

Table 4.7 Selected data used in the optimization

Liquid formation/transition	Reference
β -Cu ₂ Bi liquid, congruent and eutectic (Bi-rich side)	[Hay 44] [Ser 48] [Has 71], [Rob 74] [Joh 75] [Pan 79]
Liquid miscibility gap and miscibility (Cu-rich side)	[Rob 75] [Has 76] [Joh 77]
β -Cu ₂ Bi liquid/Cu-rich mixture	[Ser 48] [Tay 78] [Rob 75] [Chu 81]
α -Cu ₂ Bi/ β -Cu ₂ Bi, peritectic and eutectic	[Hay 44] [Rob 74] [Joh 75] [Joh 84], [Ser 48]
Other phase equilibrium data	[Joh 75] [Chu 81] [Chu 82] [Chu 94]
Chemical potential of Bi	[Pan 79] [Joh 79] [Joh 79]
Chemical potential of Cu	[Joh 89]
Enthalpy of formation	[Chu 84] [Joh 84]
Standard entropy	[Joh 74]
Heat capacity	[Rob 71]
Enthalpy of transition	[Hay 44] [Rob 71]
Enthalpy of fusion	[Rob 74]

Table 4. 10 Operational parameters according to the analytical description of the planes

[illegible]

* Temperature (T) is at 298 K. The Gibbs energies of the liquid, InGaIn , GaInIn , $\alpha\text{-GaIn}$, $\beta\text{-GaIn}$ and GaIn are in J/mol of atoms. The Gibbs energies of $\alpha\text{-Ga}$, $\beta\text{-Ga}$ and Ga are in J/mol of Ga. InGaIn and GaInIn . The residual 2 indicates $\chi^2 = \text{SS}/n$, and n represents the number of data.

Table 4.11 Experimental and calculated temperatures and compositions of the eutectic reactions in the Cu-Sr system

Phase	Composition, at % Sr	Temperature [K]	Reaction Type	Reference
Cu_{12}S	18.6718 ± 15.3715 ±	1389 1389	Critical	[Jin 74] This work
$\text{Cu}_2\text{S}/\beta\text{-Cu}_{12}\text{S}$	33.1331 ± " 1.3333 ± 43.1333 ± 3.0333 ±	1348 1370 1370 1348 1370	Monotectic	[Jin 74] [Jin 75] [Jin 75] [Jin 91] This work
$\text{Cu}_{12}\text{S}/\delta\text{-Cu}_{12}\text{S}$	" 40.0333 ± 71.8333 ± 8.0333 ±	1348 1340 1346 1338	Eutectic	[Jin 74] [Jin 91] [Jin 91] This work
Cu in $\text{Cu}_{12}\text{S}/\beta\text{-Cu}_{12}\text{S}$	0.0333 ± 0.0333 ± 0.0333 ± 0.0333 ± 0.0333 ± 0.0333 ± 0.0333 ± 0.0333 ±	406 395 411 428 396 403 396 396	Peritectic	[Jin 74] [Jin 87] [Jin 73] [Jin 75] [Jin 75] [Jin 89] [Jin 91] This work
$\beta\text{-Cu}_{12}\text{S}/\delta\text{Cu}_{12}\text{S}$	33.1333 ± 33.1333 ± 33.1333 ± 33.1333 ± 33.1333 ± 33.6333 ±	1421 1386 1403 1403 1421 1399	Congruent	[Jin 74] [Jin 87] [Jin 75] [Jin 91] [Jin 91] This work
Cu_2S	48.6666 ±	1376	Critical	This work
$\beta\text{-Cu}_{12}\text{S}/\delta\text{Cu}_2\text{S}$	" 31.6666 ± " " 14.3333 ± 34.4666 ±	796 796 813 796 796 796	Monotectic	[Jin 74] [Jin 75] [Jin 75] [Jin 75] [Jin 91] This work
$\beta\text{-Cu}_{12}\text{S}/\delta\text{Cu}_2\text{S}/\text{CuS}/\delta\text{Cu}_2\text{S}$	44.5000 31.1666 ± 31.1666 ± " 34.5000 35.8333 ±	833 837 837 837 850 850	Peritectic	[Jin 74] [Jin 75] [Jin 75] [Jin 75] [Jin 91] This work
$\gamma\text{-CuS}/\text{CuS}/\delta\text{Cu}_2\text{S}$	50.0000 ± 49.6666 ±	833 838	Peritectic	[Jin 74] [Jin 75]

	MoSe V MoSe V MoSe / MoS ₂	604 605 605		[MoSe V] [Chs 41] This work
CuSe ₂ /Se-Cu ₂	66 7100 " " " 66 7100/100	491 495 491 494 494	Exfoliated (or partially)	[Hay 65] [Mor 72] [Mor 75] [Chs 41] This work
β -Cu ₂ Se/CuSe/ β -CuSe	<100/50 <10 66/66/50 <10 66/66/50 100/50 34 500/50 71/66/50 16 500/50	408 414 408 186 183 417 183	Polycrystalline	[Hay 64] [Mor 72] [Hay 73] [Mor 74] [Chs 41] [Kur 44] This work
α -CuSe/ β -CuSe	66/50 50/50 50/50 50/50 50/50 50/50	716 719-721 722 728 723 726 724	Polycrystalline	[Hay 64] [Mor 72] [Kur 71] [Hay 73] [Mor 74] [Chs 41] This work
α -CuSe- β Se/ β -CuSe/ β -CuSe	34 67/6 100 34 27/6 100 34 47/6 100	710 291 291	Exfoliated	[Hay 72] [Mor 74] This work

Table 4.12 Experimental and calculated standard enthalpies of formation (ΔH_f° (kJ/mol)) of the intermediate compounds at 298.15 K in the Cu–Se system (all phases)

Compound	ΔH_f°	Method	Reference
CuSe ₂	57.3	Calorimetry	[Gut 94]
	60.9	ΔH_f°	[Vol 64]
	62.6	Vapor pressure	[Rau 70]
	63.7	ΔH_f°	[Ash 76]
	63.3	Evaluation	[Mol 74]
	79.1	Assessment	This work
CuSe ₃	98.9	Calorimetry	[Gut 94]
	124.9	ΔH_f°	[Hay 64]
	94.6	ΔH_f°	[Ash 76]
	104.6	Evaluation	[Mol 74]
	104.6	Assessment	This work
CuSe	39.6	Calorimetry	[Gut 94]
	46.0	ΔH_f°	[Vol 64]
	46.6	Vapor pressure	[Rau 70]
	52.6	ΔH_f°	[Ash 76]
	46.8	Evaluation	[Mol 74]
	43.6	Assessment	This work
CuSe ₄	43.1	Calorimetry	[Gut 94]
	46.8	Vapor pressure	[Rau 70]
	38.7	ΔH_f°	[Ash 76]
	43.1	Evaluation	[Mol 74]
	44.1	Assessment	This work

Table 4.13 Experimental and calculated (present) entropies (S_{298}°) of the intermediate Compounds at 298.15 K in the Cu-Be system (J/K.mol)

Compound	S_{298}°	Method	Reference
CuBe	157.4	Vapor pressure	[Kus 70]
	111.9	EMF	[Ash 76]
	129.7	Evaluation	[M4 74]
	127.7	Assessment	This work
Cu ₃ Be	187	EMF	[Ash 76]
	207.2	Evaluation	[M4 74]
	180.7	Assessment	This work
CuBe	66.2	Vapor pressure	[Kus 70]
	74.1	EMF	[Ash 76]
	74.2	Evaluation	[M4 74]
	74.2	Assessment	This work
CuBe ₂	120.6	Vapor pressure	[Kus 70]
	98.4	EMF	[Ash 76]
	107.4	Evaluation	[M4 74]
	104.4	Assessment	This work

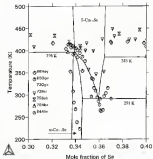


Figure 4.25 Comparison between the calculated Cu-Se phase diagram and various experimental data available in the literature as far as study of $m\text{-Cu}_3\text{Se}$ and $\beta\text{-Cu}_3\text{Se}$ equilibria and the related eutectic

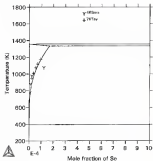


Figure 4.1a: Comparison between the calculated Ca-Fe phase diagram and experimental data available in the literature for the Se solubility in Ca (various)

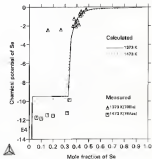


Figure 4.1 Calculated chemical potential of Se in the liquid phase along with the experimental data [164a, 7184a]. The reference state is the (liquid) phase of pure selenium.

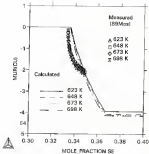


Figure 4-4 Calculated chemical potential of Cu in the B-Cu phase with the experimental data (189 MeV). The reference state is the Cu phase of pure copper.

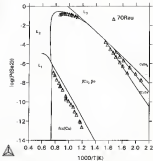


Figure 4.5 Calculated Se_2 partial pressures in the Cu-Se system (mm) along with the experimental data [70Rau]

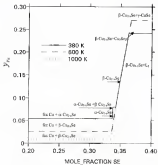


Figure 4-1 The calculated size fraction of Cu vacancy as the function of Se for the $(\beta\text{-Cu}_{13}\text{Se})$ phase

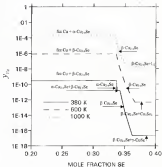


Figure 4.3 The calculated size fractions of Se vacancy on the second sublattice for the β -Cu₂Se phase.

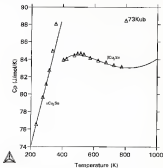


Figure 4.8 Calculated heat capacity for $\alpha\text{-Co}_3\text{S}_4$ and $\beta\text{-Co}_3\text{S}_4$ along with the experimental values [730a].

CHAPTER 5 A CRITICAL ASSESSMENT OF THERMODYNAMIC AND PHASE DIAGRAM DATA FOR THE Cu-Ge SYSTEM

5.1 Introduction

The Ge-Ge system is a member of the III-VI group containing semiconducting compounds (InAs , InSb , In_2S_3 , In_2Se_3) with possible applications in electronic devices. Knowledge of the thermodynamics and phase diagram Ge-Ge system is necessary for the study of the Cu-Ge-Ge system. A critical assessment of the Ge-Ge system is absent in the literature. In this work an assessment of the Ge-Ge system using the phase diagram and thermodynamic data in the literature, the SFTG assay assessment [Zuo 91] for InAs , and the one for selenium given in chapter 3. Nine intermediate solid phases (Cu_2Ge , InGe , In_2Ge , In_3Ge_2 , In_4Ge_3 , In_5Ge_4 , In_6Ge_5 , β - In_2Ge , γ - In_2Ge , and δ - In_2Ge) are treated as pure compounds. The accurate model [Zuo 91] was used to describe the liquid phase. By coupling the thermodynamic and the phase diagram data, optimized G - P - T representations for the solid compounds and the liquid phase are obtained together with the major vapor phase species (Ge_n , $n=1$ to In , In_2 , In_3 , In_4 , In_5 , In_6) in Ge-Ge system. The T - x and P - T projections of the P - T - x diagram were assessed.

5.2 Phase Diagram Data

The phase diagram of In-Sn system was studied by [¹Shi 43, ²Shi 43, ³Shi 43, Qiu 44, Liu 74, Liu 44, Qiu 44, Dai 56, Zuo 56 and Qiu 56]. The early studies by [¹Shi 43, ²Shi 43, ³Shi 43 and Qiu 44] were performed by DTA and X-ray analysis. Four intermetallic compounds, $\text{In}_2\text{Sn}(s)$, $\text{InSn}(s)$, $\text{In}_3\text{Sn}_4(s)$ and $\text{In}_5\text{Sn}_6(s)$ were reported. $\text{InSn}(s)$ and $\text{InSn}_2(s)$ were identified as congruent melting species. One miscibility gap was proposed in their diagram. Licherman and Gassner [*Lik 74*] investigated the In-Sn system from 12 to 48 at % Sn using DTA and X-ray analysis. They reported five compounds $\text{InSn}(s)$ (instead of InSn_2), $\text{InSn}(s)$, $\text{InSn}(s)$ (instead of In_3Sn_4), $\text{InSn}(s)$ and $\text{In}_5\text{Sn}_6(s)$. Only $\text{InSn}(s)$ was identified as a congruent melting species and two miscibility gaps were proposed in their diagram. Liu *et al.* [*Liu 81*] investigated the phase diagram from 16 to 56 at % by DTA. They also carried out the compositional analysis of the compounds grown from the stoichiometric and non-stoichiometric melts using the Rutherford backscattering technique (RBS). Their diagram was in qualitative agreement with the diagram reported by Licherman *et al.* [*Lik 74*]. The main differences are the compositions of the peritectic reactions and the shape of the liquidus lines.

Qian *et al.* [*Qiu 87*] measured the diffusional propagation rate at different compositions and temperatures of liquid In-Sn alloys to study the L-rich miscibility gap. Qian and Qian [*Qiu 93*] investigated the electronic properties of liquid In-Sn alloys including electrical resistivity, thermopower and magnetic susceptibility. They also determined the melting temperatures of In-Sn alloys at different compositions from the temperature dependence of the electronic properties. The In-Sn phase diagram was revised by Qian *et al.* [*Qiu 96*] based on the work of [^{1,2,3}Shi 43, *Lik 74* and *Liu 81*].

Dubicki [Ref 90] measured the electroconductivity for liquid intermetallic $\text{In}_{1-x}\text{Sn}_x$ alloys and determined the semiconducting gap on the basis of the phase diagram. Dasgupta *et al.* [Das 94] investigated the In-Sn phase diagram using DTA, DSC, and XRD. Their diagram is in qualitative agreement with [Das 94]. Górecki *et al.* [Gor 98] re-investigated the stable and metastable In-Sn phase diagram using DTA, XRD, optical microscopy, SEM, and TEM. They reported In_2Sn_3 and In_3Sn_2 are stable phases at stoichiometric composition and $\beta\text{-In}_2\text{Sn}_3$ was observed at 91.4 at. % contrary to previous studies, which suggested $\beta\text{-In}_2\text{Sn}_3$ was one of the polymorphic stoichiometric In_2Sn_3 phases. They also suggested $\alpha\text{-In}_2\text{Sn}_3$ phase is slightly Sn-rich compared to stoichiometric $\gamma\text{-In}_2\text{Sn}_3$ phase. However, the exact composition was not reported. The formation of In_2Sn_3 and In_3Sn_2 was suppressed while applying cooling rate between 2 to 10 K/min. They analyzed the difference between their findings and the literature data by the different experimental procedures. The phase diagram data from various authors are shown in Figure 5.2. The current equilibria are listed in Table 5.1.

Table 5.1 Invariant equilibria in the In-Sn binary system

Phase	Composition (at. % Sn)	Temperature (°C)	Reaction Type	Reference
$\text{L}/\text{In}_2\text{Sn}_3$	50/50	-429.15	Eutectic	[Das 94]
$\text{L}_2/\text{In}_2\text{Sn}_3$	-50/50	-429.15	Eutectic	[Loh 94]
	60/40	-429.15		[Das 94]
	60/40	-429		[Das 98]
	60/40	-429.15		[Gor 98]
	1.41x10 ⁻² /98.59	-429.7		This study
$\text{L}_1/\text{L}_2/\text{In}_2\text{Sn}_3$	4/96/4	793.15	Monotectic	[Gor 98]
	-5/95/5	793.15		[Loh 94]
	-10/90/10	793.15		[Das 94]
	4/96/4	793.15		[Das 98]
	3/97/3	793.15		[Das 98]
	0/100/0	793.7		[Das 94]

	4026/42.9	764		(Dist 94)
		766-15		(Good 98)
	4026/42.9	765-15		(Med 95)
				This study
$L_2/\text{In}(\text{In}_2/\text{In}_2\text{In}_2)$	30231.25/15.15	825-15	Positive	(2 Ma 91)
$L_2/\text{In}(\text{In}_2/\text{In}_2\text{In}_2)$	50234/42.9	826-15	Positive	(Lab 79)
	50238-42.9	823-15		(Time 81)
	50235-42.9	828-15		(Oke 96)
	50234/42.9	826-15		(Dist 98)
	500-42.9	823-15		(Good 94)
		823		(Med 95)
		828-1		This study
$L_2/\text{In}(\text{In}_2/\text{In}_2\text{In}_2)$	45236/42.9	875-15	Positive	(Lab 79)
	48.5/5023.9	875-15		(Time 81)
	45236/42.9	875-15		(Oke 96)
	44236/42.9	883		(Dist 98)
	/50235.9	884-15		(Good 98)
	/50235.9	875		(Med 95)
	45.5/5023.9	883-9		This study
$L_2/\text{In}(\text{In}_2/\text{In}_2\text{In}_2)$	81253.8/40	933-15	Positive	(2 Ma 92)
$L_2/\text{In}_2/\text{In}_2/\text{In}_2/\text{In}_2$	11.3/85.8/53.11	934-15	Positive	(Lab 79)
$L_2/\text{In}(\text{In}_2/\text{In}_2\text{In}_2)$	50252.8/40	938-15	Positive	(Time 81)
	53252.8/40	948-15		(Oke 96)
	53252.8/40	958-15		(Time 81)
$L_2/\text{In}(\text{In}_2/\text{In}_2\text{In}_2)$	81253.8/40	923-15	Positive	(Good 98)
	32.401/50.8/54	922-1		This study
$L_2/\text{In}(\text{In}_2/\text{In}_2\text{In}_2)$	/50258.35	933-15	Positive	(Good 98)
		938		(Med 95)
	32.85/50258.35	934-5		This study
$L_2/\text{In}(\text{In}_2/\text{In}_2\text{In}_2)$	58.33/58.8	943-15	Positive	(Good 98)
		938		(Med 95)
	58.33/58.33/58.8	960-8		This study
$L_2/\text{In}(\text{In}_2/\text{In}_2\text{In}_2)$	/58.33/58	1032-15	Positive	(Good 98)
	57.3/58.33/58	1045-5		This study
$(L_2/\text{In}_2/\text{In}_2/\text{In}_2/\text{In}_2)/L_2/\text{In}_2/\text{In}_2$	/58.33/58	971-15	Estimated	(Good 98)
	58.33/58.33/58	969-5		This study
$L_2/\text{In}_2/\text{In}_2$	60	1072-15	Congruent Mixing	(2 Ma 92)
		1082-15		(Prep 71)
		1081-15		(Time 73)
		1070-15		(Oke 96)
		1158		(Dist 98)
		1084-15		(Good 98)
		1157		This study
	60	1043-15		(2 Ma 92)
	60.33/60	953-15		(Lab 79)

$3\text{-Al}_2\text{SiO}_5\text{-Ca}_2\text{SiO}_7$	4094/10 4094/10 407 ± 2 407 ± 2 4094.82/10.40	1088.13 1087.7 1020.13 1021 1020.3	Monoclinic	[Ohts 96] [Ohts 96] [Ohts 96] [Ohts 96] This study
$3\text{-Al}_2\text{SiO}_5\text{-Ca}_2\text{SiO}_7\text{-SiO}_2$	4094/10 4094/10 4094/10.404	1020.13 1018.13 1013.8	Perovskite	[Shi 92] [Ohts 96] This study
$\text{La}_2\text{SiO}_5\text{SiO}_4$	4094/100 4094/100 4094/100 4094/100 4094/100 4094/100	448.15 448.15 448.15 448 444.15 444	Garnet	[Shi 92] [Liu 94] [Ohts 96] [Ohts 96] [Ohts 96] This study
$\alpha\text{-La}_2\text{SiO}_5\text{-}\gamma\text{-La}_2\text{SiO}_5\text{SiO}_4$	4094/100/100 4094/100/100	484 487.7	Perovskite	[Ohts 96] This study

3.3 Enthalpy, Entropy, and Heat capacity data

3.3.1 Enthalpy data

Enthalpy data of condensed phase oxides was taken from the NIST database [Ohts 96]. The thermodynamic properties of pure elements were assumed in this work as discussed in chapter 3. The data are given in Tables 3.4 and 3.5 in the form of (G°/H_{298}) expressions.

Table 3.4 Enthalpy values in H_{298} of condensed oxides

Phase	Temperature Range (K)	G°/H_{298} or G°/H_{298} expression $G^\circ/H_{298} = A + BT + CT^2 + DT^{-1} + ET^{-2} + FT^3$ (J/mol)
Solid Bridgman	298.15–1291.15 423.15–1388.15	$A = -49162.1$, $B = 10.1766T$, $C = -0.00044$, $D = 3.7054 \times 10^{-5}$, $E = 2.1469 \times 10^{-7}$, $F = -0.0004$, $G = 0$ $A = -49162.1$, $B = 10.1766T$, $C = -0.00044$, $D = 3.7054 \times 10^{-5}$, $E = 2.1469 \times 10^{-7}$, $F = -0.0004$, $G = 1.55 \times 10^{-9}$
Liquid	298.15–1291.15 —	$A = -38610.0$, $B = 14.0410$, $C = -0.00010$, $D = -0.0001$, $E = 1.5237 \times 10^{-7}$, $F = -0.0001$, $G = -0.0001$, $H = 1.5237 \times 10^{-7}$, $I = -0.0001$, $J = -0.0001$, $K = 1.5237 \times 10^{-7}$, $L = -0.0001$, $M = -0.0001$, $N = 1.5237 \times 10^{-7}$, $O = -0.0001$, $P = 1.5237 \times 10^{-7}$, $Q = -0.0001$, $R = 1.5237 \times 10^{-7}$, $S = 1.5237 \times 10^{-7}$, $T = 1.5237 \times 10^{-7}$, $U = 1.5237 \times 10^{-7}$, $V = 1.5237 \times 10^{-7}$, $W = 1.5237 \times 10^{-7}$, $X = 1.5237 \times 10^{-7}$, $Y = 1.5237 \times 10^{-7}$, $Z = 1.5237 \times 10^{-7}$

Note: ¹⁹—superheated solid, ²⁰—superheated liquid.

Table 3.3 Gibbs energy relative to H_{ref} of polyimide isomers

Phase	Temperature Range (K)	Equation in G/H_{ref} expression $G/H_{\text{ref}} = A + BT + CT^2 + DT^3 + ET^4 + FT^5$ (in K units)
Solid Benzophen	240.00–250.00	$A = -1077.0$ $B = -0.12668$ $C = 19.04$ $D = -0.002795$ $E = 0.000000$ $F = 0$
	250.00–260.00	$A = -1077.0$ $B = -0.12668$ $C = 19.04$ $D = -0.002795$ $E = 0.000000$ $F = 0$
.	260.00–270.00	$A = -1080.11$ $B = -0.013441$ $C = 18.981$ $D = 0$ $E = 0$ $F = 0$
	270.00–281.00	$A = -1080.34$ $B = -0.000000$ $C = 19.4$ $D = 0.004907$ $E = 0.000000$ $F = 0$
Liquid	281.00–301.00	$A = -1080.34$ $B = -0.000000$ $C = 19.4$ $D = 0.004907$ $E = 0.000000$ $F = 0$
	301.00–320.00	$A = -1080.34$ $B = -0.000000$ $C = 19.4$ $D = 0.004907$ $E = 0.000000$ $F = 0$
.	320.00–330.00	$A = -1075.14$ $B = -0.013441$ $C = 18.981$ $D = 0.004907$ $E = 0.000000$ $F = 0$
	330.00–350.00	$A = -1060.11$ $B = -0.013441$ $C = 18.981$ $D = 0$ $E = 0$ $F = 0$

Note: ^o experimental value, ^{est} extrapolated liquid

3.3.2 **Benzophen**

$\text{In}_2\text{In}_2\text{O}_6$ was reported to exist in several polymorphic phases, however, the literature contains contradictory results on the structure and phase transition temperature [Shi 66, Ishai 68, Lee 74, Loh 76, Pop 77, Pop 78, Loh 80, Miao 80, Oka 80, Oka 88, and God 89]. The uncertainty about the structure of $\text{In}_2\text{In}_2\text{O}_6$ is likely related to several reasons including: 1. Complexity and similarity of the different polymorphic structures that exist in the vicinity of the composition; 2. Different techniques used to prepare the samples; 3. The volatile nature of $\text{In}_2\text{In}_2\text{O}_6$ caused the composition to drift during the heat treatment involved in phase transition experiments; 4. The difficulty in performing in situ structural investigations without losing volatile components from the vapor phase.

Mills [Ishai 76] reported the only information concerning the high-temperature heat capacity and enthalpy of transition. He reported the heat capacity for $\text{In}_2\text{In}_2\text{O}_6$ and

$\ln_2\text{Sn}_3$, β) in the temperature range $T=200$ to 350 K and the transition enthalpy at 455 K. The XRD analysis on the specimen is $\ln_2\text{Sn}_3$, β sample after the DSC measurements indicate that $\ln_2\text{Sn}_3$, β is β - $\ln_2\text{Sn}_3$. This result is consistent with [Ged 96] α phase diagram. DSC's C_p data were used to fit the heat capacity, $C_p(T)$, equations for α , β and γ - $\ln_2\text{Sn}_3$. The β - $\ln_2\text{Sn}_3$ heat capacity was estimated by [Pan 88] from $\ln_2\text{Sn}_3$ heat capacity data. The fitted $C_p(T)$ results were given in Table 5.1.

The standard enthalpy of formation, $\Delta H^\circ_{\text{form},298}$, for α - $\ln_2\text{Sn}_3$ has been studied by several authors using different techniques: including combustion calorimetry [Hos 53], solution calorimetry [Ste 47], mass spectrometry [Bar 69], vapor pressure (sublimation spectra) [Cox 75], EMF measurements [Mue 54], [Mal 60], vapor pressure measurements (Knudsen or astatic) [Pan 78, Pan 88, Bar 88] and analysis of the reaction: $\ln_2\text{Sn}_3(\text{g}) + \ln_2\text{Sn}_3(\text{g}) \rightarrow 1 \text{ Sn}_2(\text{g}) + 1 \text{ Sn}_2(\text{g}) + 1 \text{ Sn}_2(\text{g})$ [Cox 75].

Malik [Mal 76] reported the value for α - $\ln_2\text{Sn}_3$ is β - $\ln_2\text{Sn}_3$ transition enthalpy, $\Delta H^\circ_{\text{tr}} = 45$ kJ/mol, using DSC. His value was reinterpreted as α - $\ln_2\text{Sn}_3$ to γ - $\ln_2\text{Sn}_3$ transition based on the recent phase diagram [Ged 96]. The standard enthalpy of formation, $\Delta H^\circ_{\text{form},298} = -319.9$ kJ/mol for γ - $\ln_2\text{Sn}_3$ was estimated from the standard enthalpy of formation, $\Delta H^\circ_{\text{form},298} = -228$ kJ/mol [Ste 47] for α - $\ln_2\text{Sn}_3$ using the transition enthalpy.

The vapor pressure measurements by [Cox 75, Cox 75, Cox 78, Pan 88, Bar 88] were performed in high temperature range, where β - $\ln_2\text{Sn}_3$ and γ - $\ln_2\text{Sn}_3$ are the stable phases. The vapor pressure data reported by [Pan 78, Pan 88, Bar 88] were used to derive the standard enthalpy of formation value for β - $\ln_2\text{Sn}_3$. The results are summarized in Table 5.4.

Arizono and Sakurai [Re 57] studied the vaporization chemistry by the simultaneous Langmuir and isotherm method in the vicinity of stoichiometric In_2Se_3 . If we re-interpret their data based on the new diagram by [Ref 58] The data they interpreted as the $\alpha\text{-In}_2\text{Se}_3/\text{In}_2\text{Se}_3$ two-phase equilibrium vapor pressure could be re-interpreted as the β/β preparation above the $\gamma\text{-In}_2\text{Se}_3$ and $\beta\text{-In}_2\text{Se}_3$ two-phase domain. Their vapor pressure data were used to estimate the value for $\beta\text{-In}_2\text{Se}_3$ according to the following vaporization reaction,



The value, $\Delta H^\circ_{298.15\text{K}} = 704.4\text{ kJ/mol}$, was obtained by second law method.

The value of entropy, $S^\circ_{298.15\text{K}}$, for $\alpha\text{-In}_2\text{Se}_3(\text{s})$ was reported by [Dow 75, Apr 75, Eqs 14] from measurements of the low temperature heat capacity and by [Mor 74] from DSC measurements. The data are summarized in Table 5.3. The entropy, S°_{298} , for $\gamma\text{-In}_2\text{Se}_3(\text{s})$ was estimated from $S^\circ_{298.15\text{K}}$ of $\alpha\text{-In}_2\text{Se}_3(\text{s})$ using the heat capacity data of $\alpha\text{-In}_2\text{Se}_3(\text{s})$ and $\gamma\text{-In}_2\text{Se}_3(\text{s})$ and ΔS°_{298} transition entropy data obtained in this work. The value, $S^\circ_{298.15\text{K}} = 110.68\text{ JK/mol}$, was obtained for $\gamma\text{-In}_2\text{Se}_3(\text{s})$.

The transition enthalpy for $\gamma\text{-In}_2\text{Se}_3$ to $\beta\text{-In}_2\text{Se}_3$ reaction was estimated from the values of standard entropy of formation and the heat capacity of $\gamma\text{-In}_2\text{Se}_3$ and $\beta\text{-In}_2\text{Se}_3$. The transition entropy was then calculated from the equation $\Delta S^\circ = \Delta H^\circ/T_0$. The value $S^\circ_{298.15\text{K}} = 268.99$ was obtained for $\beta\text{-In}_2\text{Se}_3(\text{s})$ from the S°_{298} value of $\gamma\text{-In}_2\text{Se}_3(\text{s})$ and the ΔS°_{298} transition entropy data obtained in this work.

3.3.1 In_2Sn

No thermochemical data are available for the In_2Sn phase. For some α -quaternary systems, the slope of the $\Delta H_{\text{f,298.15}}^\circ$ vs. ρ_{Mg}° composition usually lies outside the base triangle, and the nearest is often the compound with the highest melting point [Kab 76]. Following this trend, the standard heat of formation, $\Delta H_{\text{f,298.15}}^\circ$, for In_2Sn is estimated to be -784.4 kJ/mole from Figure 5.1. The value of standard entropy, $S_{\text{f,298.15}}^\circ$, is estimated to be 109.9 J/K mol by Latimer's rule [Lat 71]. The heat capacity is estimated by Ueda's rule [Kab 77]. The enthalpy, entropy and heat capacity data are listed in Tables 3.2, 3.10 and 3.11, respectively.

3.3.2 In_2Sn_3

As with In_2Sn , there are no thermochemical data available for In_2Sn_3 phase. The standard heat of formation, $\Delta H_{\text{f,298.15}}^\circ$, for In_2Sn_3 is estimated to be -1287 kJ/mole using Figure 5.1. The standard entropy, $S_{\text{f,298.15}}^\circ$, is estimated to be 796.1 J/K mol by Latimer's rule [Lat 71]. The heat capacity is estimated by Ueda's rule [Kab 77]. The enthalpy, entropy and heat capacity data are listed in Tables 3.2, 3.10 and 3.11, respectively.

Table S 4: Standard heat of formation of $\ln_2\text{Sn}_2(\text{s})$ at 298.15 K

Author	Method	$- \Delta_f H^\circ_{298.15} \text{ (kJ/mol)}$
$\ln_2\text{Sn}_2(\text{s})$		
[Sak 42]	Combustion calorimetry	144(1)
[Sak 47]	Symbolic calorimetry	111(1)
[Sak 70]	EMF	129.1(14.4)
[Lin 72]	from reaction $\ln_2\text{Sn}_2(\text{s}) + 2\text{H}_2 = 2\text{HIn}(\text{g}) + 2\text{H}_2(\text{g})$	289
[Yeo 75]	Vapor pressure (Knudsen)	110(5)
[Mih 76]	Extrapolated	126(25)
[Bar 84]	Vapor pressure (Quinn-Knudsen)	144(5)
[Fur 88]	Vapor pressure (Knudsen)	100.2(18)
[Chy 94]	Assumed	129.4(12)
[Sak 95]	EMF	126.4(1.5)
This work	Assumed	121.98
$\gamma\text{-}\ln_2\text{Sn}_2(\text{s})$		
This work*	Calculated from [Sak 47]	111(1)
This work	Assumed	124.5
$\beta\text{-}\ln_2\text{Sn}_2(\text{s})$		
[Sak 37]*	Vapor pressure (Quinn-Knudsen)	114.1
This work	Assumed	120.5
$\beta_2\text{-}\ln_2\text{Sn}_2(\text{s})$		
[Yeo 75]*	Vapor pressure (Knudsen)	121.3
[Fur 88]*	Vapor pressure (Knudsen)	101.0
[Sak 88]*	Vapor pressure (Quinn-Knudsen)	104.7
This work	Assumed	121.4

Note: * available in this work

Table 3.7 Reported $H_{\text{max}}^{\text{H}}$ values for In_2Se_3

Species	$H_{\text{max}}^{\text{H}}$, J (K/mol)	Experimental protocol	Reference
$\alpha\text{-In}_2\text{Se}_3$	187.6	Adiabatic Calorimetry	[Dow 73]
	182.3 ± 3.3	DSC	[Dow 76]
	203.2	Adiabatic Calorimetry	[Cot 79]
	192	Estimated	[Mol 74]
	204.3	Assumed	This work
$\gamma\text{-In}_2\text{Se}_3$	218.7	Estimated	This work
	218.9	Assumed	This work
$\delta\text{-In}_2\text{Se}_3$	261.5	Estimated	This work
	278	Assumed	This work
$\beta\text{-In}_2\text{Se}_3$	238.4	Estimated	[N 47]
	251.3	Assumed	This work

Note: * calculation in this work

Table 3.8 Assumed heat capacity for $\text{In}_2\text{Se}_3(\text{s})$

phase	$C_p^{\text{H}}(\text{s})$, J (K ² /mol)
α	$107.64627 + 0.0007534 \cdot T$
β	$114.76138 + 0.000741 \cdot T$
γ	$111.43643 + 0.0015867 \cdot T$
δ	(?)

3.3.1 $\text{In}_2\text{Se}_3(\text{s})$

The standard enthalpy of formation, $\Delta H_{\text{f,298.15 K}}^{\text{H}}$, and entropy, $S_{\text{298.15 K}}^{\text{H}}$, for $\text{In}_2\text{Se}_3(\text{s})$ have been measured by Madsen *et al.* [Mad 74], but the values were assigned to $\gamma\text{-In}_2\text{Se}_3$. Chatterjee [Cha 70] has recalculated the $\Delta G_{\text{f}}^{\text{H}}(\text{T}) = -764376 + 290.846 \cdot T$ (J/mol). The value $\Delta H_{\text{f,298.15 K}}^{\text{H}} = -631.45$ (J/mol) is obtained by modification of [Mad 74] ± 0.60 J/mol. The value, $S_{\text{298.15 K}}^{\text{H}} = 51.414$ (J/mol) is obtained from the second law $\Delta S_{\text{f,298.15 K}}^{\text{H}}$ value from [Mad 74]. The value, 320.85 (J/mol) is obtained if assumed by Latimer's rule [Lat 70]. The heat capacity was determined by Mills [Mil 74] from DSC

measurement. The enthalpy, entropy and heat capacity data are listed in Tables 5.9, 5.10 and 5.11, respectively.

5.1.3 (sulfur)

The standard enthalpy of formation, $\Delta H_{f,298.15}^\circ$, was determined by Hahn and Bureau [Hah 31] using combustion calorimetry, and by Manohar et al. [Man 74] from their EMF measurements. Values of the enthalpy and entropy of fusion were reported by Mills [Mil 76] using BSC. A value for the absolute entropy, $S_{298.15}^\circ$, data were reported by Manohar et al. [Man 67] from low temperature heat capacity measurements. The value $S_{298.15}^\circ = 77.44$ (J/K mol) is obtained from the [Man 74]'s second law $\Delta S_{f,298.15}^\circ$ value of EMF measurement. Mills [Mil 76] measured the heat capacity using BSC. The enthalpy, entropy and heat capacity data are listed in Tables 5.9, 5.10 and 5.11, respectively.

5.1.3 (sulfuric)

The standard enthalpy of formation, $\Delta H_{f,298.15}^\circ$, and entropy, $\Delta S_{f,298.15}^\circ$, for (sulfuric) have been measured by Manohar et al. [Man 74], which should be assigned to (sulfuric) based on the correct phase diagram. The values $\Delta H_{f,298.15}^\circ = -33.18$ (kJ/mol) and $S_{298.15}^\circ = 70.40$ (J/K mol) were obtained by recalculation of [Man 74]'s EMF data. Chaffee [Cha 50] estimated the energy value to be 281.9 (J/K mol) using Latimer's rule [Lat 25] and the heat capacity data by Ubbelohde's rule [Ubb 37]. The enthalpy, entropy and heat capacity data were listed in Table 5.9, 5.10 and 5.11, respectively.

Table S 8 Standard enthalpy of formation values at 298.15 K, $\Delta H_{\text{f,298.15 K}}^\circ$, of In-Sn compounds

Species	$\Delta H_{\text{f,298.15 K}}^\circ$ (kJ/mol)	Experiment/method	Reference
In(Sn)	741	Estimated	This work
	710.35	Assumed	This work
In ₂ (Sn) ₂	1212.9	Estimated	This work
	1127.6	Assumed	This work
In ₂ (Sn)	289.15 ± 12.2	EMF	[Mar 74]
In ₂ (Sn)	483.87	EMF	[Joh 74] ^a
	856.6 ± 8.7	EMF	[Mar 76]
	333.87	Assumed	This work
In ₂ (Sn)	117.8 ± 12.3	Combustion Calorimetry	[Pan 52]
	128.1 ± 7.9	EMF	[Mar 74]
	118.6 ± 12.6	Estimated	[Sol 74]
	58	Estimated	[Ch 73]
	102.15 ± 6.8	EMF	[Mar 76]
	174.39	Assumed	This work
In-Sn	112.1 ± 11.7	EMF	[Mar 74]
In ₂ (Sn)	112.34	EMF	[Joh 74] ^a
	100.7	Estimated	[Ch 73]
	102.51	Assumed	This work

Note: ^a recalculated in this work, ^{EMF} should be In₂(Sn)

Table 3 (a) Heat capacity values at 298.15 K of In-Se compounds

Species	C_p (J/K mol)	Experimental method	Reference
In_2Se_3	468.8	Estimated	This work
	476.8	Assumed	This work
In_2Se_2	768.8	Estimated	This work
	775.8	Assumed	This work
In_2Se^*	417.8 ± 7.1	EMF	[Mac 74]
In_2Se	714.34	EMF	[Mys 74] ^a
	676.7	EMF	[Mac 80]
	678.8	Assumed	This work
InSe	82.5	Substrate Calorimetry	[Mac 87]
	97.8 ± 2.5	EMF	[Johs 74]
	88.2 ± 1.7	Assumed	[Johs 74]
	81.8	Assumed	[Mac 74]
	75.4	EMF	[Mac 74]
	87.50	Assumed	This work
$\text{In}_2\text{Se}^{**}$	114.4 ± 7.1	EMF	[Johs 74]
In_2Se	146.75	EMF ^a	[Johs 74]
	202.8	Estimated	This work
	165.1	Assumed	This work

Note: * Calculated in this work, ** should be In_2Se_2

Table 3 (b) Heat capacity data for In-Se compounds

Phase	C_p [J/K mol]	Temperature Range [K]	Reference
In_2Se_3	$356.42 + 3.347 \times 10^{-3} T$ $- 3.094 \times 10^{-6} T^2$	298-603	This work ^a
In_2Se_2	$716.72 + 4.1448 \times 10^{-3} T$ $- 3.8 \times 10^{-6} T^2$	298-603	This work ^a
In_2Se	$568.5884 + 6.7612 \times 10^{-3} T$ $- 7.1146 \times 10^{-6} T^2 + 4.4713 \times 10^{-9} T^3$	125-476	[Mac 76]
InSe	$32.52 + 6.26 \times 10^{-3} T$ $- 1.76 \times 10^{-6} T^2 + 6.49 \times 10^{-9} T^3$	125-626	[Mac 76]
In_2Se	$166.837 + 3.437 \times 10^{-3} T$ $- 3.9336 \times 10^{-6} T^2$	294-423	[Chen 81]

Note: ^a Estimated by Dall Jorda [Koh 77]

5.3.4 Gas phase

The thermodynamic data for the gaseous molecules In(g) , In/Sn(g) , In/Sn(g) and InIn(g) were studied by [Cel 66, Gre 71, Gre 75] and summed by [Che 93] including $\Delta H^\circ_{\text{f, gas}}$, $S^\circ_{\text{f, gas}}$ and heat capacity. The $G^\circ_{\text{f, gas}}$ expressions are given in Tables 5.12 and 5.13.

Table 5.12 $G^\circ_{\text{f, gas}}$ of gaseous compounds in In-Sn system

Species	Temperature Range (K)	Coefficients in $G^\circ_{\text{f, gas}}$ expression $G^\circ_{\text{f, gas}} = A + BT + CT^2T = (2T^2 + 3T^3 + 4T) (J/K \cdot \text{mol})$
InIn(g)	298 (1 - 3000)	$A = 98548.31$ $B = 51.27566$ $C = -8.1215$ $D = -0.00000179$ $E = 2.1581 \times 10^{-5}$ $F = 28.801 \text{ K}$
In/Sn(g)	298 (1 - 3000)	$A = 126075.63$ $B = 61.51420$ $C = -10.1900$ $D = -0.00029448$ $E = 2.3201 \times 10^{-5}$ $F = 378.608$
InSn(g)	298 (1 - 3000)	$A = 122581.76$ $B = 4.1146$ $C = -21.100$ $D = -0.00054054$ $E = 3.0002 \times 10^{-5}$ $F = 275.18$

Table 5.13 $G^\circ_{\text{f, gas}}$ of gaseous indium

Species	Temperature Range (K)	Coefficients in $G^\circ_{\text{f, gas}}$ expression $G^\circ_{\text{f, gas}} = A + BT + CT^2T = (2T^2 + 3T^3 + 4T) (J/K \cdot \text{mol})$
In(g)	298 (1 - 400)	$A = 234267.042$ $B = -68.7769731$ $C = -18.34208$ $D = -0.00027533$ $E = -3.9839413 \times 10^{-5}$ $F = -3451.9 \text{ K}$
	400 - 1100	$A = 217666.634$ $B = -130.107013$ $C = -8.403223$ $D = -0.0136147$ $E = 2.25796132 \times 10^{-5}$ $F = -110439.25$
	1100 - 2800	$A = 214080.499$ $B = 178.647770$ $C = -41.36281$ $D = 8.00523417$ $E = -2.534305 \times 10^{-5}$ $F = 283756.7$

5.4 Gibbs Energy Data

5.4.1 EMF measurements

Mitschke *et al.* [Ref. 34] measured the sodium activity in the temperature range 500 to 710 K by electromotive force on the two phase elements $(\text{In}_2\text{Se}_3/\text{In}, (\text{In}_2\text{Se}_3)_2/\text{In}_2\text{Se}_3, \text{InSe-ClInSe}_2, (\text{In}_2\text{Se}_3)_2\text{-InSe})$. In_2Se_3 should be corrected to In_2Se_3 and InSe should be corrected to In_2Se_3 . More recently Mikhlin *et al.* [Ref. 35] measured the sodium activity in solid and liquid (indium + selenium) solutions in 50 mass per cent selenium in the solid-state galvanic cell

5.4.2 Vapor pressure measurements

The following gas species were reported to exist in In-Se system, $(\text{InSe})_2$ to $(\text{InSe})_4$, $(\text{InSe})_2$, $(\text{InSe})_3(\text{g})$, $(\text{InSe})_4(\text{g})$ and $(\text{InSe})_2(\text{g})$. Both total vapor pressure [Lin 32, Yen 33, Lin 34, Lin 35, Lin 36] and partial pressure [Lin 36, Cal 36] measurements in the In-Se system are presented in Table 5.14

Calin and Thewissen [Cal 36] determined the partial pressure in equilibrium with liquid InSe by Knudsen cell mass spectrometry. In their investigation, the condensed phase composition was not constant due to the fact that the unit molar ratio $\text{In}_2\text{Se}_3/(\text{InSe})_2$ varied appreciably with temperature. Grubisic *et al.* [Lin 37] studied the saturated total vapor pressure above liquid InSe by Bourdon quartz gauge and the vapor constituents by electron and IR absorption spectroscopy.

Solubility of $\text{In}_2\text{Sn}_2(\text{s})$ has been studied by mass-spectrometry [Jilek 65], various isothermal effluents [Yim 70, Pao 80, Liu 88, Su 87, Su 85], and molecular microscopy [Lin 73]. $\text{In}_2\text{Sn}_2(\text{s})$ was reported to sublime congruently according to the reaction [Jilek 65, Pao 80, Liu 88]



Congruent behavior has not always been observed and the occurrence depended on the experimental conditions. One reason can reside in the fact that the effluent process may change the condensed phase composition. This effect was shown in Saitama and Edwards' investigations [Su 87, Su 88]. The difference between congruent sublimation and congruent effluents was discussed in [Jilek 80]. In their studies, the condensed phase was not the $\text{In}_2\text{Sn}_2(\text{s})$ one phase system, but a liquid- In_2Sn_2 two-phase boundary. Their data agreed qualitatively with the P-T phase diagram from Grolberg *et al.* [Lin 73], although the pressure measured by [Su 85, Su 87] is much lower. Grolberg *et al.* [Lin 73] studied the vapor phase along the three-phase boundary " $\text{In}_2\text{Sn}_2(\text{s})$ -liquid-vapor " by measuring the total pressure and optical absorption spectra of the vapor. They constructed the P-T projection of the phase diagram along the liquid(s) liquid. The spectroscopic analysis indicated three major components in the measured vapor: $\text{In}_2(\text{In}(\text{g})$, $\text{Sn}(\text{g})$, and $\text{In}(\text{g})$. A small heterogeneity range (~ 0.1 at %) was found in $\text{In}_2\text{Sn}_2(\text{s})$ phase by analyzing the vapor composition along the three phase boundary.

Table 5.14 Equilibrium vapor pressure measurement in the Fe–Sn system

Condensed phase	Experimental method	Reference
Sn(l) (liquid)	Partial pressure (Knudsen cell mass spectrometry)	[Cai 64]
Sn(l) (liquid)	Total pressure (Knudsen cell and IR spectroscopy)	[Gao 74]
Sn ₃ Sn (solid)	Total pressure (Knudsen gauge) and IR spectroscopy	[Gao 70]
Sn ₃ Sn (solid)	Partial pressure (Knudsen cell mass spectrometry)	[Bar 69]
Sn ₃ Sn (solid)	Total pressure (Knudsen cell)	[Finn 77]
Sn ₃ Sn (solid) + liquid Fe–Sn	Total pressure and IR spectroscopy	[Gao 70]
Sn ₃ Sn (solid)	Total pressure (Knudsen cell system)	[Hsu 81]
Sn ₃ Sn (solid) + liquid Fe–Sn	Total pressure (Knudsen cell system)	[Hsu 81, 87]
Sn ₃ Sn (solid)	Total pressure (Knudsen cell)	[Finn 86]

4.5 Thermodynamic Models

4.5.1 Pure elements and stoichiometric compound phases

The Gibbs energy of Cu is taken from [Ste 11] and that of Sn is from [Ste 10].

The three-term equation given below is used to represent the composition dependence of the Gibbs energy of stoichiometric compound phases

$${}^{\circ}G = a + bT + cT \ln T \quad (5.1)$$

Where ${}^{\circ}G$ is the standard Gibbs energy, T is the absolute temperature, and a , b and c are constants whose values need to be determined from experimental data.

4.5.2 Liquid Phase

The association model developed by [Row 82] was used to describe the Gibbs energy of the liquid phase. In Cu₃Sn, is the most stable compound in the system, which is stable at 1145 K and completely melts at that temperature. The conductivity versus composition of liquid Cu₃Sn, shows a deep maximum around the composition of 0.6 Cu mole fraction. It is reasonable then to choose Cu₃Sn as an associate species for the modeling of the liquid phase



The Gibbs energy of the phase (per 1 mole of atoms) can also be expressed by equation (2) where fox should be replaced by i (liquid). The term ${}^{\circ}G^i$ is equal to

$${}^{\circ}G^i = x_{\text{Cu}}{}^{\circ}G_{\text{Cu}}^i + x_{\text{Cu}_3\text{Sn}}{}^{\circ}G_{\text{Cu}_3\text{Sn}}^i + x_{\text{Sn}}{}^{\circ}G_{\text{Sn}}^i \quad (5.2)$$

where p_i refers to the rate fractions of the species i , with $p_{\text{Cu}} + p_{\text{Cu}_3\text{Sn}} + p_{\text{Sn}} = 1$. The terms ${}^{\circ}G_{\text{Cu}}^i$ represent the Gibbs energies of the liquid phases of the species i .

The ideal mixing Gibbs energy ${}^{\text{IG}}G$ is equal to

$${}^{\text{IG}}G = RT(P_{\text{O}_2} \ln P_{\text{O}_2} + P_{\text{Fe}_2\text{O}_3} \ln P_{\text{Fe}_2\text{O}_3} + P_{\text{Fe}} \ln P_{\text{Fe}}) \quad (3.2)$$

The excess Gibbs energy ${}^{\text{E}}G$ is

$$\begin{aligned} {}^{\text{E}}G = & P_{\text{O}_2} P_{\text{Fe}_2\text{O}_3} {}^{\text{E}}G_{\text{O}_2, \text{Fe}_2\text{O}_3} + {}^{\text{E}}G_{\text{Fe}_2\text{O}_3, \text{O}_2} P_{\text{O}_2} + P_{\text{Fe}_2\text{O}_3} {}^{\text{E}}G \\ & + P_{\text{Fe}_2\text{O}_3} P_{\text{Fe}} {}^{\text{E}}G_{\text{Fe}_2\text{O}_3, \text{Fe}} + {}^{\text{E}}G_{\text{Fe}_2\text{O}_3, \text{Fe}} P_{\text{Fe}_2\text{O}_3} + P_{\text{Fe}} {}^{\text{E}}G \end{aligned} \quad (3.4)$$

where the four terms ${}^{\text{E}}G$ represents the interactions between the species. They can be expressed as the function of temperature

3.4 Optimization Procedure

A selected set of thermodynamic and phase diagram data were used for the optimization of thermodynamic model parameters of all phases in this system. The optimization was performed by using the PANDOL module of the Thermo-Calc program package [See 11] and proceeds in four steps

First, initial estimates of the Gibbs energy coefficients of the stoichiometric compounds Fe_2O_3 , FeO , Fe_3O_4 , Fe_2SiO_4 , Fe_2SiO_3 , Fe_2SiO_2 , $\beta\text{-Fe}_2\text{SiO}_3$, $\gamma\text{-Fe}_2\text{SiO}_3$, $\delta\text{-Fe}_2\text{SiO}_3$, and $\alpha\text{-Fe}_2\text{SiO}_3$, were deduced from the reported enthalpy of formation, standard entropy, heat capacity, the enthalpy of melting for Fe_2O_3 was reported in the literature. The Gibbs energy coefficients for liquid Fe_2O_3 were deduced from the melting enthalpy of Fe_2O_3 reported by [16] [76]. Second, a rough optimization of the liquid coefficients was performed based on the activities of selenium, miscibility gap, and three-phase equilibria (three involved the liquid phase). Third, fixing the coefficients of the liquid the coefficients of the stoichiometric Fe_2O_3 , FeO , Fe_3O_4 , Fe_2SiO_4 , Fe_2SiO_3 , Fe_2SiO_2 , $\beta\text{-Fe}_2\text{SiO}_3$, $\gamma\text{-Fe}_2\text{SiO}_3$, $\delta\text{-Fe}_2\text{SiO}_3$, and $\alpha\text{-Fe}_2\text{SiO}_3$ phases were optimized based on the enthalpies of formation,

calculus of variation, standard entropies and phase diagram data. Finally all parameters of the phases were optimized to fit the experimental data.

Table 1.15 Optimized parameters according to the analytical description of the phases

Phase or Function	Parameters
Liquid	$^{\circ}G_{\text{liquid}}^{\text{ref}} = G_{\text{liquid}}^{\text{ref}} - T$ $^{\circ}H_{\text{liquid}}^{\text{ref}} = -66576.4\text{ J}$ $^{\circ}S_{\text{liquid}}^{\text{ref}} = 45241 - 23.712\text{ J/K}$ $^{\circ}C_{\text{liquid}}^{\text{ref}} = 143000 - 145.80794\text{ J/K}^2$ $^{\circ}V_{\text{liquid}}^{\text{ref}} = -28279$
Ice _h	$^{\circ}G_{\text{Ice}_h}^{\text{ref}} = -452540.85\text{ J} + 1835.555\text{ J/K} - 79.5277\text{ J/K}^2 - 8.04235\text{ J/K}^3$ $+ 344486\text{ J/K}^4$
Ice _i	$^{\circ}G_{\text{Ice}_i}^{\text{ref}} = -142649.424\text{ J} + 364.439\text{ J/K} - 43.4276\text{ J/K}^2 + 5.00034\text{ J/K}^3$ $- 1.46 \times 10^{-5}\text{ J/K}^4 + 89480\text{ J/K}^5$
Ice _{II}	$^{\circ}G_{\text{Ice}_II}^{\text{ref}} = -94334.9738\text{ J} - 1791.21\text{ J/K} - 348.59876\text{ J/K}^2 + 6.65531\text{ J/K}^3$ $- 1.64 \times 10^{-5}\text{ J/K}^4 + 559300\text{ J/K}^5$
Ice _{III}	$^{\circ}G_{\text{Ice}_III}^{\text{ref}} = -794675.12\text{ J} + 1365.50725\text{ J/K} - 184.7184\text{ J/K}^2$ $- 9.32179\text{ J/K}^3 + 4.5 \times 10^{-5}\text{ J/K}^4$
Ice _{IV}	$^{\circ}G_{\text{Ice}_IV}^{\text{ref}} = -163481.344\text{ J} + 1540.754\text{ J/K} - 134.1276\text{ J/K}^2 + 5.01190\text{ J/K}^3$ $+ 2.73 \times 10^{-5}\text{ J/K}^4$
β -Ice _{VI}	$^{\circ}G_{\text{Ice}_VI}^{\text{ref}} = -235495.24\text{ J} - 219.8431\text{ J/K} - 108.7339\text{ J/K}^2 - 50.5275\text{ J/K}^3$
γ -Ice _{VI}	$^{\circ}G_{\text{Ice}_VI}^{\text{ref}} = -256417.4285\text{ J} + 2564.5764\text{ J/K} - 113.4183\text{ J/K}^2$ $- 8.87594\text{ J/K}^3$
Ice _V	$^{\circ}G_{\text{Ice}_V}^{\text{ref}} = -241146\text{ J} + 380.2596\text{ J/K} + 13.4148\text{ J/K}^2 - 5.04756\text{ J/K}^3$ $+ 2981.5\text{ J/K}^4 + 944.8$ $= - 236775.5\text{ J} + 812.1460\text{ J/K} - 1.5\text{ J/K}^2$ $+ 6.8\text{ J/K}^3 + 2000$
α' -Ice _{VI}	$^{\circ}G_{\text{Ice}_VI}^{\text{ref}} = -154481.65\text{ J} + 932.8541\text{ J/K} - 187.4440\text{ J/K}^2 - 1.02771\text{ J/K}^3$ $+ 2981.5\text{ J/K}^4 + 944.8$ $= - 154945.65\text{ J} + 961.5077\text{ J/K} - 113.4283\text{ J/K}^2 - 9.20794\text{ J/K}^3$ $+ 74.0531\text{ J/K}^4$ $= - 236775.5\text{ J} + 826.1600\text{ J/K} - 0.1\text{ J/K}^2 -$ $+ 6.8\text{ J/K}^3 + 2000$
Function	$G_{\text{Ice}_VI}^{\text{ref}}(T) = 14898.1541 - 1.0187738\text{ J/K} + 0.02561\text{ J/K}^2$ $+ 0.00065\text{ J/K}^3 - 0.00076\text{ J/K}^4 + 0.0037594\text{ J/K}^5 - 113.4183\text{ J/K}^2 - 9.20794\text{ J/K}^3$ $+ 74.0531\text{ J/K}^4$ $= - 154945.65\text{ J} + 970.5082\text{ J/K} - 124.566\text{ J/K}^2 + 0.0187\text{ J/K}^3 + 2000$

+ Temperature (T) is in Kelvin. The Gibbs energies are in kJ/mol

5.7 Result and Discussion

The optimized parameters of the *ortho* phase in the *iso*-*iso* system are listed in Table 5.3. The phase diagrams and thermodynamic properties of this system were calculated with the *Prop-3* module of the Thermo-Calc program package. The calculated phase diagram is shown in Figure 5.1. Comparisons between the experimental and calculated phase diagrams are shown in Figures 5.2 to 5.6. Table 5.1 presents the experimental and calculated temperatures and compositions of the invariant reactions in the system.

The calculated values are well within the uncertainty of experimental data. The calculated *iso*-rich liquid miscibility gap agrees well with the experimental data of [Gla 81] and [Gou 88] as shown in Figure 5.4. The calculated peritectic reactions and liquidus lines for *iso*/*iso*, *iso*/*iso*, *iso*/*iso*, *iso*/*iso*, *iso*/*iso* and *β*-*iso*/*iso*, are shown in Figure 5.1 in detail along with the experimental data. In general, the calculated diagram is in agreement with the experimental data. The calculated phase diagram in the *Se*-rich side is given in Figure 5.4 in comparison with the experimental data. Figure 5.5 shows the comparison between the calculated and measured activity of selenium. The calculated activity deviated more positively than the experimental data.

Figure 5.7 shows the comparison between the calculated and measured total vapor pressure in the system. To calculate the total pressure, an ideal gas phase containing 15 species is added to the optimized coefficient set. The parameters of the gas species *Se*, *Se₂*, *Se₃*, *Se₄*, *Se₅*, *Se₆*, *Se₇* and *Se₈* are from chapter 3, whereas the parameters of the gas species *is*, *is₂*, *is₃*, and *is₄*/*Se₂* are from [Ren 96]. The calculated total pressure agrees well with the measured data. The calculated total pressure data are in good agreement

with the measurements of [Chi 71]. The calculated T_g data along the β -isopleth, isopleth agree well with the measurements of [Se 47] and [Fox 49].

The experimental and calculated standard enthalpies of formation of the organosulfur compounds at 298.15 K in the h_2S system are presented in Tables 5.4 and 5.5. The corresponding standard entropies are presented in Tables 5.7 and 5.8. The reference states of these data are the enthalpies of the pure stable elements at 298.15 K. The standard enthalpy of formation for α - h_2S_6 in the present work are close to the equilibrium calorimetry value [Ste 67]. This value was obtained by direct synthesis of α - h_2S_6 in a bomb calorimeter. The equilibrium compound was confirmed by X-ray diffraction. This technique does not rely on other thermodynamic functions, which introduces additional uncertainty. The assessed standard enthalpies for β - h_2S_6 and γ - h_2S_6 are close to the values derived from [Ste 67] and [Ste 67] respectively. The assessed enthalpy of formation for h_2S_8 is well within the experimental uncertainty of the value measured by [Ste 62] from combustion calorimetry. It was found that the enthalpy of formation value for h_2S_8 is much more negative than the value derived from DSC measurements of [Ste 74] and closer to the value by [Mal 53]. It was also found that the enthalpy of formation value for h_2S_{10} is much more negative than the value evaluated by [Chi 91] and the recalculated value from [Ste 74]. A more positive value of the enthalpy of formation resulted in the disappearance of h_2S_{10} phase in the calculated $T-x$ phase diagram.

The assessed entropy values are well within the available experimental values. The calculated heat capacity data for α - h_2S_6 , γ - h_2S_6 , β - h_2S_6 , h_2S_8 and h_2S_{10} along with

the measured data by [96, 76] are given in Figure 5.4.5.9 and 5.4.6, respectively. The calculated values agree well with the measured ones.

5.4-Conclusion

A thermodynamic description of the Li-Sn binary system is obtained by optimization of the available phase equilibrium and thermodynamic data. The regular solution model was used to represent the Gibbs energy of the liquid phase. The intermediate phases were modeled as line compounds. The phase diagram and thermodynamic properties of the system have been calculated by using the optimized model parameters. There is reasonable agreement between the model-calculated values and the phase equilibrium and thermodynamic data available in the literature for all phases.

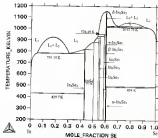


Figure 1.7 Calculated In-Sn phase diagram based on the optimized parameters

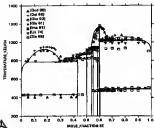


Figure 5-3 Calculated In-In phase diagram along with the experimental data.

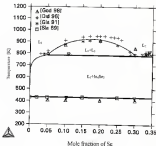


Figure 5.4 Comparison between the calculated Se phase diagram and experimental data on the vicinity of the Se-rich azeotropic gap.

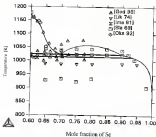


Figure 5.3 Comparison between the calculated Fe-Si phase diagram and various experimental data on the vicinity of the eutectic temperature [99]

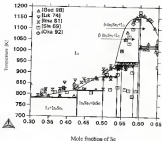


Figure 3-4 Comparison between the calculated Fe-Fe phase diagram and various experimental data from 0.3 to 0.85 mole fraction of Fe

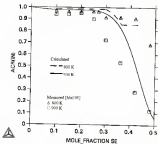


Figure 8.7 Calculated activity of H_2 with the experimental data [Maj 16] with the pure liquid H_2 phase as the reference state

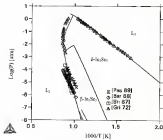


Figure 18 Comparison of the total vapor pressure in the In-Sn system with the experimental data

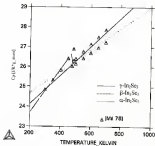


Figure 3-17 Assumed and measured heat capacity data for α - In_2Se_3 , β - In_2Se_3 , and γ - In_2Se_3 .

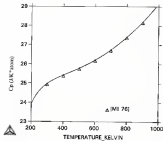


Figure S 10: Assessed and measured heat capacity data for Al_2O_3 .

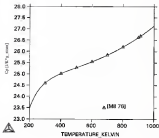


Figure S 11 Assessed and reviewed heat capacity data for In_2O_3 .

CHAPTER 4

Cu₂S₂ THEN FILM FORMATION BY RAPID THERMAL PROCESSING

4.1 Introduction

In conventional slower film formation processes, CuS is not directly formed during the film film-deposition process. Rather, the requirement for a large area, high throughput and low cost slower film formation process has motivated the use of physical deposition techniques using elemental sources to first deposit a precursor film of an appropriate overall composition. Subsequent annealing then leads to the synthesis of large grained CuS. *Selenization* and *Stacked Elemental Layer (SEL)* techniques are two promising processes. *Selenization* is a two-stage technique. Firstly, sequential layers of copper and selenium are deposited on a molybdenum coated substrate. CuS is then obtained by reacting the metal precursor with gas phase Se, either H₂Se or Se vapor. The SEL technique is a process involving the sequential deposition of Cu, Se and Se layers on a substrate which is then annealed in vacuum or a Se environment to promote reaction of the elements to form CuS. Among the annealing techniques, RTP is attractive with the advantages of low thermal budget and better control of the process kinetics.

4.1. Previous Work on RTP-CIB

Several precursor structures have been utilized in RTP synthesis of CIGS, the most commonly, three types of precursor structures have been reported in the literature.

One type of precursor structure studied for elemental composition is film-molecule-like structure. A variety of precursors could be fabricated by alternating the layer sequence and changing the number of layers. Compositions of the films were controlled by the relative thickness of the individual layers. It often incorporated errors in due to the high volatile nature of the gas species. A number of groups have reported successful CIGS film formation using this approach including (Chen 99, Kim 99, Kim 94), or $\text{CuIn}_{1-x}\text{Ga}_x\text{S}_2$ (Jin 94, Kim 94).

The important processing parameters in this approach include stacking arrangement of the layers, Cu/In ratio, RTP mapping rate, and sintering temperature.

The first device quality CIGS produced by RTP was synthesized by Wang et al. (Kim 94). It consists of Mo, Cu, In, and Se sequentially deposited by DC-magnetron sputtering (Mo, Cu, In) under composition (Cu, In, Se). The Cu/In ratio varied from 0.45 to 0.65, while Se was typically 40% in excess of the stoichiometric amount. A furnace type flow stage oven, (TCA) processing was also performed in their investigation. Two critical process steps were found from this type of process. The first one is the severe denaturing of the amorphous Se layer starting at above 100°C which causes a locally inhomogeneous nucleation and grain growth of the CIGS layer. This locally inhomogeneous growth process resulted in voids between the CIGS and Mo back contact, which produced poor adhesion and low cell performance. The second critical process point is when the sample

in the temperature range of 100 to 150°C where the formation of Cu_2S is desired as compared to Cu_2Se , a detrimental secondary phase. Their results indicated the Cu/S ratio is the most significant parameter. At a Cu/S precursor of 1:19 small grained material is obtained in contrast to the coarse grained film at Cu/S of 1:12 with a grain size in the range of 1–3 μm . TEM results revealed that copper-rich and sulfur-rich films were deficient in their defect structure. Copper-rich films had a significant number of dislocations and stacking faults. In contrast to copper-rich films, there were a significant number of twins in sulfur-rich films. These features revealed different reaction mechanisms during synthesis for these two Cu/S ratios.

Using the same process strategy [Pro 16] fabricated the $\text{Cu}_2\text{S}/\text{Cu}_2\text{Se}$ thin film cells by RTP. They also developed two steps to incorporate sodium into CIGS to quantify its impact on grain morphology and cell performance. They varied the co-diffusion of sodium from the soda-lime glass by employing a partially permeable film backbufferoxide as the first process. Sodium chloride was added to the precursor in the second process. The optimization of the sodium content in RTP-CIGS films on soda-lime glass resulted in cells with averaging efficiency 32% and a peak efficiency of 13.2%.

More recently Probst *et al.* [Pro 16] developed a new stacked elemental layer process to produce $\text{Cu}_2\text{S}/\text{Cu}_2\text{Se}$ and $\text{Cu}_2\text{S}/\text{Cu}_2\text{Se}/\text{Sb}_2\text{S}_3$ cell. The key process steps are (1) deposit a barrier coating on the soda-lime glass substrate (sandblasted and sput a sodium compound to the elemental $\text{Cu}_2\text{S}/\text{Cu}_2\text{Se}$ precursor stack (2) rapid thermal processing the structure to form CIGS thin films. The first step barrier controls the sodium distribution. A thin layer of SnO_2 , Al_2O_3 or Si_3N_4 was used as the barrier material. They suggested a liquid assisted growth mechanism for the stacked elemental layer process but two main

prospective: 1) the processing conditions must drive the formation of the Cu_2S phase, 2) a dynamic heating process is needed to exceed the melting temperature of Cu_2S before it is consumed in the reaction. Cell peak efficiencies of 13.3% for $\text{Cu}_2\text{S}/\text{Sn}/\text{AgCl}_2$ and of 14.6% for $\text{Cu}_2\text{S}/\text{Cu}_2\text{SnS}_3$ -deposits were obtained with this technique.

The second precursor structure used as evaporating electrode (Cu_2S to seed Sn) [John 91, Gab 92]. This processing approach had bubbling and refluxion problems, especially with Mo-coated glass substrates. The bubbling was worse with higher Cu contents and lower ramp rates. The device made from this approach had an efficiency < 3%, after 220°C an annealing an efficiency 3.3% was obtained.

The third approach used RTP to re-crystallized Cu_2S , Allen et al. [Abb 93] used thermal annealed small-grained (<1 μm) Cu_2S , to producing large-grained Cu_2S (>100 μm). This approach suffered from the severe oxygen incorporation and Cu_2S -decomposition at high temperature, and other defects such as numerous voids and particles in the films.

It is learned from this review that the precursor film structure and the subsequent reaction pathway during annealing can dramatically affect the eventual device performance. For example studies by [Mat 98] showed a different chemical reaction pathway when the precursor was formed by mixing powders of pure Cu, Sn and Sn in the 1:1:2 stoichiometry as compared to mixing powders of the stoichiometric compound Cu_2S with Sn in the same stoichiometry. The latter approach led to Cu_2S formation at a much lower temperature.

This is consistent with the observation that a unidirectional Cu-Sn-S₂ amorphous mixture [Gab 92, Moo 96] precursor structure does not lead to device

quarry CTS films, in contrast to the sequential SCL process. In the SCL process the elements are sequentially deposited on a substrate usually in the sequence substrate/Cu/In₂O₃ [Fro 56]. This precursor structure usually leads to the formation of a Cu₂In₂ intermetallic phase during its intermediate reaction step [Kor 73]. Based on these results it is anticipated that alternative precursor structures might yield improved CTS thin film growth.

4.3 Reaction Pathway Engineering

Phase diagram information is essential in designing the precursor structure. Figure 4-1 shows the Cu-In-Sn ternary composition diagram along with the accepted intermetallics and several tie-lines connecting pairs of them. Inspection of this diagram suggests several reaction pathways to quaternary CuInSn, from binary compounds using RTP. Although previous approaches have started with the pure elements or from a physical mixture or a stacked layer structure, certain advantages exist when starting with binary compounds. Among these compounds those within the Cu-In and In-Sn couples are attractive due to existence of low melting temperature phases [Jin 97]. There are several combinations of these two couples that could lead to CTS formation. The following guidelines were used to suggest suitable Cu-In and In-Sn compounds to serve as precursors for *in situ* RTP synthesis of CTS.

- + Avoid high melting temperature phases such as In₂Sn and Cu₂Sn, especially the coexisting Cu₂Sn secondary phase
- + Utilize an intermediate liquid phase to assist grain growth
- + Minimize evaporation losses during RTP

- Select highly reactive parts

At first glance, one choice would be to deposit a bilayer structure of Cu_2Se and In_2Se_3 and treat them to form CSE according to



Examining the calculated $\text{Cu}_2\text{Se}-\text{In}_2\text{Se}_3$ pseudobinary T-x phase diagram (Figure 6.2) reveals that the liquid phase that exists at the lowest temperature in this system is the -40°C eutectic alloy lying in the In_2Se_3 -rich composition field. This temperature is much too high for the glass substrate.

An examination of Cu-Se (Figure 6.3) and In-Se (Figure 6.4) binary T-x diagrams from chapters 4 and 5 suggests that a more suitable combination would be selenium-rich copper compounds ($\text{CuSe} - \text{Cu}_2\text{Se}$) and selenium-rich indium compounds (biller In_2Se_3). When these binary compounds are heated the copper compounds will form a liquid phase and the indium compounds will form a solid-liquid mixture in the temperature range 533 to 628°C . To reach the liquid phase, rapid thermal processing might be required to avoid sub-solid phase transformations. The binary diagrams show, however, the net results of a liquid phase exists after the melting procedure like enters the primary domain.

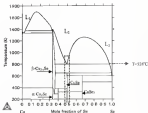


Figure 4.3 Cu-Sn binary T-x phase diagram

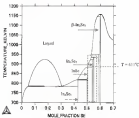


Figure 4-4 Bi-Sb binary T-x phase diagram

It should easily volatize to leave single phase CIS. An assessment of the ternary Cu-In-Sn phase diagram has been developed, and a projection of the liquidus surface is shown in Figure 4-6. With this diagram possible compositional combinations can be further evaluated. In particular, the entire valley between the binary eutectic compositions E_1 and E_2 should be easily depressed and thus cast at slightly below 220°C. The dash line in Figure 4-6 connecting the pure Sn corner to the CuInSn compound indicates it should be possible to form CIS in the presence of an intermediate low-temperature liquid phase by the reaction:



The relative amounts of the binary components should be adjusted to be on this line.

The above approach suggested a precursor structure that consists of an In-Sn layer (58 to 75 Sn at %) just coated over an In-Sn phase diagram in Figure 4-4) deposited on a Cu-In (20 to 33 Sn at %) (see dashed line in Cu-In phase diagram in Figure 4-3) layer, which is deposited on a Mo coated substrate film surface. A schematic diagram of the structure is given in Figure 4-5. The composition ranges for the binary parts and the overall precursor films are indicated in Figure 4-6 as binary lines along the In-Sn and Cu-In lines near the CuIn and InSn compounds. With this composition a Cu-Sn liquid phase should form to make growth and the small amount of remaining excess Sn should be volatile. The presence of solid In-Sn layer on top will minimize the composition loss during the RTP process.



Figure 4.5 Proposed processor structure

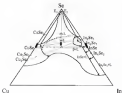


Figure 8.6 Liquidus projection for Cu-Sn-In ternary system.

4-4 Precursor Growth

A low temperature precursor growth is desirable for higher manufacturing equipment throughput, lower equipment cost, lower thermal budget, and thus a lower capital cost for modules. A rotating-disk evaporation-enhanced deposition system was used for precursor deposition, which included two Langmuir-Blodgett sources for copper and sodium and a double-core thermal evoking source for selenium. A schematic drawing of the reactor is shown in Figure 4-7. The growth conditions (substrate temperature and flux ratio) of the binary systems have been thoroughly studied by [Farr 92]. In their investigations they utilized a Langmuir-Blodgett source and suggested the low selenium evoking coefficient is most likely due to the formation of larger polymer molecules (e.g., Se_8). The use of a evoking source allowed the Se decomposition temperature to be adjusted independent of source temperature (flux control) and thus control the selenium flux species distribution.

The precursor films used in this study were deposited at a 200°C substrate temperature. To fabricate the desired precursor structure, the In-Se and Cu-Se growth conditions were studied separately by fixing the selenium flux constant and adjusting the selenium to copper and selenium to sodium molar flux ratios. The molar fluxes were cross-calibrated by RHEED and quartz-crystal monitors.

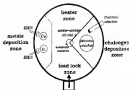


Figure 8-7 Schematic diagram of the migration-enhanced epoxy reaction

2.4 Film Characterization

The film morphology was studied by phase-contrast and cross-section Scanning Electron Microscopy (SEM). Compositional analysis was performed by Inductively Coupled Plasma (ICP) emission spectrometry for the major cations of CM. The samples were dissolved in 5 % (by volume) nitric acid. The standard solution is also based on 5% nitric acid. Composition depth profiles were measured by spatially Auger Electron Spectroscopy (AES) using a Perkin-Elmer P5400 AED/AAS microscope equipped with a CMA spectrometer and an Ar-ion gun. All spectra were obtained at 30 kV.

The structural properties of the films, such as phase constitution, crystallinity, and texture were determined by Powder X-ray Diffraction (PXRD) and Grazing Incidence X-ray Diffraction (GIXRD) at various angles. The GIXRD measurements were carried out using a Siemens diffractometer equipped with an area detector using Cu K α radiation. This non-destructive technique allows determining the depth distribution of the phases in the film. The utilization of an area detector provided the opportunity to assess the texture of the films at the same time. The texture is measured when diffraction peak intensities are needed to identify the phase constitution.

The unpolarized Raman scattering signals were measured using a double monochromator at Ar⁺ laser excitation at two wavelengths (488 nm and 497 nm) and standard backscattering sample geometry. The longer wavelength excitation laser will provide information with deeper penetration in the film.

4.7 Results and Discussion (Previous literature)

Two precursor structures were fabricated. The first one possesses a three layered structure, $\text{InGa}/\text{CuInGa}/\text{CuInGa}$. The second one possesses a two layered structure InGa/CuIn .

4.7.1 Precursor structure

It is a challenge to distinguish CuInGa from CuIn using XRD spectra since most of the peaks overlap. A major difference is the powder spectra between these two phases is the peak intensity ratio of the $[111]_{\text{CuIn}}$ and $[002]_{\text{CuIn}}$ is 4:1 for CuIn and $[111]_{\text{CuInGa}}$ is 3 for CuInGa phase. Simulated powder XRD patterns for CuInGa and CuIn were given in Figure 4.12(a) and (b) respectively. Unfortunately, the possibility of preferred orientation renders this difference useless in a conventional diffractometer equipped with a point detector. With the aid of an area detector, the difference can be exploited. An area detector allows measurement of the effects of preferred orientation. It is clearly seen in Figure 4.11 that only those diffraction rings belonging to the InGa substrate indicate signs of spurring. The XRD spectra of the precursor film taken at various X-ray incident angles (0.3 to 4°) clearly shows a change of the relative intensity of the peak around $2\theta = 26.2^\circ$ $[111]_{\text{CuIn}}$, $[111]_{\text{CuInGa}}$ and the peak around $2\theta = 44.5^\circ$ $[002]_{\text{CuIn}}$, $[002]_{\text{CuInGa}}$. The relative intensity for peak at 44.5° is increasing with the X-ray incident angle as shown in Figure 4.13 (a) and (b). All the spectra from the presence of InGa phase in addition to CuIn and CuInGa . These data suggested a three layered structure, $\text{InGa}/\text{CuIn}/\text{CuInGa}/\text{InGa}$, was formed in the deposition process.

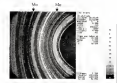


Figure 2-11 X-ray diffraction pattern at 2° incident angle of the precursor SiO_2 .

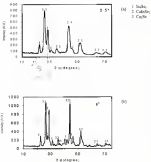


Figure 4.12 XRD spectra of pretreated SAs measured at (a) 2θ incident angle and (b) 2θ incident angle.

The Raman spectra shown Figure 6-13(a) and (b) provide further evidence for the structure. A much more intense CuInSe_2 phonon peak is evident in the spectrum measured at 514 nm as compared to the one measured at 477 nm.

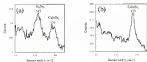


Figure 6-13 Raman spectra at two excitation wavelengths: (a) $\lambda = 477$ nm and (b) $\lambda = 514$ nm measured on the precursor film.

KPFM

The majority of the InSe_2 phase disappeared and reacted to form CuInSe_2 after 200°C (TC temperature) RTP annealing for 70s as indicated by the XRD spectrum shown in Figure 6-14. The appearance of the (100) peak and the increasing (112) peak intensity of CuInSe_2 are good indications of production of additional Cu. The XRD patterns vary only slightly with various X-ray incident angles. This indicated the heavy precursor layer was reacting and formed more CuInSe_2 during the RTP. GIXRD spectra

however still shows the presence of β -Sn peaks. This indicates the reaction is not complete at the processing conditions. The XRD spectra at 4° incident angle are given in Figure 4.17.

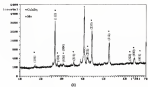


Figure 4.14 XRD spectrum of the film after RTP at 250°C (300 temperature) for 75 s.

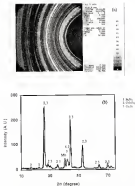


Figure 6.11 (a) X-ray diffraction pattern (b) integrated spectra at h^* incident angle of the film after RTP at 200°C (TC temperature) for 78 s

RTD-600

Figure 6.16 shows the XRD pattern of the film after annealing at 500°C for 70 s. The spotty pattern instead of the ring pattern for the precursor film indicated a dramatic grain growth process at this annealing temperature. The reason for this enhanced grain growth is the formation of an In-Sn liquid by $\text{In}_{25}\text{Sn}_{75}$ undergoing a monotectic reaction (see Figure 5.1). Figure 6.17 shows the XRD diffractogram measured at 0.5° incident angle indicated formation of Cu or Cu_2In intermetallics and high temperature Cu_{10}Sn phases in the near surface region. Figure 6.18 shows an integrated XRD spectrum measured at 0° incident angle.

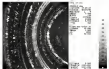


Figure 6.16 X-ray diffraction pattern at 0° incident angle of the film after RTD at 500°C (70 s temperature) for 70 s.

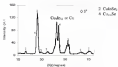


Figure 4-17 XRD spectra at 0° incidence angle of the film after RITP for 10 s at 500°C (9C)

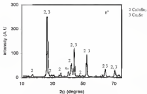


Figure 4-18 X-ray diffraction spectra at 0° incidence angle of the film after RITP at 500°C (TC temperature) for 10 s

Microbiology

Plane-view (a, c, e) and cross-sectional (b, d, and f) SEM photographs of the precursor and RTP films are given in Figure 6.10. The plane-view SEM photograph shows no change in the surface morphology after the 350°C (TC temperature), 70 s heat treatment (Figure 6.10(a)). A significant change was observed in the cross-sectional photograph in Figure 6.10(b). These results suggested an interface reaction between the precursor layers, and the reaction did not extend to the top surface region. Dramatic changes were observed after the 350°C (TC temperature), 70 seconds heat treatment in both plane-view and cross-section photographs as shown in Figures 6.10(c) and (f). The surface morphology suggests a liquid phase formed during the rapid thermal process. This could be attributed to the melting of In_{2}O_3 phase, which undergoes a binary peritectic reaction at 324°C (see Chapter 3). This is an expected result since we already know the temperature on the surface is about 350°C, higher than the TC temperature at this ramp rate as indicated by our temperature calibration studies.

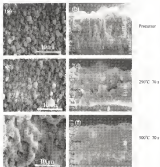


Figure 4. LE Flat-view and cross-section SEM photographs of the precursor and RUP films

Compositional Analysis

The overall composition of the samples was analyzed by ICP spectrometry. The estimated uncertainty for ICP analysis is 10–25% relative. Major sources for uncertainty are variability in the plasma, variability in the pump rate, and variability in the solution efficiency. The precursor has an overall composition of Cu (a.t.%) = 15.1 ± 15.2 (a.t.%). The AES survey spectrum for the as-received precursor is given in Figure 4.23. The oxygen signal indicated the precursor surface is mostly covered by native oxide. The surface composition estimated by AES is given in Table 4.1. The peak intensity depth profile data are shown in Figure 4.24. The oxygen signal decreased drastically after sputtering for a short time. The bottom layer composition, as estimated by AES, is given in Table 4.1. The depth profile is consistent with the XPS data, which suggested the formation of a thin layer, $\text{In}_2\text{Se}_3/\text{CuInSe}_2/\text{Cu}_2\text{Se}$, structure.

Table 4.1 ICP chemical analysis of the investigated samples

Sample	Cu (a.t.%)	In (a.t.%)	Se (a.t.%)
Precursor	15.6	13.2	39.2
as-received, 10 s	16.3	23.3	34.6
as-received, 10 s	16.1	23.6	34.3

RTP 280

The overall composition of the films changed a little after RTP at 280°C (10 s) for 70 s as shown by the ICP data in Table 4.1. However, the AES data shown in Figure 4.23 did show a dramatic change after RTP. The depth profile clearly showed a deep Cu diffusion from the backside of the film into the top In_2Se_3 layer. This indicated the

reaction front between Co_2Si and $\text{InGa}_{0.5}\text{Sb}_{0.5}$ layer was moving forward and forming $\text{CoInGa}_{0.5}\text{Sb}_{0.5}$ during the RTP. This is consistent with the XRD data, which showed the disappearance of XRD $\text{InGa}_{0.5}\text{Sb}_{0.5}$ peaks and increasing $\text{CoInGa}_{0.5}\text{Sb}_{0.5}$ peak intensity. However, the reaction mechanism is mainly through solid state diffusion.

4.1.7. SEM

Again the overall composition of the film changed a little after RTP at 500°C (SC) for 70 s as shown by the RTP data in Table 4.1. This clearly demonstrates an advantage of using binary layers as precursors as compared to stacked elemental layer structures. The AES survey spectrum on the as received sample is given in Figure 4.24. The strong Co signal indicated the reaction had reached the surface of the film during the RTP. The AES depth profile given in Figure 4.25 showed a uniform distribution of Co, In and Sb atomic species. Such fast mass transport is believed to be a result of liquid phase formation as $\text{InGa}_{0.5}\text{Sb}_{0.5}$ underwent a eutectic reaction, as supported by the XRD and RPD data.

Table 4.2. Precursor film surface composition measured by AES

Element	Atomic %
C	49.7
Cu	23.4
Se	26.2
Sr	11.4

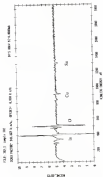


Figure 4.20 AES survey scan on as-received precursor film

Table 6.1 Precursor film composition measured by AES after 100 runs sputtering

Element	Atome %
C	5.3
Co	42.6
Fe	3.8
As	32.6
Sb	15.7

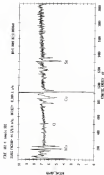


Figure 6.21 AES survey scan on precursor film after 100 runs sputtering etching

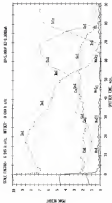


Figure 4.21. AEG depth profile of the pressure film

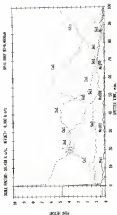


Figure 4.13 AIC depth profile of the film after RTP at 250°C.

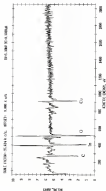


Figure 6.20 AEG survey scan of the film surface after RTP at 500°C

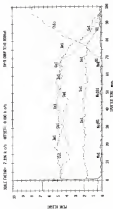


Figure 6.21 AEG depth profile of the film after RTP at 500°C.

4.4 Sample and Structure-Property Relationship

Process

The composition analysis for the precursor and the reference binary layers is shown in Table 4-4. The WDS analysis is in agreement with the ICP data for the binary samples. For the 4-layer precursor structure, WDS is not able to provide the correct overall composition. The ICP data show the overall precursor structure is a slightly Cu-rich. The overall composition should be adjusted by increasing the In-Sn binary layer thickness.

The XRD spectra are shown in Figures 4-26 and 4-27 for the In-Sn and Cu-Sn reference samples, respectively. The In-Sn layer primarily consists of small crystallites, which showed a broad peak in the XRD spectrum. The Cu-Sn layer mainly consists of the α -Cu-Sn phase. The XRD spectrum for the 4-layer precursor is given in Figure 4-28. The maximal peak height at 35° - 35.7° value and the small extra peak 28° - 34.3° indicates a small amount of pre-nucleation to form Cu-Sn alloy during the deposition process. A schematic drawing for the precursor structure is shown in Figure 4-29. The AES depth profile of the precursor film given in Figure 4-30 is consistent with the structure.

Table 4-4. Composition analysis

Sample	ICP	
14-12 (Cu-Sn reference)	Cu: 51.85	Sn: 48.93
14-4 (In-Sn reference)	In: 50.53	Sn: 49.52
14-14 (4-layer precursor)	Cu: 51.74	In: 27.84, Sn: 49.57

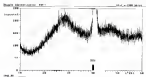


Figure 4-26 XRD spectrum for In-Sn binary reference sample

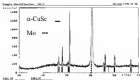


Figure 4-27 XRD spectrum for Cu-Sn binary reference sample

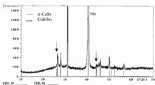


Figure S 14 XRD spectrum for the bilayer precursor

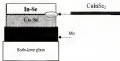


Figure S 15 Schematic drawing of the bilayer precursor

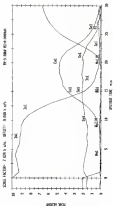


Figure 6.30. AGL depth profile of the precursor structure-11.

A set of experiments was performed to understand the influence of ramp rate. Three ramp rates (1, 3, and 10 °C/s) were used in the study. The slow ramp rate resulted in bubble formation and delamination of the film. A phase-contrast optical micrograph is shown in Figure 4.11. The mechanism can be easily understood by examining the Cu₂Se binary phase diagram shown in Figure 4.3. The CuSe phase decomposes to form Cu₂Se phase and Se₂ vapor during the heating process before forming the CuSe liquid phase. The production of Se₂ vapor causes bubble formation and thus delamination of the film.

At higher ramp rate, it is expected that the single liquid phase domain will appear more quickly. Although the Se vapor pressure is very high (Figure 4.3) in this domain the mass transport and reactivity are often much higher. On the other hand, at the slower ramp rate most of the α -CuSe phase has time to transform to Cu₂Se before the temperature can reach the single-phase domain. Thus, the higher ramp rate produced more Cu₂Se, with better crystallinity and reduced delamination. This is clearly shown in the optical phase-contrast image of the RTP film presented at a ramp rate of 10 °C/s (Figure 4.12). The XRD spectra for the 10 °C/s₁ and 1 °C/s₁ scans are shown in Figure 4.13 and 4.14, respectively. The XRD spectra indicate the peaks for the 10 °C/s ramp rate RTP sample have higher intensity than the corresponding XRD peaks presented at a ramp rate of 1 °C/s.

A reference α -CuSe binary film was subjected to RTP treatment at a ramp rate of 1 °C/s for 10 s to further confirm this conclusion. WDS analysis indicated the film composition changed from Cu 39.13, Se 49.46 to Cu 60.78, Se 39.22. XRD analysis indicated the film has changed to the Cu₂Se phase (Figure 4.15). These results clearly show the Se₂ vapor-expelled from α -CuSe during the RTP process to produce Cu₂Se.

The ICP analysis of the buffer layer samples after RTP treatment is given in Table 4.1. In contrast to the result for the RTP experiment of reference *n*-GaIn sample, the ICP data indicated the overall film composition did not change much after the buffer-layer precursor was subjected to RTP treatment.

These results are encouraging that our precursor structure design is feasible. Putting the buffer layer on top of the GaIn layer to maintain the film, evaporation loss appears to be effective. Figure 4.14 shows the AES depth profiles of the film after RTP treatment with a ramp rate of 10°C/s and annealed at 450°C (TC temperature) for 10 s. A uniform composition profile was achieved throughout the film. The high mass-transport and reaction rate is believed to be a result of liquid phase formation in the GaIn layer. Phase-contrast SEM photographs of the precursor film and the film after RTP annealing (10°C/s) are shown in Figure 4.15a and b, respectively. The SEM images show the formation of crystals with grain size on the order of several microns.

Table 4.1 Composition analysis for RTP treatment

Sample	924.145	Ca 36.76	As 16.11	
100.0 g GaIn precursor				
GaIn buffer layer after RTP (10°C/s)	92.9	Ca 37.56	As 17.16	As 16.46
GaIn buffer layer after RTP (10°C/s)	92.9	Ca 36.61	As 16.66	As 16.17



Figure 4.14 Phase-contrast optical micro-graph of the sample after 10°C/s



Figure 6.12 Phase-contrast optical micrograph of rough state (10 °C).

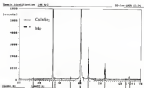


Figure 6.13 XRD spectrum for KTP $\text{Ca}_{0.95}\text{Si}_{0.05}$ film with rough state at 10 °C.

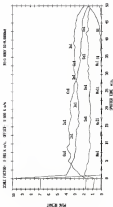


Figure 6. 30-MHz depth profile of the pressure structure (1).

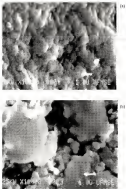


Figure 6-10 The photo-view SEM photographs of the precursor (a) and RTP (b) films

4.3 Conclusion

Three different CuInSe₂ layer growth mechanisms are proposed in Figure 4.28, 4.29 and 4.30. The first growth mechanism is solid state inter diffusion between In₂Se₃ and Cu₂Se binary layers (Figure 4.28). The second growth mechanism is a liquid-solid reaction due to the melting of In₂Se₃. CuIn-grown CuInSe₂ crystals grew from the liquid-solid reaction. Uniform mass-transport was observed in short time (10 s) as shown in the AES depth profile (Figure 4.25). The main phase to appear is the film after 100°C RTP are CuInSe₂, CuSe and a small amount of a Cu-In inter-metallic phase. The third mechanism is a liquid-solid reaction due to the melting of n-CuSe in the In₂Se₃ layer. CuIn-grown single phase CuInSe₂ crystals were synthesized from the liquid-solid reaction as suggested in the reaction pathway analysis (Figure 4.3). Uniform mass-transport was achieved in short time (10 s) as shown in the AES depth profile (Figure 4.34).

In this study an alternative strategy for low temperature pressure fabrication of CIS films has been proposed and tested using *ex-situ* rapid thermal processing. The experiments showed that large grain CIS could be synthesized through this approach.

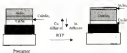


Figure 6.18 Illustration of the solid state diffusion growth model

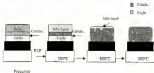


Figure 6.19 Illustration of the liquid assisted growth mechanism for precursor structure 1



Figure 4-58 Illustration of the liquid axonal growth mechanism for precursor structure II.

CHAPTER 7

X-RAY ABSORPTION FINE STRUCTURE (XAFS) INVESTIGATIONS OF COPPER INDIUM SELENIDE SEMICONDUCTOR ALLOYS

Cd-based solar cells have been thought to be p-n structures (p-CdS /n-CdS). However, such a model does not predict the failure of high-Cd-content devices. A novel model has been proposed by Ichim et al. [Ich 92] that the growth kinetics of PYG-grown CdSe/Si result in the formation of a surface layer of CdSe/Si and that the CdSe/Si/CdSe/Si heterojunction is the true heterojunction partner in CdS devices. This surface material is reported to show composition close to CdSe/Si and has been referred to as an Ordered Vacancy Compound (OVC). The significant finding, contrary to earlier observation of a buried junction elucidated by electron-beam induced current (EBIC) [Miz 84] measurements. However, the crystal structure of CdSe/Si and its phase relation with CdSe/Si is still not clear at this point. In this chapter a detailed study of the local structure of CdSe/Si and CdSe/Si by X-ray Absorption Fine Structure was reported.

7.1 Introduction

X-ray absorption fine structure (XAFS) spectroscopy refers to the measurement of the modulation of the X-ray absorption coefficient, μ , as a function of photon energy, E , at and above the X-ray absorption edge. One of the major advantages of XAFS is its atomic selectivity, which is capable of probing the local structure of each atomic constituent of a sample. Conventionally, EXAFS spectra refer to the region 45 to 1000

qV above the absorption edge. The pre-edge region contains bonding information such as the electronic configuration, and the site symmetry. In between the pre-edge and the EXAFS region is the X-ray Absorption Near Edge Structure (XANES) which contains information about the local electronic structure and geometrical configuration of the materials. Figure T 1 shows a typical X-ray absorption spectrum around an absorption edge.

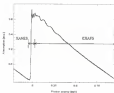


Figure T 1 A typical XAS spectrum

7.2 Theory of ESCAPE

K , L , and I represent the intensity of the incident X-ray beam and transmitted X-ray beam respectively. the relation between K and I is given by

$$I = I_0 e^{-\mu(E)x} \quad (7.1)$$

In this equation $\mu(E)$ is the X-ray absorption coefficient, E is the photon energy, and x is the sample thickness. The term $\mu(E)$ is a monotonically decreasing function of E in most energy ranges. When the photon energy equals the binding energy of a core electron, a sudden increase in μ due to the photoelectric absorption. This energy is denoted as E_0 , the threshold energy. When the electrons are in the $n=1$ shell the absorption edge is called the K -edge. For the $n=2$ shell, the corresponding edges are called the L -edges. In the photoelectric process, the energy of an X-ray photon is absorbed by a core electron and promoted to an unoccupied valence level or to continuum. The measurement of the excited photoelectron can be determined by the relation

$$p = \sqrt{\frac{2m(eV - E_0)}{\hbar^2}} \quad (7.2)$$

where p is the momentum of the photoelectron, h is Planck's constant, m is the electron mass, and e is the X-ray-photon frequency.

For an isolated atom the photoelectron release can be represented as an outgoing wave as shown in Figure 7.2 by the solid lines. When the absorbing atom is surrounded by other atoms as in top molecules or condensed phase, the outgoing photoelectron wave is indicated by the surrounding waves as indicated by the dashed lines in Figure 7.2.

The final state is the superposition of the outgoing and the scattered waves. The backscattered waves will add or subtract from the outgoing wave in the center depending on their relative phase. The total amplitude of the electron wave function will be enhanced or reduced, thus modifying the probability of absorption of the X-ray. The absorption coefficient μ is proportional to the square absorption cross section σ . If we denote P as the probability of an atom absorbing a photon of energy $h\nu$ from the Fermi Golden rule within the dipole approximation gives

$$P = 4\pi e^2 \hbar^2 \left| \langle f | \hat{r} | i \rangle \right|^2 \delta(E_f - E_i - h\nu) \quad (2.3)$$

where $|i\rangle$ and $|f\rangle$ represent the initial and final states with E_i and E_f as the corresponding energies respectively. $\alpha = \frac{e^2}{\hbar c}$ is the hyperfine structure constant, \hbar is the Planck constant divided by 2π , e is the electron charge, c is the speed of light, ϵ is the dielectric field polarization vector of the X-ray photon, r is the position vector of the electron with respect to the cluster atom, and ω is the angular frequency of the photon.

In EXAFS we are only interested in the oscillatory part of the total absorption. A simple way of deriving the EXAFS equation is by combining one-electron single scattering in plane wave approximation. With these approximations the oscillatory part $\chi(k)$ of the total absorption coefficient $\mu(k)$ can be described by the summation of one wave originating from all neighboring atoms, and the EXAFS equation is defined as [Bey47]

$$\chi(k) = \sum_j \frac{N_j}{k^4} f_j^2(k) \sin(2kR_j) \exp\left(-\frac{4R_j^2}{\lambda_j^2}\right) \exp(2\sigma_j^2 k^2) + f_j^2(k) \quad (2.4)$$

Here j refers to the j th coordination shell, \bar{R}_j is the average coordination distance, $\langle R_j^2 \rangle$ is the phase shift experienced by the electron in the scattering process, \bar{N}_j is the average coordination number in the j th shell and σ_j^2 is a Debye-Waller type of term which represents the root mean square fluctuation in \bar{R}_j caused by thermal motion of the atoms and the structural disorder, $F_j(k)$ is the back-scattering amplitude, $F^*(k)$ is an amplitude reduction factor which accounts for the photoelectron energy loss due to many body effects and shake-up/shake-off processes, and the term $e^{-2M_j(k)}$ accounts for the finite lifetime of the excited state.



Figure 7.1 Debye-Scherrer patterns of the final state wave function

Effect of Thermal Vibration and Lattice Expansion

The Debye-Waller factor e^D in the EXAFS equation has two contributions: the thermal vibration, e^D_{th} , and static disorder, e^D_{st} . It is important to note that the e^D in the EXAFS equation (7.6) is different from the Debye-Waller term, e^D , in diffraction. The e^D term in diffraction accounts for the mean square displacement of the atoms from its lattice site, while for EXAFS e^D_{st} is the relative deviation between the scattering and backscattering atoms. Thus in EXAFS the vibration modes causing the mean path of electron moving in the same phase and amplitude have no contribution to e^D . e^D_{th} could be calculated from first principle (Eqs. 94) or indirectly using the Einstein or Debye approximations. The Einstein model assumes the single optical vibration frequency ω_0 and is given by

$$e^D_{\text{th}}(T) = \frac{3}{4M\rho_0} \left(\frac{1}{2} + \frac{1}{e^{\hbar\omega_0/2kT} - 1} \right) \quad (7.9)$$

where M is the reduced mass of the scattering atom and backscattering atoms pair

In the Debye model, the $e^D_{\text{th}}(T)$ has a simple form given by

$$e^D_{\text{th}}(T) = \frac{3}{4M} \left(\frac{3\pi}{\alpha_0} \left[1 - \frac{\text{erf}(\alpha_0 \theta_D / \sqrt{e})}{\alpha_0 \theta_D / \sqrt{e}} \right] \right) \text{erfc} \left(\frac{\theta_D}{2\alpha_0} \right) \frac{d\theta_D}{d\alpha_0} \quad (7.10)$$

with

$$\alpha_0 = \frac{3\pi k_B \theta_D}{\hbar}, \quad \theta_D = \frac{\hbar \omega_D}{k_B}, \quad \text{and} \quad k_D = \left(\frac{6\pi^2 N}{V} \right)^{1/3} \quad (7.11)$$

where θ_D is the Debye temperature, N is the number of atoms, and V is the crystal volume.

The structural-disorder Debye Waller factor w^2 , measures the degree of deviation of the equilibrium interatomic distance of each cluster and backbone from the average bond length R . w^2 is given by:

$$w^2 = \sum_{j=1}^N \frac{(R_j - R)^2}{N} \quad (7.14)$$

where R_j is the equilibrium bond length of j th atom in that shell

7.3 Experimental XAFS Apparatus

An X-ray source, X-ray optics, and the X-ray detector are the primary experimental system for XAFS experiments. A schematic diagram for the experimental setup is shown in Figure 7.1.

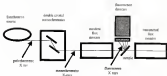


Figure 7.1 Schematic diagram for XAFS experiment

THE X-RAY SOURCE

A high-intensity X-ray source with a continuous energy spectrum is necessary for XAFS experiments. The principal X-ray source used for XAFS is that from an accelerating charge particle beam radiator. Synchrotron radiation is the most widely used X-ray source for XAFS experiments. All the measurements in this study were done at the Materials Research Collaborative Access Team (MRCAT) beam line, Advanced Photon Source, at the Argonne National Laboratory.

The beam acceleration and storage process begins at the electron gun, which emits electrons that exit the gun at 100 keV. Electrons are raised to an energy level of 100 MeV by a series of accelerating structures in the first-stage linear accelerator (linac). Next, the 100-MeV beam of electrons strikes a 7-mm-thick tungsten positron conversion target, which produces electron-positron pairs. Positrons are accelerated to 450 MeV by the second-stage linac. The 240-m-long booster synchrotron raises positron energy at a rate of 50 keV per turn. In 0.15 s positrons strike the booster 20000 times as their energy climbs to 1 GeV. The positrons are then injected into the 104-m-circumference storage ring. The positron beam strikes the storage ring more than 27,000 times per second, stored and focused by 100-T powerful electromagnets as it circulates. The beam decelerates at a rate of about 5 MeV per turn as it emits synchrotron radiation. The energy loss is replaced by the 210-MHz storage ring rf system.

Every 10 to 20 hours, the storage ring is refilled with positrons. A storage ring is actually a set of curves connected by straight sections. Linear arrays of north-south permanent magnets with alternating polarity are inserted into the straight section (hence the name insertion device—ID) one array above the beam path, the other below. When

charged particles in the storage ring pass through the steering fields they either wiggle or undulate, depending on the configuration of ID. This action greatly enhances the synchronous radiation.

3.3.3 X-ray beam line optics

The X-ray beam line optics consist a double crystal Si(111) monochromator, and a harmonic-rejection mirror. The double crystal monochromator is used to monochromatize the synchronous radiation. The working principle of a monochromator is the Bragg's law

$$2d\sin\theta = \frac{h\nu}{E} = \frac{2\pi}{\sqrt{h^2 + k^2 + l^2}} \sin\theta \quad (3.7)$$

where hkl is the corresponding value plane index. Thus we can select the desired X-ray energy by changing θ .

The output X-ray from a monochromator is not truly monochromatic. Since the reflections from the (h_1, k_1, l_1) and (h_2, k_2, l_2) planes have the same Bragg angle in the fundamental (h, k, l) plane. These reflections are called harmonics. A harmonic-rejection mirror was used to eliminate these harmonics and its principle of operation given below. The refractive index for most materials in the X-ray region is slightly less than one. Total external reflection can occur when the incidence is below the critical angle. The critical angle can be expressed as

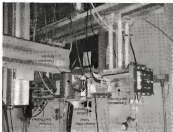
$$\theta_c = \sqrt{2} \sqrt{1 - n^2} \approx \frac{\lambda}{2} \quad (3.8)$$

where θ_0 is the X-ray energy, ρ_e is the electron density. The fundamental will be totally reflected while the harmonics will be absorbed by the mirror by setting the mirror angle between θ_0 of the fundamental and θ_1 of the harmonics.

3.3.3 Mirror detector

The most common way of measuring X-ray intensity in XAFS is by using a gas ionisation detector or an 'ion chamber'. The basic structure of an ion chamber is a pair of parallel metal plates. A certain type of gas, such as He, Ar, Ne or Kr, or a mixture of these gases fills the chamber. The choice of gas depends on the energy range of interest. A DC voltage is applied between the plates. The X-ray will ionise the gas molecules in the chamber. The ions (electrons) will transport to the negative (positive)-collecting plate generating a current in a closed circuit. Figure 7.4 shows a photograph of the experimental set up.

Figure 7-4 Photograph of the experimental setup for the 3-axis measurement of the advanced phase device in this study.



7.4 Composite Effects on the Local Structure of Colchite

The crystal structure of α -Colchite has been determined and refined by several authors. It belongs to $A^2B^{20}C^{12}$ family with the chalcogen (E1) structure (space group $I432$), with Ca in site 4a at $(\frac{1}{2}, 0, \frac{1}{2})$, In in site 4b at $(\frac{1}{2}, 0, 1/2)$, and Sn in site 16c at $(\frac{1}{2}, 0, \frac{1}{2})$ [Sp 74]. It's a ternary compound of the Grimes-Schomfeld compounds, which are characterized by tetrahedral bonding. Each atom C is coordinated by two A and two B atoms, whereas each atom is tetrahedrally coordinated by four atoms C. The atom C usually adopts an equilateral geometry closer to one pair of atoms than to the other, $R_{2A} < R_{2B}$ (dist. differences). The nearest neighbor bond lengths for a perfect crystal can be derived from the structural parameters and given by

$$R_{2A} = (x^2 + (1 + q^2)/4)^{1/2} a \quad (7.11)$$

$$R_{2B} = ((x - \frac{1}{2})^2 + (1 + q^2)/4)^{1/2} a \quad (7.12)$$

$q = c/a$ (tetragonal deformation) is the ratio between the lattice parameters c and a . A schematic diagram of chalcogen Colchite unit cell is shown in Figure 7.5.

An interesting question was raised by recent studies by Miran *et al.* [Mir 98, Mir 99]. They reported that the atomic coordinates, after the CdTe and InTe unit-cell atomic distances, depend strongly on the Cd occupation number based on X-ray powder diffraction and Rietveld refinement. Using their results they suggested that the spread in reported energy gap value E_g in the literature could be due to the variation of the x values predicted by InTe and ZnTe's model [Ref 89]. A direct measurement of the band gap of these samples [Mir 98], however, show that there is no correlation between the

measured gap and the reported x values. In fact, for some samples R_p decreases as x increases, in contrast to the Jaffe and Zunger's model [34–36] in this work. Cu K-edge X-ray Absorption Fine Structure (XAFS) measurements were performed on $\text{Ca}_{1-x}\text{Fe}_x\text{O}_{3-\delta}$ crystals with different compositions close to the CaFeO_3 stoichiometry and $\text{Ca}_{0.95}\text{Fe}_{0.05}\text{O}_{3-\delta}$.

4.1 Equipment

The samples were prepared from powder CaO and Fe_2O_3 in boron nitride (BN) coated evacuated quartz ampoules. The BN coating was used to prevent copper deoxidation of the quartz at high temperature [36a, 37]. These mixtures were then slowly heated to the melting temperature of CaO then gradually cooled to 1700°C and were kept in the furnace at 1700°C for one week to ensure equilibration. One sample was then quenched in liquid nitrogen and another one is slowly cooled to room temperature. The steel sample was heated above the oxide dissociation temperature (2100°C) to 2600°C , and held there for a week then quenched in liquid nitrogen. Electron Probe Micro Analysis (EPMA) (JEOL Superprobe III with wavelength dispersive spectrometry) was performed to ensure the compositional uniformity within of the samples. Powder X-ray diffraction (XRD) was used to verify the formation of chalcopyrite CuFeS_2 and the absence of other phases. The XAFS specimens were prepared by grinding the polycrystalline material. The fine powder was uniformly spread over Scotch tape. The XAFS spectra were measured in the fluorescence mode at room temperature.

The samples were analyzed by ICP atomic emission spectrometry for the atomic ratios of Cu

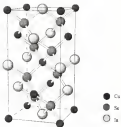


Figure 7.3 Schematic diagram of chalcopyrite structure for CuFeS₂

4.2 Results

The ICP analysis of dissolution of three Calcite_{0.99} samples shows that each sample has a different overall composition as given in Table 7.1 including sample II with nearly ideal 1:1 Ca:Ba₂ ratio. The estimated uncertainty for ICP analysis is ±0.5% relative.

Table 7.1 Chemical analysis of the investigated samples.

	Ca at. %	Ba at. %	Se at. %
Calcite _{0.99} I	33.4	23.8	42.6
Calcite _{0.99} II	34.1	25.3	40.4
Calcite _{0.99} III	33.2	23.1	43.8

The X-ray powder diffraction was used to verify the average long range order structure. The resulting spectra for all three Calcite_{0.99} (I, II, III) samples showed typical rhombohedral-Calcite_{0.99} powder XRD patterns [Mar 96].

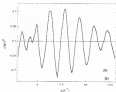
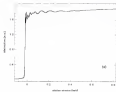
The three samples were taken to Argonne national laboratory and X-ray absorption spectra were taken using synchrotron radiation from the Advanced Photon Source. The XAFS data were analyzed by using the WinXAFS package [Bat 95]. The collected data was processed by standard methods [Joy 87]. The experimental accuracy data were first converted to an absorption coefficient based on $\mu_0(E) = 4\pi k^2 / E^2$. The Cu K-edge spectrum of Calcite_{0.99} sample-I is shown in Figure 7.1(a). The pre-edge background was then removed from the spectra. The next step was to convert the photon energy E to the photoelectron wave vector k along the relationship $k = \sqrt{2m(E - E_0)}/\hbar$ where m is the electron mass, E is the X-ray photon energy and E_0 is the K-edge energy

The normalized XAFS spectra were obtained by subtracting the background $\mu_0(k)$ from the measured absorption coefficient $\mu(k)$ and were normalized by the edge jump $\Delta\mu_0(k)$:

$$\chi(k) = \frac{\mu(k) - \mu_0(k)}{\Delta\mu_0(k)} \quad (7.12)$$

The resulting $\chi(k)$ oscillations shown in Figure 7.4(b) were then Fourier transformed into r -space with a k^2 weighting and a k -space range of 3–12 Å⁻¹. The Fourier transformed Cu-K edge r -space data are shown in Figure 7.4(c). To obtain the nearest neighbor information, data were inverse Fourier transformed with a r -space window range of 1.6 to 2.6 Å. The resulting first shell EXAFS are shown in Figure 7.4(d). The same k -space and r -space windows were applied to the data analysis.

Figure 7.7 shows the Cu-K edge r -space data for samples I and II. The first sharp peaks appear at about 2.1 Å and are due to Cu's first nearest neighbors (2a). The second broader peaks are at around 3.0 Å, and are produced by scattering from the second nearest neighbors (Cu-3a). It can be clearly seen the two spectra are almost identical. This indicates the local structure (i.e., the bond length, a_{1-2a} , and the number of nearest neighbors, N_{nearest}) of these two samples are nearly identical.



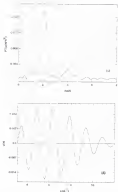


Figure 7.6 (a) Absorption as a function of photon energy at the Fe-K edge in Cygnus X-1 at 170 K. (b) Fe-K edge EXAFS oscillation $\Delta I/g(E)$ as a function of k after background removal. (c) Fourier transform of (b) to real space. The oscillation period is $3-2 \text{ \AA}^{-1}$. (d) Fourier filtered first shell EXAFS.

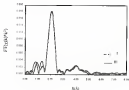


Figure 2.1 Dark edge (CCNPN) in real space transformed using a window $k \leq 3$ in \AA^{-1} for Catalase samples I and II

In Figure 7.4, the Fourier filtered EXAFS on the Cu-F edge for the first-neighbour peaks of samples 1, 11, 18 are shown. The first shell EXAFS from these three samples are identical. This indicates the first nearest neighbours around Cu atoms are identical in these three samples. To obtain quantitative information, the standard EXAFS equations (7-4) was used [Bey 87] as the least square analysis.

To fit the data to the equation, the structural parameters of chalcopyrite-CuSb₂ are needed for obtaining the backscattering amplitude, $F(k)$ and phase shift, $\phi(k)$, from the CuSb₂ EXAFS spectrum. A review of the reported structural data for chalcopyrite CuSb₂ is listed in Table 7.2. The agreement in cell parameters is good, but a considerable difference is observed in the reported lattice coordinates, $a(\text{Cu})$ and the resulting bond lengths, $d_{\text{Cu-Sb}}$ and $d_{\text{Cu-S}}$. The values from Spence et al. [Spn 74] $d_{\text{Cu-Sb}} = 2.424 \text{ \AA}$, and $d_{\text{Cu-S}} = 2.344 \text{ \AA}$ are accepted here for chalcopyrite-CuSb₂ structure.

Table 7.2 Structural parameters of CuSb₂ determined by X-ray diffraction

Type	$a(\text{\AA})$	$c(\text{\AA})$	$z(\text{Sb})$	$d_{\text{Cu-Sb}}(\text{\AA})$	$d_{\text{Cu-S}}(\text{\AA})$	Reference ^a
Single Crystal	5.752	11.426	0.233	2.424	2.344	[Spn 74]
Powder	5.764	11.436	0.234	2.424	2.344	[Spn 74]
	5.764	11.436	0.2348	2.423	2.343	[Sch 80]
	5.767	11.433	0.2337	2.420	2.343	
Single Crystal	5.760	11.4422	0.2340	2.4277	2.3463	[Kaw 82]
Powder ^b	5.7576	11.4472	0.2375	2.426	2.346	[Mn 84]
	5.7636	11.4360	0.2348	2.426	2.346	
Single Crystal	5.751	11.433	0.2377	2.4224	2.3441	[Pou 84]

^a $a(\text{Cu}) = 0.233$ for all cases.

^b $a(\text{Cu}) = 0.2375$ for all cases.

The backscattering amplitude $F_0(k)$ and phase shift $\phi(k)$ for Cu K-edge were obtained from sample (B) here using Cu-Se near-atomic distances equal to 2.424 Å. These functions were then used to calculate the Cu-Se near-atomic distances of sample I and II. The least-square fitting results are given in Table 7.3. The values of Cu-Se near-atomic distances are within 0.04 Å of each other.

Table 7.3 Least-square fitting results

	Coordination number	Cu-Se near-atomic distances Å
Calcd(I)	4	2.424 ± 0.002
Calcd(II)	4	2.425 ± 0.002
Calcd(B)	4	2.424

The samples examined in this study did not give evidence for a large density of Cu vacancies. The question whether the near-atomic distance is a function of the Cu occupancy number remains unanswered experimentally, even though a large density of Cu vacancies reported as (Miy 80) are questionable. This question, however, could be addressed by X-ray diffraction measurements on bulk samples such as Cu_2Se . The Cu_2Se compound lies on the $\text{CuSe-Fe}_2\text{Se}_3$ tie line. In general the structure of the compound belongs to defect mineral structures. They can be described as normal mineral structures with a certain fixed number of unoccupied atomic sites. The EXAFS data on this compound indicated that the Cu-Se and Se-Se near-atomic distances are the same as Calcd(I) even though 30% of Cu sites are vacant in this structure. The detailed EXAFS studies of Calcd(Se) are described in section 7.5.

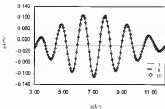


Figure 7.8 Fourier filtered EXAFS on the Cu K edge for the first neighbor peaks of three different monoisomeric Cu(II) samples (1, 2, 3).

7.1 Local Structure of Cu_2OSe_2

Considerable work has been carried out to determine the structure of the compound. A summary of the reported structure of the compound is given in Table 7.1. Polanski and Rysanowska [Pol 87] first reported the structure for Cu_2OSe_2 , and suggested the crystal structure is the space group of order 14 or $P4_3m$ based on the observed extinction rule from X-ray powder diffraction data. Later, a refined structure solution was given by Hsieh *et al.* [Hsie 88] using single crystal X-ray diffraction data. They determined the space group was $P4_3m$ and proposed the name P-chalcocopper for this phase. Tseng and Wen [Tse 90] proposed an ordered vacancy compound (OVC) structure model, with $P4$ symmetry, from their transmission electron diffraction results. The proposed structure model, however, has stoichiometry of Cu to Se is 1.5 rather than 1.33. Xiao *et al.* [Xia 94] studied epitaxial Cu_2OSe_2 thin films by transmission electron microscopy. They constructed a structure model by incorporating ordered point defects into the rhombohedral Cu_2OSe_2 structure to account for the extra diffraction spots. They further suggested Cu_2OSe_2 is an ordered defect rhombohedral structure. Hossain and Guha [Hos 95] also constructed a structure model for Cu_2OSe_2 from the same principle. Their model, however, is not an Ordered Vacancy Compound (OVC) although they referred to it as an OVC in the reference. Matsuda *et al.* [Mat 96] investigated the crystal structure of Cu_2OSe_2 by a combination of electron and X-ray diffraction. They found the space group is $P4$ or $P4_3m$ based on the observed extinction rule followed by powder X-ray data. They further determined the space group to be $P4_3m$ from a Convergent Beam Electron Diffraction

KTEM patterns along the [001] zone axis. They proposed a structural model $\text{AlGa}_{1-x}\text{Ga}_x$ for $\text{CuGa}_{1-x}\text{Ga}_x$, which is represented by $(\text{Cu}_x\text{Ga}_{1-x})_{\text{Ga}}(\text{Ga}_{1-x}\text{Al}_x)_{\text{Al}}$ (\square denotes anionic vacancy). They concluded that $\text{CuGa}_{1-x}\text{Ga}_x$ is similar to QVC, not a defect chalcopyrite structure.

Zhang *et al.* [Zha07-98] proposed an ordered vacancy compound structural model from first principle calculations. They followed two rules: (1) minimum Madelung energy and (2) minimum deviation from the cation rule. The model suggested the QVC is a complex distribution of three types of local tetrahedra around each Ga to minimize the deviation from the cation rule: $2\text{Cu}^+\text{Ga}$ (called I-^{\square}), $\text{V}_{\text{Ga}}\text{Cu}^+\text{Ga}$ (called I-^{\square}), and $\text{V}_{\text{Ga}}\text{Ga}$ (called I-^{\square}). The quantity k denotes the sum of the valence electrons from the 3d nearest neighbor cations. The I-^{\square} and I-^{\square} clusters must occur in equal numbers to ensure charge neutrality and likely results in each cation from neutral Coulomb structure. Chalcopyrite CuGaS_2 consists of 100% of the I-^{\square} clusters. $\text{CuGa}_{1-x}\text{Ga}_x$ has 20% of the I-^{\square} cluster and 40% each of the I-^{\square} and I-^{\square} clusters. They also suggested the formation of the defect pair $(2\text{V}_{\text{Ga}} + \text{In}_{\text{Ga}})$ satisfies the formation of an QVC.

Clearly the structure of $\text{CuGa}_{1-x}\text{Ga}_x$ needs further investigation. The disagreement among these structural models stems from the sensitivity of the different characterization techniques. The two questions in single crystal X-ray structure determination are whether a true single crystal was used and the limitation in unique determination of the space group. Transmission Electron Microscopy is capable of selecting a single crystal for study. The identity check, however, is not easy to obtain. Although the observed Selected Area Electron Diffraction (SAED) pattern in their TEM complex [Tsu 03][Xu 04] can be explained qualitatively by their proposed ordered vacancy structural model, their structure

model is not unique to the observed XRD patterns and the intensity data were not used quantitatively. “Does the vacancy in Cu_2S order?” is still an open area for research. In this work, the X-ray absorption Fine Structure (XAFS) measurements were performed on the Cu $L_{2,3}$ and S K -edges to study the local structure of Cu_2S . The first-principles total energy calculated results are compared and discussed.

Table 7.1 Reported structure data for Cu_2S .

Crystallographic Data	Structure Determination Method	QTC ^a	Reference
$P4_3$ at $\lambda = 1.5426$ and 1.79 \AA , $a = 0.39 \text{ \AA}$	Powder XRD	-	[Pol 66]
$P4_3$ at and 1.79 \AA , $a = 0.39 \text{ \AA}$	Single crystal XRD Full matrix structure refinement	No	[Shu 93]
$C4$	SAD ^b	Yes	[Ter 89]
	SAD ^b	Yes	[Zou 94]
Trigonal ^c	Powder XRD	No	[Sato 96]
$P4_3$ at and 1.79 \AA , $a = 0.39 \text{ \AA}$	Powder XRD, SAb, CRD ^d	No	[Shu 97]

7.5.1 Experiments

7.5.1.1 Sample Preparation and Characterization

The samples were prepared from powder Cu_2S and Ag_2S in boron nitride (BN) crucible enclosed quartz ampoules. The BN coating was used to prevent copper dissolution of the quartz at high temperature [Shu 93]. These crucibles were first slowly heated to the melting temperature then gradually cooled to 100°C , and were kept at 100°C for a week to ensure equilibrium then quenched in liquid nitrogen. Powder X-ray Diffraction (XRD) and Wavelength Dispersive X-ray Spectroscopy (WDS)

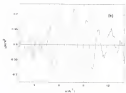
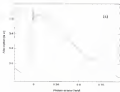
were used to verify the formation of desired homogeneous single-phase material. The XAFS specimens were prepared by grinding the polycrystalline material then spread the particles uniformly over Scotch tape.

7.5.1.2 XAFS Measurements

The XAFS measurements were performed on the Materials Research Collaborative Access Team (MRCAT) beamline of the Advanced Photon Source at Argonne National Laboratory. The beamline optics incorporate a Si(111) double crystal monochromator and a harmonic-rejection mirror to minimize the higher order harmonic content in the X-ray beam. The X-ray intensities were measured using ionization chambers. The XAFS spectra were measured in the transmission mode.

7.5.2 Data Analysis

The XAFS data was processed in the standard procedures as described in section 7.4.2. The backscattering amplitude $F_L(k)$ and phase shift $\chi(k)$ for Cu and Fe K-edge were extracted from the Caltech spectra using the known reference data. The ab initio multiple-scattering code FEFF [46, 52] was used to calculate $F_L(k)$, $\chi(k)$ and $\chi_L(k)$ for Fe K-edge data analysis.



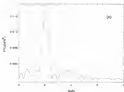


Figure 7.9 (a) Absorption as a function of photon energy at the Cu-K edge in Cu_2S_3 at 295 K. (b) Cu-K edge EXAFS oscillations, $k^2\chi(k)$, as a function of k after background removal. (c) Fourier transform of (b) to real space. The transform window is 3 to 12 \AA^{-1} .

7.5.2 Results

7.5.2.1 Crystal structure

The Cu K-edge EXAFS spectra and FT-R space data for Cu_2S_3 are shown in Figure 7.9. The first FT peak appears at about 2.1 \AA is due to the first nearest neighbors. (b). The second Fourier peak around 3.3 \AA seems then correspond with second nearest neighbors (Cu). (c). The isolated first shell species for Cu_2S_3 and Cu_3S_4 are given as

Figure 7.11. It can be clearly seen that the two spectra are almost identical except the one for Cu₂SiO₃ has a slightly larger damping coefficient. This indicates the local structure (i.e. the bond length, R_{Cu-O} , and the number of nearest neighbors, N) around the Cu atoms in these two semiconductor alloys are nearly the same. To obtain quantitative data a least-squares fit to the standard EXAFS equation was performed.

The least squares fit of the k^2 -weighted data at 298 K are shown in Figure 7.12. The backscattering amplitude, $f(k)$, and phase shift, $\phi(k)$, for Cu K -edge were estimated from the Cu₂SiO₃ spectrum using a Cu-Be interatomic distance equal to 2.04 Å. The obtained structural parameters are given in Table 7.4. The fitting results confirmed that the Cu-Be interatomic distance is consistent between Cu₂SiO₃ and Cu₂GeO₃. The nearest neighbor coordination number for Cu is fixed at 4 for the least square fitting in both phases. A schematic drawing of the Cu first nearest neighbor local structure is given in Figure 7.13.

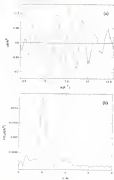


Figure 7: (a) 0.250 Å XMM spectra, and (b) magnitude of the Fourier transform for Catalog₂.

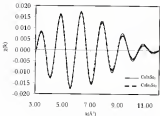


Figure 7-11 Fourier filtered EXAFS oscillations for the Ca K-edge for the first shell peaks in CaSi_2O_6 and CaSi_2O_7 .

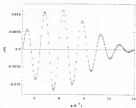


Figure 7.11: Least-square fit to the Fourier-filtered first shell Cu *K*-edge *k*-weighted EXAFS data of Cu₂O. (The data for Cu₂O and reference Cu₂O were filtered over an identical range as Figure 6, from 1.50 to 2.50 Å.)



Table 7.4: EXAFS analysis results

N	χ^2/ν
$R_{\text{Cu-O}}(\text{\AA})$	2.424 ± 0.004
$\sigma^2(\text{\AA}^2)$	$(1.46 \pm 0.01) \times 10^{-3}$

Figure 7.12: A ball-and-stick drawing of the Cu first nearest neighbor local structure.

3.1.2 Initial structure

The In-K edge FT-R spectra data for CuIn_2S_4 are given in Figure 7.14. The first FT-peak occurs at 2.15 \AA and is attributed to the first nearest neighbors (In). The selected first shell spectra for CuIn_2S_4 and Cu_2InS_4 are given in Figure 7.15. It can be clearly seen that the two spectra are almost identical. This indicates the first nearest neighbor environment (i.e. bond length, $R_{\text{In-S}}$, and number of nearest neighbors, N_1) around In atoms in these two semiconductor alloys are identical. The backscattering amplitude, $F_1(R)$, and phase shift, $\delta(R)$, required for the analysis of the In-K edge CuIn_2S_4 spectrum were extracted from the In-K edge CuIn_2S_4 EXAFS spectrum.

The least square fits of the k^2 -weighted data at 298 K are shown in Figure 7.16. The extracted structural parameters are given in Table 7.1. The fitting results confirmed that the In-In bond nearest distance is conserved between CuIn_2S_4 and Cu_2InS_4 . The nearest neighbor coordination number is fixed at 4 for the least square fitting. A schematic drawing of the In first-nearest neighbor local structure is given in Figure 7.17.

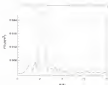


Figure 7.14 Magnitude of the Fourier transform of the Ls-K-edge EXAFS, $|F_L(k)|$ for Cu_2O_{5n} .

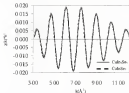


Figure 7.15 Power filtered EXAFS on the Ls-K-edge for the first shell peaks in Cu_2O_{5n} and Cu_2O_{5n} .

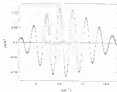


Figure 7.17 Local square fit to the Fourier-Bessel fit, used to K -edge k^2 -weighted $g(k)$ data of $\text{Cu}_2\text{S}_2\text{O}_6$. The data for $\text{Cu}_2\text{S}_2\text{O}_6$ and reference $\text{Cu}_2\text{S}_2\text{O}_6$ were fitted over an identical range ± 0.1 Å, from 1.7 to 2.7 Å.



Table 7.1 EXAFS analysis results

N	$R \pm 0.1$
$R_{\text{fit}} (\text{\AA})$	2.399 ± 0.001
$\Delta R^2 (\text{\AA}^2)$	$1.40 \times 10^{-4} \pm 0.10 \times 10^{-4}$

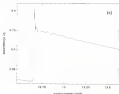
Figure 7.18 A schematic drawing of the first nearest-neighbor local structure

7.3.3 Se local structure

The Se-K edge core X-ray absorption data, $F(k)/k$ spectra, and FT-EXAFS spectra for Colclough, are shown in Figure 7.18. Unlike the Cu-K edge data, the first peak shows multiple-scattering because the first shell consists of both Cu and Se atoms. The Se-coordination number of chalcogenite Colclough is given in Figure 7.23(a), which consists of two Cu and two Se atoms around the central Se atom. Colclough belongs to defect-wierzbickite structure [Par 14], which can be described as normal wierzbickite structure with 10% vacancies substituted sites. The first shell Se-K edge EXAFS data should reveal the number of nearest neighbors in the case of Cu, by $\Delta = 1/3 \pm 1/6$. If Colclough did belong to defect-wierzbickite structural family.

The selected first shell spectra for Colclough and Colclough, are given in Figure 7.19. It is clear that the two spectra are very different. This indicates the first nearest neighbor environment around Se atoms in these two semiconductor alloys is different. The ab-initio multiple-scattering code FEFF7 [Rea 97] was used to calculate $F(k)/k$ and $k(k)$ in order quantitative estimates of the number of nearest neighbors and their distances. The selected first shell spectrum for Colclough and the least squares fit are given in Figure 7.20. The fitting was performed by assuming the number of nearest neighbors (NN), Cu-0, 1 or 2, and their distances d_{Cu-Se} 1.404 Å, and d_{Se-Se} 1.198 Å. Fitted results showed the Se-K edge data are consistent with the Cu and Se K edge. The resulting reduction factor S_0 was obtained and used in the analysis of Se K-edge spectrum for Colclough. The fitting

was performed using $N(E) \approx 0.8$, $N(E) \approx 0.4$, $d_{\text{CaO}} = 2.424$ Å, $d_{\text{FeO}} = 2.195$ Å. The FT-Raman first shell spectrum for $\text{CaCuSi}_2\text{F}_6$ with the best least square fit is shown in Figure 7.12. The fitting results confirm that $\text{CaCuSi}_2\text{F}_6$ does belong to defect-ordered structure which is characterized by a vacant tetrahedral site in the Fe ordered sublattice. The data are consistent with the idea proposed by [22a, 24], which suggested that the structure of $\text{CaCuSi}_2\text{F}_6$ consists of three types of local tetrahedral cationic clusters around each Fe : $\square\text{-Ca+2Si}$ ($q=3$), 2Ca+2Si ($q=4$), and $\square\text{-2Si}$ ($q=5$). \square denotes a vacancy and q denotes the sum of the cation valence electrons. A schematic drawing of these local structure models is given in Figure 7.12. How these different types of tetrahedra arrange themselves and form the long-range order structure (e.g., symmetry)-need further study by other techniques.



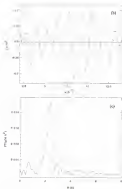


Figure 7: (a) H&K index for CoRoT-5, (a) raw H&K data, (b) $\hat{H}_k(t)$ Fourier coefficients, and (c) magnitudes of the Fourier coefficients.

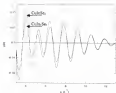


Figure 7: 19 Fourier filtered ESWAP on the line K edge for the first shell points in CylGr50 and CylGr50s

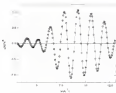


Figure 7.20: Least-square fit to the Fourier-filtered first shell Se-K edge E^2 -weighted $g(r)$ data of CdTe.

Table 7.4: EXAFS analysis results for CdTe Se-K edge data

R_F^2	0.750
$R_{\text{Se}} - C_{\text{Se}}$	
N	2
$R_{\text{Se}}(R_F^2)$	2.428
$\sigma^2(R_F^2)$	4.39×10^{-3}
$R_{\text{Se}} - I_{\text{Se}}$	
N	2
$R_{\text{Se}}(R_F^2)$	2.278
$\sigma^2(R_F^2)$	4.26×10^{-3}

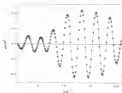


Figure 7.21 Least-square fit to the Fourier-filtered first shell Se-K edge k' -weighted $x(k)$ data of CuSe/Se.

Table 7.7 EXAFS analysis results for
CuSe/Se, Se-K edge data

R_i	4.112
Se - Cu	
N	1.9
$R_{\text{red}}(\%)$	2.434
$\sigma^2(\text{\AA}^2)$	1.75×10^{-3}
Se - Se	
N	2.4
$R_{\text{red}}(\%)$	2.596
$\sigma^2(\text{\AA}^2)$	4.22×10^{-3}



Figure 7.21 Schematic drawing of the three types of local symmetrical cationic cluster around each Sn: (a) $3D_{n+2}Sn$ ($n=0$), (b) $D+2Sn+2Sn$ ($n=7$) and (c) $D+3Sn+3Sn$.

To further investigate this problem, a collaborative research effort was established with the solid state theory group at the National Renewable Energy Laboratory (NREL). The group at NREL has calculated the Cu, Se and In-Se bond lengths in monochalcogen Chalcides, and Cu-pyrite Chalcides, and Cu-chalcogen ordered vacancy compounds using first-principles self-consistent electronic structure method. The total energy calculation was performed using the local density approximation (LDA) [Cap 11] as implemented by the general gradient boosted augmented plane wave (LAPW) method [Wu 85].

The calculated lattice constants $a = 3.768$ Å, $c = 1.008$ and $x = 0.217$ for chalcopyrite CuChalc₂ are in good agreement with the experimental values of $a = 3.764$ Å, $c = 1.008$ and $x = 0.218$ [Sjö, 74]. To determine the total energy, our calculation considers only structures that have minimal deviations from the stoichiometry ($x = 0$) since structures far from stoichiometry (x) of the valence electrons of the four cations (including the possibility of a vacancy V) that surround each Se atom should be close to 1. For Chalcides, only 1×1 clusters exist, that is each Se is surrounded by 3Cu + 2In. Some of the crystal structures that satisfy this condition are shown in Figure 7.23. These recent study [Wu 98] show that unlike 1×1 structures can be described as non-Martinite-like polytypes (i.e. they can be obtained by shifting part of the (001) planes of the chalcopyrite (CW) structure (Figure 7.23(a)) along the $[110]$ direction by $\pm \frac{1}{4}(\frac{1}{2})^2$ Se. For example, the CuSe structure (Figure 7.23(b)) with $x = 0$ in the $[110]$ direction can be obtained from the chalcopyrite structure by periodically shifting two out of every four planes, while the pyrite chalcopyrite structure (Figure 7.23(c)) can be obtained by shift periodically one

out of every four planes, etc. Notice that the shift along the $[110]$ direction by $\tau = c_0/4$ (Fig. 2.16) is equivalent to the permutation of all the Cu sites with all the Fe atoms in that plane. For Coludite, the most restrictive requirement demands that only an equal number of Fe^{2+} ($\text{Fe}^{2+} + \text{Cu} = 2\text{Fe}$) and Fe^{3+} ($\text{Fe}^{3+} + 3\text{Fe}^{2+}$) Fe -octahedral clusters can exist. These structures can be obtained from Coludite, in Figure 2.13, by having one $(2\text{Fe}_{\text{Fe}} + 3\text{Fe}_{\text{Cu}})$ cluster pair in every FeO_{10} (4 Coludite) unit cell [Jia 99]. For Coludite, it can be viewed as a mixture of Coludite and Coludite, i.e., they contain 50% of the $k = 0$ clusters and 40% each of the $k = 2$ and $k = 4$ clusters.

The NEEL group 1 calculations show that the unachieved Coludite, the chalcopyrite structure (Figure 2.13(c)) has the lowest energy, in agreement with experiment [Pd 87]. Thus chalcopyrite is the ground state structure for Coludite. The calculations also show that for all the $k = 0$ polytypes the total energy difference between any of the two polytype structures is very small, less than 2 mRy/atom. This result indicates that although the $k=0$ local maximum is well conserved below the order-disorder transition temperature ($T_c = 1045$ K) [Pd 87], the long range chalcopyrite ordering is not perfect at finite temperatures [Wu 99]. Many of the chalcopyrite [001] layers are shifted along the $[110]$ direction where Cu occupies the normally Fe site and vice versa. The actual degree of the long-range chalcopyrite order of Coludite may depend sensitively on the growth kinetics, history of annealing, and the stoichiometrical composition. Indeed, the coexistence of chalcopyrite and Cu-Fe-blue phases in Coludite has been reported [Jia 99]. The imperfections of long range chalcopyrite ordering will have large effect on the XRD analysis of the crystal structure (see below). Although Cu-Fe-like phases had not been reported in Coludite, The observed diffuse scattering in the electron diffraction

studies of CuAlSi₂ by Mandilova and Ljapčević [Mia 81] and Kelly et al. [Kel 81] clearly show the dominance of the long range order and a strong tendency for short range ordering.

This result is consistent with the classical work of McKinnon and Broyer [Mia 81] and previous theoretical work on semiconductor alloys [Mia 84] which shows that bond lengths in semiconductor alloys are more close to their ideal values than to the alloy averaged values. It is also consistent with the fact that bond length conservation is more complete for alloys with large ionic character (e.g., III-V alloys and CuAlSi₂) than for more covalent compounds (e.g., III-V alloys) since the bond breaking force is much weaker for ionic alloys [Mia 84].

Unlike a full scale order-disorder transition, which can lead to a change of band gap by as much as 0.33 eV [We 66], the formation of polycrystalline leads to only small changes in the band gap, less than 0.03 eV [We 66]. The band gap in the defect tetrahedral compounds is larger than the band gap for CuAlSi₂ [We 66, 68b, 68c]. The reason for this is as follows: In the defect tetrahedral compounds some of the Cu atoms are replaced by Ca vacancies V_{Cu} and Si₃ atoms, thus the coupling between Si₃p and Cu s/p_{3/2} reduced versus defect tetrahedral compounds as compared to CuAlSi₂. This weaker p-s_{3/2} repulsion lowers the Valence Band Intermixing (VBI) of the ordered vacancy compounds and increases their band gaps.

Both XRDPS and first principle calculations results show that the first-nearest-neighbor bond structure (i.e. the bond length, $d_{\text{Si-Si}}$, and the number of nearest neighbors, N) around Ca atoms in CuAlSi₂ is not a function of stoichiometry nor a vacancy. This is contrary to the conclusions of Hensen et al. [Het 84] from X-ray powder

diffraction (XRD) and Rietveld refinement. The reason behind this discrepancy is found in the differences between these two characterization techniques. XRD is not suitable for determining individual bond length when two different type of atoms share the same crystallographic site. On the other hand, EXAFS is capable of measuring bond structure toward specific type of atoms, including the bond lengths.

It is believed that the large dependence of the Cu-Fe and Fe-Fe bond lengths on Cu occupancy number reported in [Már 94] is an artifact of the fitting procedures. Part of the difficulty is related to the determination of Cu-Cu occupancy number. [Már 94] used three schemes were used in the Rietveld refinement process. In the first scheme, the Fe content is fixed at 2, the Fe content at 1, and the Cu content was refined. In the second, only Fe is fixed at 2, the Fe is as observed by EXAFS, and the Cu is refined. In the third, both Fe and Fe are fixed EXAFS and the Cu is refined. The three different schemes yielded similar Cu occupancy number, despite the 3.33% difference between the Fe content in scheme 1 and scheme 2. This observation indicates that the refinement is not very sensitive to the occupancy number. For example, it would be interesting to see how much the fit factor changes if one fixed the Cu content using the EXAFS data. Another interesting scheme is allowing all three occupancy numbers to vary in the refinement.

Second, as shown by Joff and Zunger [Joff 93] and more recently Wu *et al.* [Wu 94], large change in $a(b)$, and thus, the Cu-Fe and Fe-Fe bond lengths, will lead to a large change in the bond gap. A change from 0.224 to 0.226 in $a(b)$ is expected to cause an increase of bond gap by 0.123 eV [Wu 94]. This large bond gap increase is not supported by the measurement of Mészáros *et al.* [Már 94] for the same samples. In fact, some of the samples with large dot val of Fe actually have smaller bond gaps.

It is likely that the samples used in the measurements by Minami *et al.* show some degree of partial disordering of Cs and is consistent with the formation of CaSiO_3 polymorphs in short range order. By assuming the samples have perfect chalcopyrite ordering in their Rietveld analysis, some of the h-k-l bands is treated as CaSi bands and vice versa. This will overestimate the smaller CaSi band and underestimate the longer h-k-l band thus give a false impression that αSi increases. The fact that formation of CaSiO_3 polymorphs in the samples is also consistent with the observed small band gap changes in the samples and the fact that sample (B) which has "largest" αSi actually has smaller band gap.

In addition to the two reasons stated above, another source of complication could come from formation of the CaSi -phase in the samples, especially for the Curvish samples used in [Min 94]. It is well known that the powder XRD patterns for CaSi and CaSiO_3 are not easy to resolve if a mixed phase was examined. Simulated powder XRD patterns for a single-phase chalcopyrite CaSiO_3 and a mixed phase (10% CaSi and 90% CaSiO_3) are shown in Figure 1.26(a) and (b) respectively. The only difference is a small change in the relative peak intensity and slight shift in peak position. These changes can not be easily distinguished from the preferred orientation effect and lattice parameter variations.

Crystal structure of CuInSe_2

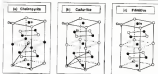


Figure 1.23 Crystal structures of CuInSe_2 in (a) chalcopyrite, (b) C_{2h}^8 -like, and (c) primitive phases. For clarity the Se atoms are not shown. The lines with arrows give the primitive and cell lattice vectors for these structures.

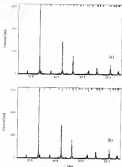


Figure 7.24 (a) Calculated Cu-K α powder XRD pattern for cholesteric Cu $_2$ S $_x$ structure [Fig. 7c] (b) Calculated Cu-K α powder XRD pattern for a mixed cholesteric Cu $_2$ S $_x$ and Cu $_2$ Se [Fig. 7d] sample (10 % Cu $_2$ Se and 90% Cu $_2$ S $_x$). DEWYS [Fou 11] program was used for the simulation.

[Mir 94, 96] extended their results to explain the spread in the energy gap values reported in the literature based on Jaffe and Langner's model [Jaf 84]. Jaffe [94, 96] compared their experimental dE_{gap}/dx and dE_{gap}/dx values with those derived from [Mir 94] and had good agreement between them. However, the value of dE_{gap}/dx and dE_{gap}/dx can be directly derived from the structural model and given as

$$dE_{\text{gap}}/dx = \frac{d}{dx} \left(x^2 + (1 + g^2)/4 \right)^{1/2} x \quad (7.14)$$

$$dE_{\text{gap}}/dx = \frac{d}{dx} \left(x + \frac{1}{2} \left(x^2 + (1 + g^2)/4 \right)^{1/2} \right) x \quad (7.15)$$

A plot of dE_{gap}/dx and dE_{gap}/dx vs. x [94] is given in Figure 7.24. The agreement between the values of dE_{gap}/dx and dE_{gap}/dx in [Mir 96] and [Jaf 84] are a direct consequence of using the same structural model. It would not be used as a measure of how well the experimental data agree with the theoretical calculations.

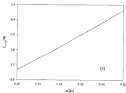
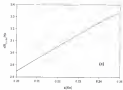


Figure 7.25 (a) dM_{n-1}/dk and (b) dM_{n-1}/dk vs. $\alpha(k)$ ($n=7$, $T_0 = 1$, $\beta_0 = 0.05$).

1.1 Condensates

XAFS experiments were performed to study the local structure of various copper indium selenide semiconductor alloys.

Fluorescence Cu K-edge X-ray Absorption Fine Structure (XAFS) measurements were performed on $\text{CuIn}_{1-x}\text{Se}_x$ crystals with different compositions close to the stoichiometric CuInSe_2 . The result indicates the local structure (i.e. bond length, $d_{\text{Cu-Se}}$, and number of nearest neighbors, N) around Cu atoms in these semiconductor alloys are the same. Contrary to other X-ray powder diffraction (XRD) and Raman scattering work which suggested the Cu-Se and In-Se bond length values depend strongly on Cu occupancy number, these studies indicate the environment around Cu is not affected by small changes in chemical composition. Total energy calculations were also performed, and show that the Cu-Se bond length is independent of the Cu occupancy number while In-Se bond length decreases only slightly when the Cu occupancy decreases. The calculations also suggested the formation of other polypyr structures in CuInSe_2 , in addition to the chalcopyrite structure. It is likely the samples used in the measurements by [Jin 96] showed some degree of partial disordering of Cu and In cations or the formation CuInSe_2 /polypyr in their sample.

A detailed EXAFS study of CuInSe_2 and $\text{CuIn}_{0.9}\text{Se}_{1.1}$ on Cu-K, In-K, and Se-K edges was performed. It was found the Cu and In first nearest neighbor local structures in $\text{CuIn}_{0.9}\text{Se}_{1.1}$ are almost identical to those in CuInSe_2 . The In first nearest neighbor local structure, however, is quite different. The least square fitting of Se-K edge EXAFS spectra indicated $\text{CuIn}_{0.9}\text{Se}_{1.1}$ consists of Se-coordinated coordination with average 2 Cu and 1 In as nearest neighbors. On the other hand, CuInSe_2 consists of Se-coordinated coordination

with average 14.4 Do and 2.4 fa as nearest neighbors. This result directly proved $\text{C}_{\text{duty}}/\text{C}_{\text{fa}}$ is indeed a direct structural measure.

CHAPTER 8 CONCLUSIONS AND FUTURE WORK

This dissertation has focused on developing a detailed thermodynamic description of the Ca-In-Sr system for better understanding of the processing chemistry of Ca-based intermetallic layers. Knowledge of thermodynamics and phase diagrams was applied to various engineering of the power-cycle modules for RTP systems of Ca-based intermetallic layers. Another focus of this work was a detailed study of the local structure of copper within silicide semiconductor alloys by EXAFS.

8.1 Conclusions

8.1.1 Thermodynamics and phase diagrams assessment

In Chapter 3, the assessment of the thermodynamic properties of elemental $\text{Sn}_2(\text{g})$, In(gas) , Sn(l) , and $\text{Sn}_2(\text{l})$ ($n=1$ to 3) resulted in suggested values of $\Delta H_{\text{f,298.15}}^\circ$, $T_{\text{m,eq}}^\circ$, and $C_p(T)$. The thermodynamic functions of each gas phase species was assessed from the available literature data or calculated from molecular constants assuming harmonic oscillator, rigid rotor, and ideal gas behavior. The values of $\Delta H_{\text{f,298.15}}^\circ$ for $\text{Sn}_2(\text{g})$ and $\text{Sn}_3(\text{g})$ were optimized using the vapor pressure data in equilibrium with Sn(l) and Sn_2 , In(gas) , respectively. The phase considerations were taken into account by using the Peng-Robinson equation of state. The results of this assessment are expressed for the Gibbs energy of each of the six species Sn_2 , In(gas) , Sn(l) , and $\text{Sn}_3(\text{g})$ ($n=1$ to 3) as a function of temperature. These expressions were then used to calculate

equilibrium in the Se system. The vapor pressures obtained from equilibrium calculations agree well with the experimental results. The equilibrium calculations showed that the predominant vapor species at a temperature above approximately 1000 K is the dimer while at a lower temperature (~ 600 to 1000 K) Se_2 is the dominant species. Below 600 K the major species is $\text{Se}_2(\text{g})$. During growth using a Se evaporation source, a change in the deposition chemistry is expected as the temperature is changed through one of these transitions. The results were used to estimate the Langmuir evaporation flux for each species and is useful in characterizing the performance of an evaporation source.

In Chapter 4, a complete database for the Cu-Se system was assembled and a model assessment was performed. A self-consistent set of phase diagrams and thermodynamic data was selected. The selected database was combined with the unary data for copper provided by NIST, and the assessed Se data in Chapter 3. The association model was used to describe the liquid phase. A first-sublattice compound energy formalism was used for the Cu_{1-x}Se phase. The Redlich-Kister polynomial was used to represent the Gibbs energy of the terminal solid solution $\text{Se}(\text{Cu})$. The remaining metastable solid phases (Cu_2Se , CuSe , CuSe_2) were modeled as line compounds.

The phase diagrams and thermodynamic properties of the system have been calculated using the optimized parameters. The calculated phase diagrams agree well with the data used in the optimization. In the calculated phase diagrams, the temperatures and compositions of the Se-rich liquid miscibility gap have been predicted. The site fractions of vacancy in the $\beta\text{-Cu}_{1-x}\text{Se}$ phase were calculated. In the $\beta\text{-Cu}_{1-x}\text{Se}$ single-phase region, the Cu vacancy concentration in the first sublattice, x_{Cu}^{I} , increases with an increase of selenium concentration, whereas the Se vacancy concentration, x_{Se}^{I} , decreases with an

increase in the selenium concentration. The calculated Cu vacancy concentration in the first calculation is between 0.008 to 0.01% , whereas the β -se vacancy site fraction is between 2.87×10^{-12} to 2.23×10^{-8} .

The calculated enthalpies of formation in the present work are between the ones measured by [Gai 36] and those evaluated by [old 74]. The calculated standard entropies agree well those evaluated by [old 74] except that of CuSe_2 , which lies in between the value of [New 70] and that evaluated by [old 74]. The calculated heat capacity values agree well with the measured ones [Ref 33]. The transition of $\alpha\text{-CuSe}$ to $\beta\text{-CuSe}$ is assumed to occur at 176 K with an enthalpy change of 8930 J/mole, which is in good agreement with that measured by [Ref 33]. The calculated entropy of the transition of $\alpha\text{-CuSe}$ to $\beta\text{-CuSe}$ at 176 K is 1.28 J/mole, which is in good agreement with that measured by [Ref 66]. As no experimental heat capacity data for CuSe are available, those data were generated from the phase diagram data after assuming that the heat capacities of $\alpha\text{-CuSe}$ and $\beta\text{-CuSe}$ are identical.

In a similar fashion, a complete database for the In-Se system was assembled and presented in Chapter 5. The phase diagrams and thermochimistry of the In-Se system has been experimentally studied by several authors and the results for selected properties are summarized. Early studies reported four intermediate compounds (In_2Se_3 , InSe , In_2Se_5 , and In_3Se_4), while InSe and In_2Se_5 were identified as congruent melting compounds. A miscibility gap on the In-rich side was also suggested. Later work reported the existence of the four compounds In_2Se_3 (instead of In_2Se_5), InSe , In_2Se_5 (instead of In_3Se_4) and In_3Se_4 , with only In_2Se_5 melting congruently. More recent work by [Gao 98] reported In_2Se_3 and In_3Se_4 as stable phases and $\beta\text{-In}_2\text{Se}_5$ as stable at 59 ± 1 K at $x_{\text{Se}} = 0.74$ as contrary to

present study. A self-consistent set of phase diagrams and thermochemical data was inferred. The inferred database was compared with the survey data for values provided by AGTE and the assessed $\Delta_f H^\circ_{298.15}$ data presented in Chapter 3. Nine intermetallic solid phases (In_2Sn , InSn , In_3Sn , In_5Sn_2 , In_7Sn_3 , $\alpha\text{-In}_2\text{Sn}$, $\beta\text{-In}_2\text{Sn}$, $\gamma\text{-In}_2\text{Sn}$, and $\delta\text{-In}_2\text{Sn}$) were modeled as line compounds. The association model [Eqs. 81] was used to describe the liquid phase. Missing heat capacity (In_2Sn , In_5Sn_2) and entropy data (In_2Sn , In_5Sn_2) were first assessed by Uni- α [Koh 77] rule and Lennor's [Lar 75] rule, respectively, and a re-estimation of the literature heat capacity and entropy data for $\alpha\text{-In}_2\text{Sn}$, $\beta\text{-In}_2\text{Sn}$, $\gamma\text{-In}_2\text{Sn}$, and $\delta\text{-In}_2\text{Sn}$ was then based on the new phase diagram. These data were then assessed through optimization using ThermoCalc.

It was found that the reported $-\Delta_f H^\circ_{298.15}$ value for In_2Sn [Jahn74, Cha 91] is too small to be consistent with the phase diagram data. Using the reported value In_2Sn disappears at a much lower temperature ($\sim 300\text{K}$) and does not reach the peritectic temperature (719K). By coupling the thermochemical and the phase diagram data, optimized G $_{\text{mix}}$ expressions for the solid compounds and the liquid phase are obtained together with the major vapor phase species (Sn , $\alpha\text{-Sn}$) in G $_{\text{Sn}}$, In , InSn , In_3Sn , In_5Sn_2) as In_2Sn system. The T-x and P-T projections of the P-T-x diagrams were calculated. The calculated P-T diagrams is in reasonable agreement with the reported data [Gib 73, Liu 87, Cha 91, Pan 93] and consistent with the recent T-x phase diagram [Cao 94]. It is also suggested that the experimental data of [Gib 73, Liu 87, Pan 93] represented the vapor pressure in equilibrium with the $\beta\text{-In}_2\text{Sn}$, $\delta\text{-In}_2\text{Sn}$ and liquid 2 and liquid 2' phase domains, rather than that in equilibrium with $\alpha\text{-In}_2\text{Sn}$, as the investigators presented.

5.1.2 Catalysts, thin film formation by RTP

In Chapter 4, knowledge of thermodynamics and phase diagram was applied to engineering of alternative reaction pathway for CDS thin films. A novel 3-layer precursor structure of a co-deposited In-Sn (95 to 15 Sn at %) top layer and a Cu₂Se (50 to 10 Se at %) bottom layer was proposed. It was postulated that this precursor structure should lead to CDS formation through a liquid-solid reaction in the processing temperature window 300°C to 400°C. Two precursor structures were deposited on a negatively-biased transparent substrate. The first structure is the three layered structure, In_{0.95}S_{0.05}/Cu₂Se_{0.50}/Cu₂Se. After RTP, it was found the precursor film underwent a liquid-solid reaction and formed large grained Catalyst films at a substrate temperature of 300°C, as suggested by SEM and XRD analysis. It was believed that the melting of top layer In_{0.95}S_{0.05} phase occur through a eutectic reaction. The second structure consists of only two alloy layers In_{0.95}S_{0.05}/Cu₂Se. This precursor structure lead to the formation of large grained CuS-(In)₂S films at a substrate temperature of 300°C, consistent with the pathway suggested by the phase diagram. It was found that the ramp rate has a dramatic effect on the film quality for the second structure. A slow ramp rate (1°C/s) resulted in bubble formation and de-lamination of the film. A higher ramp rate (10°C/s) produced Catalyst films with better repeatability and no bubble formation or de-lamination problems. It is believed that bubble formed by evaporation of In₂ vapor from the Cu₂Se layer. This is supported by RTP experiments on Cu₂Se reference film under the same conditions. The Cu₂Se film has a lower Se content and transformed to Cu₁₀Se. With In_{0.95}S_{0.05} layer on top, however, the overall Se content did not change significantly (~0.1%) according to the RTP

chemical analysis. The presence of the InAs layer provided a barrier to Sn interdiffusion in the film.

4.1.3 XAFS investigations of copper indium selenide semiconductor alloys

XAFS experiments were performed to study the local structure of various copper indium selenide semiconductor alloys.

Resonance Cu K-edge X-ray Absorption Fine Structure (EXAFS) measurements were performed on $\text{Cu}_{1-x}\text{In}_x\text{Se}$ crystals with different compositions close to the stoichiometry CuInSe_2 and Cu_2InSe_3 . The EXAFS data were analysed using the same range of k-window for Fourier transform and same R-window for Fourier filtering of the first shell EXAFS oscillations. The resulting first shell Cu, $k^3\chi(k)$ spectra from different stoichiometries were almost identical. This result indicates the local structures (i.e. bond length, $d_{\text{Cu-Se}}$, and number of nearest neighbours, N) around Cu atoms in these semiconductor alloys are the same. Contrary to other X-ray powder diffraction (XRD) and Rietveld refinement work, which suggested the Cu-Se and In-Se bond length values depend strongly on Cu occupation number, these studies indicate the environment around Cu is not affected by small changes in chemical composition.

Total energy calculations were also performed, and show that the Cu-Se bond length is independent of the Cu occupation number while In-Se bond lengths decrease only slightly when the Cu occupation decreases. The calculation also suggested the formation of other polytype structures $\alpha\text{-CuInSe}_2$, in addition to the chalcopyrite structure. It is likely the complex used in the measurement by [Mar 91] showed a degree of partial ordering of Cu and In cations in the formation CuInSe_2 polytype in the short range. The discrepancy between the results of the present work and that of [Mar 91] could be

explained by the different nature of the characterization techniques. XRD is not suitable for distinguishing individual local lengths when two different types of atoms share the same crystallographic site, while XAFS is capable of measuring local structure around specific types of atoms, including the bond lengths. The large dependence of the Cu-Se and In-Se bond lengths on Cu occupation number reported in the literature may be an artifact of the Rietz procedure used. A further implication of this result supports the existence of short-range order Cu₂Se₃ polytypes in Cu₂Se₃ thin film photovoltaics.

A direct EXAFS study of Cu₂Se₃ and Cu₂Se₂Se on Cu-L, In-L, and Se-L edges was performed. It was found that the Cu and In first nearest neighbor local structures in Cu₂Se₃ are almost identical to those in Cu₂Se₂Se. However, the Se first nearest neighbor local structures are quite different. The first-nearest fitting of the Se-L edge EXAFS spectra indicated Cu₂Se₃ consists of Se-centered tetrahedra with an average 2 Cu and 2 In nearest neighbors. On the other hand, Cu₂Se₂Se consists of Se-centered tetrahedra with an average of 1.8 Cu and 1.8 In as nearest neighbors. This result directly proves Cu₂Se₃ is ordered α -defect tetrahedral structure and is consistent with first-principle calculation [Chu 98]. The calculation suggests there are three types of local tetrahedral nearest clusters around each Se: V-Cu₂Se₂ ($\beta=7$), 2Cu-2In ($\beta=8$), and 2In-2Se ($\beta=9$), where β denotes the sum of nearest distances for nearest. Cu₂Se₃ consists of 100% $\beta=8$ clusters and Cu₂Se₂Se consists of 30% $\beta=8$ and 40% $\beta=7$ and 40% $\beta=9$ clusters.

5.2 Future work

5.2.1 Thermodynamic and phase diagram assessment

In this work, a crucial thermodynamic and phase diagram assessment of the Bi-Ge, Cu₂Bi, and Bi-Ge binary systems were completed. It is recommended to utilize this database for analysis of binary film calculations during the binary precursor deposition.

More experimental data are needed for the Cu₂Bi-In₂S₃ pseudo-binary system. It is recommended to perform experiments to determine the important phase boundaries and the mixing energy data such as the heat capacity data for most of the binary phases. A complete assessment of the Cu₂Bi-In₂S₃ binary system will be the next step after these critical data are available.

5.2.2 Cu₂Bi₂S₃ thin film formation by RTP

In this work, a novel precursor structure for RTP synthesis of Cu₂Bi₂S₃ film was proposed and subjected to RTP treatment. The experimental results showed the proposed precursor structure is extremely promising. Large grain CS films were produced without delamination problems in a very short time (<70 s). It is recommended to optimize the processing conditions based on the rate and performance by a DOE (Design of Experiments) methodology.

It is also recommended to study the effect of Bi. Preliminary results showed the In₂Bi₂S₃ formation is much more prominent when Bi is added to the precursor. The mechanism, however, is not clear.

5.2.3 XAFS investigations of copper valence relative to annealing steps

The XAFS results of this work suggest the coexistence of a polycrystalline structure in Cu₂Bi₂S₃ materials as evidence to disordered ordering. Increasingly ordered Cu₂Bi₂S₃

ordering CuInS_2 structure was produced at our laboratory [56a, 59] for the first time. A theoretical study of the origin of the polytypic or pleochroic device is recommended.

A detail study of the local structure of CuInS_2 was reported in this work. A complete structure model, however, is still needed. It is recommended to perform Convergent Beam Electron Diffraction (CBED) in combination with X-ray diffraction experiments to resolve the GVC issue.

REFERENCES

- [Abr 94] Abramson H. Kh. Buzikov V. P. Kuznetsov M. A. Demchenko G. K. & Taylor D. A. *Sov. Phys. Solid State* 24(10): 1678 (1984)
- [AJB 94] Allen D.R., Mawson G.D., Davis A., Turtel J., Mawson R. and Nisell K., *Solar Cells*, 34: 91 (1990)
- [And 37] Anderson C.T. *J. Amer. Chem. Soc.* 59: 1928 (1937)
- [And 90] Anderson T., Pasterkamp D., Pien S-G, Legros H., Chen W. A., Sakash-Peterson R., Berlin H.J. Chen Q., *Colloid* 21(2): 285 (1997)
- [Ask 93] Askaniyev A.L. and Rehr J.J. *Phys. Rev. B* 52: 2495 (1995)
- [Asa 95] Asano I., Sato M., Kubo H., Sandhu, B. in *Applications of Thermodynamics in the Synthesis and Processing of Minerals* (P. Nash and B. Sandhu, 1996.) *The Minerals, Metals & Materials Society* 211-223.
- [Asa 72] Asano J.O., Dandekar, G.A., Hovari, Z.M. *Heavy Metal* 1: 11 (1972)
- [Ask 54] Askarov E. A., Akov M.A., Azarov T. Kh., Akhmedov A. B. & Mordukhai E. M. *Tr. Akad. Nauk Azerb. SSR* 6: 117 (1954)
- [Asa 78] Asano T. and Yuzawa A. *Canadian Metallurgical Quarterly* 18: 111 (1978)
- [Ber 79] Belyayev A. A., Belyayeva T. A., Chernyya M. A. & Kabanikov V. T. *Russ. J. Inorg. Chem.* 24: 1211 (1979)
- [Bel 48] Belar E.H. *J. Chem. Soc. (London)* A: 669 (1948)
- [Ber 98] Berth G., Pasterov V., Savitski P. *High Temp. Sci.* 25: 171 (1988)

- [Bar 94] Baumgartner F.F., Regula M., and Bueker E. Proc. of the 12th EC Photovoltaic Solar Energy Conference, Amsterdam 415, 1994
- [Bar 95] Barkashtz, I. Chapiro W. A., J. Chem. Phys. 43 4329 1965
- [Bar 96] Barkashtz, I. Chapiro W. A., J. Chem. Phys. 48 2744, 1968
- [Bar 97] Baranovskii G. P. & Golov A. *Nucl. Separation* (1) 1 773 1968
- [Bar 98] Berger L., I. Barkashtz, S.B. Benlar, S. A. Malot'ka, A. G. Balasubrahany, A. E. Lohrler, Y.Y., *Int. Acad. Phys.* 1988, Hong Kong Mater. 3 373, 1988
- [Bar 99] Baranovskii G. P. Carson F., & Tuck R. *Period. Miner.* 41 391, 1973.
- [Bar 00] Baranov, W. Z. *Russ. Rev.* 3 1945
- [Ba 76] Blackwell R., Selzer G., J. Low-Cost Solar Module 57 24 1976
- [Bar 77] Barlow A., Lippman J. C. *J. Phys. Chem. Solids* 283 879 1973
- [Bar 85] Bartrick R.F., J. Chem. Phys., 84 3644, 1985
- [Br 47] Bragg P. *Exposition*, Techn. Hochschule Stuttgart 1947
- [Bar 74] Barlow B. P., Feltzow, B. N. & Stronitzman L. *Br., Russ. J. Inorg. Chem.* 19 1187 1974
- [Cap 88] Caporali D.M. and Miles B.J. *Phys. Rev. Lett.* 60 366 1988
- [Cha 76] Chang S.S. Enoki A.B. J. Chem. Thermodynamics, 8 323 1976
- [Cha 81] Chakraverty D. J., & Laughlin D. E., *Bulletin of Alloy Phase Diagrams* 2(4) 169, 1981
- [Cha 90] Chaudhri C. J. *Crystal Growth* 119 297 1993
- [Cha 97] Chang, C.H. Spaldrey B.J. Morneau A., Derylova A. and Anderson T.J. *Mater. Res. Soc. Symp. Proc.* Vol 445 463 1998
- [Cha 98] Chang C.H. Derylova A., Spaldrey B.J. and Anderson T.J. The Conference Report of the 22nd IEEE Photovoltaic Specialists Conference, Washington D.C. 448 1998
- [Cha 99] Chang, C.H. Derylova A. Spaldrey B.J. Anderson, T.F. to be published 1999

- [Cal 88] Cole R., *Detrend J. Trans. Faraday Soc.*, **44**, 2411, 1948
- [Cal 94] Calvez Y., Pleschak Ya., Solovnikov B., *J. Phys. Equilibria*, **17**, 404, 1990
- [Dae 91] Damsle B., Rasm M.-C., Tolness J. C., Vossler G. Z., *Makrid*, **1991**, 417, 1998
- [Dae 92] Davies B.H., Damsle A.T., Chan T.G., Berry T.I., Rasm M.H., *High Temp. Sci.*, **28**, 259, 1990
- [Dae 93] Damsle W., *J. Chem. Phys.*, **2075**, 1044, 1953
- [Dae 94] Damsle A. P., Koshenko V. I., Gorbunov Ya. B., Baryskaya V. A., Gusev S. V., *Int. Atom. Nucle. Sci. Ser.*, **11**, 2140, 1979
- [Dae 97] Dae R., *Kaplan und Kaplanologien in der Technik*, Springer, Berlin, 1997
- [Dae 98] Damsle H., Bunkar G., *Physical Review B*, **38**, 2407, 1988
- [Dae 99] Damsle A.T., *Cal/Phad*, **1543**, 317, 1991
- [Dae 00] Damsle L.E., *J. Am. Chem. Soc.*, **42**, 1379, 1920
- [Dae 04] Damsle J., Selmer B., Arnesen-Mathias A.M., Vossler, Tuo E., *Proceedings Third International Symposium on Industrial Use of Selenium and Tellurium (Oslo, Sweden)*, 223, 1989
- [Edw 91] Edwards J. G., *High Temp. Sci.*, **42**, 37, 1991
- [Eny 92] Eny J.-Y., Brillon-Grenier L., Heugnon C. and Chevy A., *J. Appl. Phys.*, **71**, 3156, 1992
- [Foa 90] Foa S.I., *J. Appl. Phys.*, **68**(6), 2114, 1990
- [Foa 94] Foa S.I., *MRS Bulletin/August*, **18**, 1994
- [Fop 94] Fopale H., Wastner J. B., Tolner A. W., *Can. J. Chem.*, **46**, 1060, 1968
- [Fou 91] Fouge, M., Mandil, C., Amelinckx, S., *Phys. Stat. Sol. A*, **125**, 9, 1991

- [Fie 88] F. Fieser, G. Chetty, G. Cohen, H. Hefek, J. Joffe, A. Kozik, H. Quastman, *Int. Phys. Conf. Ser. No.* 112 67 (1992)
- [Gib 92] Giber A.M., Hershman A.M., Taitel J.B., Aky D.S., Swendsen A., and Nand B., *ALP Conference Proceedings* 261-276 (1992)
- [Gib 94] Gitter O. and Schickler A. *Z. Anorg. Allg. Chem.* 256 291 (1994)
- [Gib 95] Gitter O., Hershman G. *Z. Anorg. Allg. Chem.* 258 219 (1995)
- [Gib 97] Gibb U., Ritz WC, Mates A., and Wenderlich B. *J. Phys. Chem. Ref. Data* 1997 26 769
- [Gib 98] Gibb U. M., Kim S. G., Hershman G. *Inorg. Mater.* 33(1) 112 (1998)
- [Gib 99] Gibb U. M., Kim, S. G. *Inorg. Mater.* 34 2161 (1999)
- [Gol 88] Golobok T., Hershman G., Kuznetsov P. *J. Phase Equilibria*, 19(3) 256 (1988)
- [Gol 89] Goldfinger F., Rosenbaum M., *Advances in Infrared Spectroscopy*, 3 104 (1989)
- [Gol 94] Gray J.L. 17th IRR: Fluorescence Spectral Conference Record 105 (1994)
- [Gro 73] Gromberg Y. M., Baryakova V. A., Shvedikov V. F., *J. Chem. Thermodynamics*, 5 119 (1973)
- [Gro 74] Gromberg Ya. M., Baryakova V. A., Shvedikov V. F. *Int. Abstr. High. Chem.*, *Inorg. Mater.* 7(5) 768 (1974)
- [Gro 75] Gromberg Ya. M., Baryakova V.A., Shvedikov V. F. *Molokhova E. S. Inorg. Mater.* 4 2095 (1975)
- [Gro 76] Gromberg Y.M., Baryakova V. A., Shvedikov V. F. *J. Inorg. Mater.* 11 1542 (1976)
- [Gro 82] Gromberg R. T., Gromberg G. O., De Marsico T. A., Ruzman J. A., *J. Phys. Chem.* 86 976 (1982)
- [Gro 79] Gromberg F. *J. Chem. Thermodynamics* 5 535 (1979)
- [Gro 80] Gromberg F., Gromberg J., Wenzel F.F. "The Chemical Thermodynamics of Actinide Elements and Compounds" part 4 153 International Atomic Energy Agency, Vienna, 1980

- [Cav 74] Gapek E.H., Helweg E., Kolias L. *J. Phys. Chem. (Laurens)* 251 1815 1974
- [Gal 81] Galois T.M., Melvolden, L.B. *Rev. J. Inorg. Chem.* 10(7) 1129 1981
- [Gar 78] Garvick L.V., Yula I.V., V.P. Gushko, gen. ed. "Thermodynamic properties of individual substances" Moska, Moscow, volumes 1-4 1978, 81
- [Hah 11] Hahn H., Buser F. *Angew. Chem.* 123 183, 1981
- [Haw 11] Hawon M., B. Andrich E. *Constitution of Binary Alloys*, McGraw-Hill Book Co. New York, 1981
- [Hir 88] Hirata T., Yamada A., Nakamura Y., Nishino O., and Wada T., Technical Report, 7th International Plasterhouse Science and Engineering Conference (International PHS&E-8 Tokyo, 1988) 198
- [Hys 64] Hysling R.D. *Can. J. Chem.* 42 1253, 1964
- [Hys 66] Hysling R. D. *Can. J. Chem.* 44 1211 1966
- [Hys 74] Hysling R. D. & Murray R.M. *Can. J. Chem.* 52 381 1974
- [Joh 78] Johen, M., Soderqvist, L.J. *Acta Chem. Scand.* 31 1819 1978
- [Jin 81] W. Jinde, G. Kohn, and U.-C. Barckow, *Chem. Rev. Technol.* 21 1187 1981
- [Kee 71] Keenan A., Raymond, J. M., Colwell B., Usher R. *J. Phys. (Frank. Jn)* 717 1971
- [Ker 78] Kerker R., Schwaner R. W., and Hozel F. *Int. Reviews Phys. Chem.* 80 27 1978
- [Ker 81] Kerker R. and Tamura K. *J. Chem. Phys.* 75(2) 788 1981
- [Ker 83] Kerker R., Tamura K., Ito M., Yui M., Hada C., Hoshino H. *J. Chem. Phys.* 79(2) 788 1982
- [Ker 84] Huang J. Y. K., P. W. Gillet, J. E. Bennett. *High Temp. Sci.* 17 109 1974
- [Kil 73] Kilgus R. et al. "Selected values of the thermodynamic properties of the elements" American Society for Metals, Metal Park, OH 1973

- [Bl 17] Blanton T V, Lopez L M *Soft Matter* **558**, 114 (2011) 1073
- [Dm 11] Durr K, Soudo E, Papp T, Hengsten Y, Abo Y *J Cryst Growth* **343** 954 (2011)
- [Jef 14] Jeff J, A. Zenger *Phys Rev* **329** (1982) 1904
- [Me 95] Meeson B, Roden B *High Temp Sci* **35** 203 (1995)
- [Kai 93] Kang P, Peles V, Hays H, Sanyal J, Ruff W, Knappe J, Holc J, Tondin R, Elm G, Knebel A *EPJ CONF PRSC* **44** (1993)
- [Kai 94] Knebel A, Abo J *J Phys C* **28** 1329 (1994)
- [Kai 71] Keller H, Ruckert H, Dany G, Dornat J, Grollinger P, *Z. Physik Chem. (Neue Folge)* **75** 275, (1971)
- [Kai 95] Keller H, Thesis, Universität Darmstadt/Germany, 1975
- [Kai 91] Kelly C J, Ford R C, Knebel A and Ruckert A, *Phil Mag A*, **61** 1269 (1991)
- [Kai 92] K. S. Knight, *Mater Res Bull.*, **27** 161 (1992)
- [Kai 94] Knebel A *Mater Res Bull.*, **3** 329 (1994)
- [Kai 94] Koshakov M A, Koshakov V V, Nikheev N Kh., & Dushan V F *Sov Phys Solid State* **36**(7) 1341, (1994)
- [Kai 94] Koshakov V I, Greshov Ya Kh, Karpachov A, M, Koshchikov B V *Sov Akad Nauk USSR, Young Mater* **30**(10) 1765 (1994)
- [Kai 71] Koshchikov P. & Michay N *Sov Biophys Phys Chem* **7**(2) 76 (1971)
- [Kai 77] Koshchikov G, Ustul H *High Temp High Pressure* **9** 361 (1977)
- [Kai 79] Koshchikov G, Aliev C B. *Micrological Thermochimistry* | 5th ed (Gyrgama, Gelfel) 1979)
- [Kyl 96] Kyler A., Lindgren, Seth L., *J Electrochem Soc* **123**(6) 1084 (1996)
- [Man 67] Manakov K K, Karanov I G, Kanyshkov Y M, Gerasimov D D *Russ P Phys Chem* **41** 640 (1967)
- [Min 11] Minichas C and Spyridakis J *Mater Res Bull* **38** 583, (1991)

- [Sole 62] Maron R., Noell, R., Alamiel, R., and Powell, C., *Solar Cells*, 16-486 (1986).
- [Sole 92] Marudatos H., Takasawa T., *Jpn. J. Appl. Phys.* 34, 6689 (1995).
- [Lar 73] Latimer W. M., *J. Am. Chem. Soc.*, 73, 1486 (1951).
- [Lar 74] Van Landuyt, L., Van Tendeloo, G., and Amelinckx, S., *Phys. Status Solidi A*, 36, R165 (1974).
- [Lar 76] Lieberman A., Carr, D., Hital, R., *Ann. Crystallogr.* B 24, 1 (1978).
- [Lar 74] Lieberman A., Gattard M., *Compt. Rend. C* 279(4) 22 (1974).
- [Lar 88] Lieberman A., Foucaud P., Gattard M., Fichet J., Poulet R., Brylle N., *J. Solid State Chem.* 73, 91 (1988).
- [Lar 75] Lakes, H. L., Hong E. Ts., Ramanamurti, B., *CALPHAD* 1, 275 (1977).
- [Lar 92] Lakes, H. L., *Proc. 3-45, J. Phase Equilibria*, 13(3) 332, 1992.
- [La 92] La Z W., Zenger A., and Deutsch M., *Phys. Rev. B* 47, 8315 (1993).
- [Mar 82] Marudatos C., *J. Solid State Chem.* 33, 91, (1980).
- [Mar 92] Marudatos N., Woloszew, M., in *X-ray powder data file 01-061* and L.G. Berry, *Special Technical Publication 486G* ASTM, Philadelphia, 1989.
- [Mar 94] Maron P.L. and Zenger A., *Phys. Rev. B* 50, 2689 (1994).
- [Mar 97] Maron R.J., Noell, R., Buchanan K.L., Cohen D., *Appl. Phys. Lett.* 70(7) 1036, (1997).
- [Med 67] Medina, R. de, Thesis, Louvain, 65(1967) cited by [Med 97].
- [Med 97] Medina A., Rupp R.C., Goss U. and Waserleick B., *J. Thermal Anal.*, 49, 197 (1998).
- [Mer 96] J.M. Merino, J.L. Martin de Vidales, S. Michaux, R. Durr, F. Rault, *J. Appl. Phys.*, 80(10) 5836 (1996).
- [Mer 98] J.M. Merino, R. Durr, T. Merino, J.L. Martin de Vidales, M. Lema, F. Rault, *Int. Phys. Conf. Ser.* No. 152, 161 (1998).

- [Mc80] McInnes, R.A. *Chem WS Appl Phys Lett* 36 371 (1980)
- [Mc81] McInnes, R.A. *Chem WS*, 17th IEEE Photovoltaic Specialist Conference (instel 800 1981)
- [Mc82] McInnes, R.A. *Chem WS* 10th IEEE Photovoltaic Specialist Conference (instel 784 1982)
- [Mc83] McInnes, R. & C. and Boyce, J.B. *Phys Rev Lett* 49 1411, 1982
- [Mc84] Mills R.C., "Thermodynamic data for inorganic sulphides, selenides and tellurides" London, Butterworths, 1974
- [Mc85] Mills R.C. *High Temp High Pressure* 13 225 1975
- [Mc87] Miller, D. *Vacuo, Z. Sol Stat Ionics*, 21 37 1987
- [Min84] Minshall-Monard, P. *Rev Chem France Meet* 39 1349 1978
- [Min85] Murray, D.D., Hermann, A.M., Tuttle, P.L., Allen, D.S. and Neale, R. *Appl Phys Lett* 38 (23) 2479 1981
- [Min86] Moroski, S.M., Selim, S.R., Selman, S.A., El-Labirani, F.A. *Rev Roumains Phys Chem* 30 123, 1986
- [Mor85] Morley, R. M. & Heyling, R. D., *Can J Chem* 33 875 1975
- [Mus84] Muschall, P. M., Anzures, T. KH., Nair, I. Ya., Johnson, A. & Joseph, Khan, Kh. I. 33 1974
- [Nag81] Nagata K., Ishizuka K. and Miyamoto Y. *Jpn J Appl Phys* 20(1) 611, 1981
- [Nag82] Nagatani K., Lechinsberg, E. *J Phys Chem* 184 48 1980
- [Nes80] Nesb, R., Stulen, Z. *J Fac Sci Hokkaido Univ Ser 3* 1 31 1980a
- [Nes85] Nesbitt, R. and Stulen, Z., *Trans. MSSE Japan* 33 715 1985
- [Ogo80] Ogasawara, Z., Colonna, E. *J Phys Chem Solids* 35 149 1969
- [Ogo82] Ogasawara, Z., Mitsuoka, S., Demizu, G. *J Mater Sci* 17 907 1982
- [Oka80] Oka, T., Ohta, S., *J Phys Soc Jpn* 45(1) 1645 1980
- [Oka88] Okamoto H. *Binary Alloys Phase Diagrams* A824

- [Oli 86] Oliver, M., McMillan, R.R., Wootch, B. J. *Sol. Sol. Trans.* 29:10 (1986)
- [Osh 87] H. Oshino, A. Kuroki, M.H. Bawin, M.J. Comer and R. Hill, *Proc. of the 10th EC Photovoltaic Solar Energy Conference Freiburg*, 155, 1988
- [Pal 87] Palaniak L. S. and Bergerman C.J. *J. Appl. Phys.* 61:11 50 (1987) [*Rev. Phys. Defect* 12 505, 1987]
- [Par 89] Padavanelli R., Ide, M., Soudary B.I., Anderton, T.I. (to be published) 1989
- [Per 73] J. Perkins, R. D. Titchener, and M.J. Hargreaves. *J. Appl. Cryst.* 6 434 (1973)
- [Per 84] E. Perini, *Crystal Chemistry of Extended Structures*, Gordon and Breach, New York, 1984
- [Pet 86] Petrášik A. S., Zeman M.V. *Phys. Mater.*, 20PP 1488 (1986)
- [Pol 90] Polina, A.D., Thompson W.T., Hale C.W., Erickson G. *High Temp. Sci.*, 26 231 (1990)
- [Pop 71] Popescu S., Colantoni B., Bojars D. *Phys. Status Solids A*, 6 301, 1971
- [Pop 78] Popescu S., Tompa A., Plămăreș B. G., Colantoni B., Bojars R., *J. Appl. Crystallogr.*, 12 448, 1979
- [Pre 88] Preiser G., Brockhoff J. *J. Phys. Chem.*, 92 187, 1988
- [Pri 84] Priker V., Samarski J., Reed W., Senter W., Hale J., Haines R., Karg F., Schuch R.W., *Proc. 10th IEEE PV Spec. Conf. Hawaii*, 344, 1984
- [Pri 86] Priker V., Karg F., Samarski J., Reed W., Senter W., Haines R., and G. Mei. *Res. Res. Symp. Proc. Vol. 426*, 185, 1986
- [Rab 86] Rabl P. *J. Phys. Chem.*, 90, 117 (1986)
- [Ram 88] Ramakrishna K., Wimmer H., Acher S., Nilsen Ramanathary R.R., Goss J., Comtes M.A. and Nishi R. *1st World Conference on Photovoltaic Energy Conversion*, Wien, Austria, 1990 (in press)
- [Rao 74] Rao R., *J. Chem. Therm.* 6 325, 1974
- [Rao 83] Rao V. R. *Metall. Trans.*, 14B 108, 1983
- [Rao 85] Radford R.J., Butler H. *J. Electrochem.* 92 497 (1985)

- [Rae 75] Rae H. & Roberts A. *J. Sol. State Chem.* **1** 515, 1976
- [Rat 41] Ratlich G. & Koser A. *Ind. Eng. Chem.* **40** 345 (1944)
- [Rau 87] Rander T., *J. Physique IV* **7** C2-369, 1987
- [Rau 91] Raman A.D. *Yeni Mosk. Univ. Khimya* **49(2)** 119, 1994
- [Rau 93] Raman A.D., Zhigalov V. A. and Lushin N. A. *Mosk. Univ. Khimya*, **49(1)** 5, 1994
- [Rye 75] Ryndersck P.P., Minko P. G., Zaitsev N.M., Fan Hong Yui, Bao Yu. *Kinet. Zh. Prikl. Khim.* **48** 209, 1975
- [Sak 89] Sakuma, T., Sugiyama, K., Mizushima, J., Watanabe, Y. *Nature Trans* **186** 38(3) 345, 1989
- [Saw 71] Sawin H. & Hoch J. *Int. J. Mass. Spectrom. Ion Phys.* **7** 149, 1971
- [Saw 88] Sawin H., Matuszewska A. P. CALPHAD, Colloquium of Phase Equilibria, A. Compere, J. Gasiot, J. Gasiot, Elsevier Science Ltd., Oxford, UK, 1988
- [Sey 87] Seyers G. and Rindler B. in *X-Ray Absorption: Principles, Applications, Techniques of EXAFS, SEXAFS and XANES* edited by D.C. Koningsberger and R. Prins (Wiley, New York, 1987), Chap. 4.
- [Sch 81] Schandzel H., Givian M. J. and Elger R. *Z. Anorg. Allg. Chem.* **494** 76, 1982
- [Sch 83] Schandzel H., Givian M., Grossmold F., Schuch H.W. *J. Appl. Phys.*, **53(5)** 2882, 1983
- [Sch 87] Schuch H.W. and Jack L., in *Proc. 11th NBSL Fluorescence Program Review*, edited by H. S. Ellis and C. E. Wain (AIP, New York, 1987) pp.59
- [Sey 95] Scofield J.H., Ashen R., Allen G., Taitel I., Cauters M., Niles D., Beady R., Bennett A., Nault R. pp.164 *Proc. 1st World Conference on Fluorescence Energy Conversion: Radiation, Hawaii (IEEE, 1994)*
- [Sha 65] Sharlov E. A., Anan T. Kh. *Russ. J. Inorg. Chem.* **10(5)** 645, 1967
- [Shy 75] Shy J.L., Wagner R., Rappert H.M. *Appl. Phys. Lett.* **17(2)** 87, 1975

- [Shu 66] Shu K.C., Guse U., and Wundlich R. *J Polymer Sci Polym Phys Ed.*, 11 449 (1966)
- [Shu 67] J.A. Shuler, C.H. Champness, and J. Wals. *J. Cryst Growth* 32: 187 (1967)
- [Spz 70] R.W. Spruz, U. Ruckert, G. Bausch, A. Rüdter, and J. Schneider. *Phys Status Solidi B* 42: 143 (1970)
- [Stee 70] Steinhilber, G., and Heyding R. D. *Can. J Chem.* 48: 1234 (1970)
- [Ste 64]¹ Stearns G.E., Lacheyne N.P., Medvedev Z.B. *Russ. J Inorg Chem* 9(7): 74 (1963)
- [Ste 64]² Stearns G.E., Lacheyne N.P., Medvedev Z.B. *Russ. J Inorg Chem*, 9(7): 412, (1963)
- [Ste 64]³ Stearns G.E., Elmore A. A., *Russ. J Inorg. Chem.* 9(7): 461 (1963)
- [Ste 64]⁴ Stearns G.E. *Russ. J Inorg. Chem.* 9(8): 1165, (1963)
- [Ste 64] Smart, J.B., Smith, A.A. *Trans AIME* 236: 148 (1964)
- [Ste 65] Stearns, F. *J Metallol.* 75: 71 (1965)
- [Sto 74] Stokhan, G. P., Isakhan Z., Dergach L.V., Kovalev E. V., Sokolova, Z. M. *Int Akad Nauk SSSR Khim. Mater.* 1961: 919 (1974)-in Russian translated as *Inorg Mater.* 10(9): 934 (1974)
- [Sw 67] Swenson R. E., Edwards J. G., *J Electrochem Soc.* 114: 1811 (1967)
- [Sw 68] Swenson R. E. Ph. D. Dissertation, The University of Toledo Toledo OH, (1968)
- [Sw 69] Swadlow B.J., Glas W.S., Michaelson R.A., *Proceedings of the Symposium on Materials and New Processing Techniques for Electrochemical* pp 115 (The Electrochemical Society Inc. NY (1969)
- [Sw 75] Swadlow B.J., Dreyer A., Chang C. H., Anderson T.J. *AEF-Conference Proceedings* 134: 379, (1977)
- [Tay 68] Taylor, A. L. N. *Philips Res Rep Suppl.* 1: 1 (1968)
- [Tay 70] Taylor, A.L.N. *Jellinek P. Ber. Buns. Chem.*, 101: 271, (1970)

- [Ste 75] Steadall R. Z. Naturforsch. 30a, 1481, 1975
- [Ste 77] Steadall R. Z. Naturforsch. 30a, 426, 1975
- [Ste 76] Still D.B. and Smith G.C., "Thermodynamic properties of the elements", American Chemical Society Washington, D.C. 1976
- [Stal 77] Stal D.B. and Wils S.-H., Appl. Phys. Lett. 34, 2021, 1979
- [Ste 81] Steinman, R., Agnew, J. J. Phys. Chem. Solids, 42, 187, 1971
- [Ste 82] Steinman, R., Johnson, B., American J. of CALPHAD 3, 149, 1983
- [Ste 83] Steinman R., Journal of Phase 9, 44, 1978
- [Ste 84] Steinman, R. SCITE Reference Database, SCITE, 1984
- [Tay 76] Taylor P.L., Wagner D.L., Pet, C.H. Met. Trans. 7B, 103, 1976
- [Tak 78] Takashi C., and Bartholdi H.J., J. Phys. Chem., A148, 171, 1978
- [Tsu 84] Tsuge, A., Tsuge, A. M. J. Sol. Stat. Chem., 19, 259, 1981
- [Tsu 84] Tsuge B.H. and West, C. A., J. Appl. Phys. 44(4) 2264, 1984
- [LH 77] Lital H.S., Zureick E., Rabinov B.Y. 36th EPR Phenomena Spectral Conference Record, 320, 1977
- [Yas 68] Yasuoka J. J. J. Phys. Chem., 63, 236, 1968
- [Yas 69] Yasuoka N., Zett. Physik. Chemie Neue Folge 61, 10, 1968
- [Yas 79] Yasuoka N. F., Pashchen A. S., Lashin V.V. In: Akad. Nauk SSSR, Heavy Metals 15, 166, 1979
- [Yas 82] Yasuoka N. F., Gorbun S. I., Pashchen A. S. Inorganic Materials 18(7) 821, 1982
- [Yas 86] Yasu E., & Ogurotsu E. Phil. Mag. 42, 287, 1980
- [Yas 86] Yasu E., Müll, G., Herveau V. Ogurotsu E. Phys. Rev. B, 24(9) 5798, 1981
- [Wu 84] Wu S.-H. and Krikorian H. Phys. Rev. Lett. 53, 1280, 1985
- [Wu 89] Wu S.-H., Zhang G.-B. and Zhang A. Phys. Rev. B 39, R2478, 1989

- [We 93] Wei S-H, Farnen, L. G. and Zenger A. *Phys. Rev. B* 44, 8140 (1993)
- [We 93] Wei S-H, Farnen, L. G. Zenger A. *Phys. Rev. B* 48(2), 2113 (1993)
- [We 94] Wei S-H, Zenger A., Choi, H., Yu P-Y. *Phys. Rev. B* 50, 8170, (1994)
- [Go 94] Kim H-E, Yang, L.-C., and Ruckenstein, A. *J. Appl. Phys.* 76(3) 1366 (1994)
- [Yam 57] Yamaguchi, R., Foster, R. F., *J. Electrochem. Soc.*, 114 (1967), 1987
- [Yam 64] Yamamoto, K., Sakakida, S. *J. Sol. Sol. Chem.*, 10 366, (1964)
- [Yim 93] Young R. A., Sakharov A., Moss T. S. *Paradigms C Co., User's guide to DAWG-9401* (1993)
- [Zab 88] G. Zala, and P. Fowler *Phys. Rev. Tribol.*, 27(4) 499 (1988)
- [Zha 90] S. B. Zhang, Si-Huan Wen, and Alex Zenger. *Phys. Rev. Lett.* 75 4079 (1995)
- [Zha 94] S. B. Zhang, Si-Huan Wen, and Alex Zenger. H. Katsurama-Yoshida, *Phys. Rev. B* 50 5642, (1994)
- [Zhu 99] Zhuang, W. Shen, J. Liu Y. Ling, L. Sheng, S. Du Y., Schuster J.C. *J. Microfluid.* (accepted), 1999

BIOGRAPHICAL SKETCH

Chia-Hung Chang was born in Taipei, Taiwan, on June 18, 1967. He received his B. S. Degree from the Department of Chemical Engineering, National Taiwan University in June 1991. He pursued his undergraduate research in the electrochemistry lab in electrodeposition of platinum thin films on titanium electrodes under Dr. Shi-Cheng Yeh as his senior tutor. From August 1991 to June 1993 he served in the Taiwan Army as a lieutenant. After fulfilling his military service, he worked as a research and development engineer in the Nan-Ya Plastics Company until June 1994. He received a fellowship from the Department of Chemical Engineering, University of Florida, and started his graduate study in August 1994. He joined Dr. Tam Anderson's group in December 1994 and began his graduate research in growing and characterization of Colloidal-based photoelectrodes. He is interested in growth and characterization of semiconductive materials thermodynamics and phase equilibria, and cryobiology. He will join the Chemical Engineering faculty of Oregon State University upon completion of the dissertation.

I certify that I have read this study and that in my opinion it conforms to acceptable standards of scholarly presentation and is fully adequate in scope and quality as a dissertation for the degree of Doctor of Philosophy.


Timothy J. Anderson, Chairman
Professor of Chemical Engineering

I certify that I have read this study and that in my opinion it conforms to acceptable standards of scholarly presentation and is fully adequate in scope and quality as a dissertation for the degree of Doctor of Philosophy.


Oscar D. Casselle
Associate Professor of
Chemical Engineering

I certify that I have read this study and that in my opinion it conforms to acceptable standards of scholarly presentation and is fully adequate in scope and quality as a dissertation for the degree of Doctor of Philosophy.


Paul R. Heflinger
Professor of Materials Science
and Engineering

I certify that I have read this study and that in my opinion it conforms to acceptable standards of scholarly presentation and is fully adequate in scope and quality as a dissertation for the degree of Doctor of Philosophy.


Ming S. Li
Professor of Electrical and
Computer Engineering

I certify that I have read the study and that in my opinion it conforms to acceptable standards of scholarly presentation and is fully adequate, in scope and quality as a dissertation for the degree of Doctor of Philosophy


John H. Johnson
Professor of Chemical Engineering

This dissertation was submitted to the Graduate Faculty of the College of Engineering and to the Graduate School and was accepted in partial fulfillment of the requirements for the degree of Doctor of Philosophy

December 1999


Mr. Jack Johnson
Interim Dean, College of Engineering

Richard M. Phillips
Dean, Graduate School